How Is the Galactic Weather?

Tracing the Baryon Cycle and Gas Flows in the Milky Way's Inner Atmosphere

Bo-Eun Choi

A dissertation
submitted in partial fulfillment of the
requirements for the degree of

Doctor of Philosophy

University of Washington

2026

Reading Committee:

Jessica Werk, Chair

Emily Levesque

Matthew McQuinn

Program Authorized to Offer Degree:

Astronomy

University of Washington

Abstract

How Is the Galactic Weather?

Tracing the Baryon Cycle and Gas Flows in the Milky Way's Inner Atmosphere

Bo-Eun Choi

Chair of the Supervisory Committee:

Professor Jessica Werk
Astronomy

A galaxy's atmosphere is a key factor in its evolution, presenting the cycle of gas flowing between its star-forming disk and the surrounding multiphase gaseous halo. The metallicities, ionization states, and kinematics of these flows determine the gas supply for future star formation and its impact on Galactic chemical evolution. While external surveys reveal the average climate of the circumgalactic medium across many galaxies, only the Milky Way allows individual halo clouds to be resolved spatially, kinematically, and chemically on the scales most directly relevant to the disk.

In this dissertation, I report the current weather of the Milky Way's inner atmosphere and forecast its impact on the Galaxy. Using HST/COS UV absorption spectroscopy combined with Voigt profile fitting and Bayesian photoionization modeling, I measure the metallicity, ionization, and kinematics of halo clouds. First, I introduce a method that uses pulsar dispersion measures from globular clusters paired with UV-bright halo stars to constrain the ionized hydrogen column density, providing a precise ionization correction to the total hydrogen column. The metallicities of the diffuse ionized gas span a wide range and do not separate cleanly into metal-poor inflow and metal-rich outflow, pointing to complex origins. Second, I spatially resolve the metallicity, ionization, and kinematics of a Galactic fountain flow across 27 sight lines through the intermediate-velocity cloud Complex K. The majority of the gas is metal-rich ($\langle Z \rangle \sim 2.4\ Z_{\odot}$), with the most metal-rich components showing the slowest infall and progressively lower metallicities at higher infall velocities. It indicates fountain-driven mixing with the metal-poor corona in action and forecasts that fountain accretion returns gas to the disk well above the metallicities assumed in chemical evolution models. Last, I search the underexplored low-latitude sky and report the discovery of ionized Magellanic Stream gas in a northern extension, whose mass and location refine constraints on the Stream's total gas budget and trajectory toward the disk.

DEDICATION

To my teachers, You Lee (이유) and Taeyang Shin (신태양), who found a faint longing for the cosmos in me and believed, needing no reason, that it would light as long as the Sun.

ACKNOWLEDGEMENTS

Sitting down to write these pages gives me a flashback to the last night of 2020, when I sat down to write the acknowledgements for my master's thesis. That night, I was excited about where my academic journey would take me, but at the same time, I was insecure and intimidated, thinking that if I didn't keep my feet, there was no knowing where I might be swept off to. The past five years of my PhD turned out to be a journey I couldn't have imagined then, and now I mark another milestone on it. I owe all of it to the people I met, and who walked with me throughout it.

First, I would like to thank my advisor, Jess Werk. Her excitement for new ideas and her curiosity about very diffuse but massive and beautiful things have always inspired me and shaped what kind of astronomer I want to be. I have also learned from her diligence, which is what makes things happen, and from the way she mentors her students. Thank you for your steady support and for giving me so many opportunities at every stage, even when my work was not at its best. Thank you also for saving me from going down rabbit holes numerous times, and for helping me in more ways than I can list here. I have been very fortunate to have you as my advisor.

I would also like to thank Emily Levesque for bringing me into the weird stars we work on together, for the conversations I have always enjoyed, for her advice on my career, and for doing so much to make me a better writer. Thanks to Matt McQuinn for serving on my reading committee and for his insight and comments on my work over the years. Thanks to Mario Jurić for serving on my mentoring committee and for his understanding and advice at a time when I felt out of place working in a language that is not my first. I am also grateful to Eric Agol for checking in on me, always with a smile, whether in the hallway or in the U District, and for the understanding and generosity that meant a lot to me when I was struggling.

This thesis work could not have been done without my collaborators, and I have been lucky to work with them. I would especially like to thank Kirill Tchernyshyov for his mentorship, for working through every problem in my research with me, and for staying with this work. Thanks also to Andy Fox for being so welcoming, for our discussions about halo gas, and for his help and advice with observing proposals and with my career. Thanks to DIGG for fun discussions about gas, and especially to Yakov Faerman for being a mentor to me, not so much on my research, but as someone always open, always excited to talk, and always warm.

One of the things I appreciate most from my PhD journey is the grad community, and the friends I made in it. I had no one in the US when I first came to Seattle. Now I have friends I could not do without, and the grad community is the core of that. To the Fab Five: I was lucky to have this cohort, and congratulations again to all of us, all doctors at last. I could fill another thesis with everyone I owe for joy and support, so here are a few. Debby, for our conversations that comforted and supported me, for their wisdom which showed me things I had not thought about, and for their generosity that took me in when I had nowhere to stay for weeks. Sam, for being my roommate, my officemate, and my research groupmate, for still being on my emergency contact, and for all the beautiful cards. Andy, for always being there, and for getting through job applications alongside me. Gabby, for being as enthusiastic about Disney movies as I am (more than I am, honestly), and for saving me when I was stressed out about my first department talk and having nightmares about it. David, for planning every good event, and for bringing home a little closer with soju mixed with hongcho, Lunar New Year, and trips to H Mart. Fran, for always checking in, and for coworking that actually made me productive enough to finish this thesis. V, for being there all the time, for cheering me up, and for the smile that comes with "Bonni!!!!" Lupita, for the welcoming card when I was accepted to UW Astro, and for being so warm ever since.

Some of the people who walked this road with me were with me long before my PhD started. Seok-Jun Chang, for being the person I looked to when I needed to know whether I was on the right track, for always being willing to help, for our conversations about research and about careers, and for building the foundation of my programming skills from the day I printed "Hello, world!" in Fortran in my freshman year. Jeong-Eun Heo, for teaching me everything I know about spectroscopic observation, and for being an incredible mentor to me in many ways. Hee-Won Lee, for showing me the beauty of spectroscopy, and of physics more generally, that I fell in love with and have never gotten over. Gunn Kim, for advice that has helped me become a scientist. Miji Jeong, for always being generous and for bringing so much energy. Last but not least, Hye-Jin Park, for listening to all my whining throughout my PhD, for our silly discussions over Zoom across time zones, and for cheering me up every time I was struggling. I know I still owe you a Kookaburra song.

I would also like to send my gratitude to my friends and family at home, across the Pacific, or wherever they are now, who have always been up for a call and have never stopped sending me their support. Kanghee, for being my friend for the past 25 years, more like family, and for clearing her schedule whenever I was home and taking me everywhere fun. Minjeong and Seona, for making me read books other than astronomy papers, and for their warmth. Young-Min, for chatting about physics and IU, and for getting me into wine. Jihyeon, for all the conversations we had while walking around San Francisco. Jieun, for being there, like home, on our bridge. Lastly, my family, and especially my mom. Thank you for giving me this life, and for all the sacrifice and dedication that gave me better opportunities than you had. I am almost the age you were when you had me, and I still cannot understand how much you love me.

Thank you to all for lighting up my *microcosmos*. I can't wait for the next chapter, and I can't wait to see what I'll find as I continue exploring the Universe.

CONTENTS

LIST OF FIGURES

LIST OF TABLES

Chapter 1

Introduction

1 Galaxy's Atmosphere and Baryon Cycle

A galaxy forms an ecosystem in which the flow of energy and matter between its components shapes its evolution. Much like Earth's ecosystem comprises biotic and abiotic elements whose interactions drive the system's trajectory, a galaxy's “biotic" component, its stars, forms from, interacts with, and returns material to its surrounding abiotic medium. We define a galaxy as a dark matter halo harboring a long-lived stellar system (Bromm & Yoshida 2011), which can be reinterpreted as a system that has managed to host, sustain, and regulate star formation despite the disruptive effects of its own feedback. Understanding galaxy evolution, therefore, means understanding how gas is supplied, converted into stars, and redistributed, that is, how matter and energy circulate within this ecosystem.

In the standard ΛCDM cosmology, baryons are pulled into halos, following gravitationally dominant dark matter, where gas can radiatively cool and condense toward the halo center to eventually form stars (White & Rees 1978). If this process were efficient, galaxies should retain a baryon fraction close to the cosmic mean. Yet observations consistently show that galaxies contain far fewer baryons in their stars and ISM than their halos can account for, the so-called “missing baryon problem" (e.g., Behroozi et al. 2010; McGaugh et al. 2010). A significant fraction of baryons must therefore reside within the halo in a form that has been difficult to detect, or have been expelled beyond the halo entirely. Furthermore, even the detected baryons present a puzzle. The gas depletion timescale, $\tau_{\rm dep} \sim M_{\rm gas}/\dot{M}_*$, for typical star-forming galaxies is ∼1–2 Gyr (Bigiel et al. 2008; Leroy et al. 2008), far shorter than their ∼10 Gyr ages. In other words, galaxies do not have enough gas in their ISM to sustain star formation at their current rates, implying that they must continuously accrete fresh gas from outside the disk.

Both these questions, where the missing baryons reside and how galaxies sustain their star formation, point to a component of the galactic ecosystem that has long been underexplored: its gaseous atmosphere, the circumgalactic medium (CGM). The CGM extends from the boundary of the ISM to the virial radius (∼200–300 kpc for a Milky Way-mass galaxy) at characteristic densities of $\sim 10^{-4} - 10^{-2}$ cm^{-3} (Tumlinson et al. 2017). Despite this diffuseness, absorption-line observations against bright background sources have revealed cool, ionized gas ($T \sim 10^4$ K) is prevalent in low-redshift, L^* galaxies out to ∼150 kpc, with a characteristic total mass of $M_{\rm cool,CGM} \sim 10^{10-11}\, M_\odot$ (e.g., Prochaska et al. 2017a; Werk et al. 2014). The CGM also harbors metals ejected through stellar and/or AGN-driven outflows (e.g., Peeples et al. 2014), while simultaneously serving as the reservoir from which gas accretes to fuel star formation in the ISM. In the ecosystem picture, the CGM is the atmosphere mediating the exchange of matter and energy between the galaxy and the IGM, and the baryon cycle that drives galaxy evolution plays out within it.

2 Multiphase Circumgalactic Medium

The idea of a hot gaseous corona surrounding a galaxy was first proposed by Spitzer (1956). Motivated by observations of Na I and Ca II absorption toward high-latitude stars (Münch & Zirin 1961) [1], he noted that interstellar clouds observed far from the Galactic plane could not be self-gravitating and would disperse without an external confining medium. He argued that pressure equilibrium between these clouds and a surrounding rarefied, hot gas required a Galactic corona at $\sim 10^6$ K, with an electron density of $\sim 5 \times 10^{-4}$ cm^{-3}. This early prediction anticipated what would later be understood in the cosmological context. In ΛCDM, the thermal state of gas within a dark matter halo is set by the halo's gravitational potential. From the virial theorem, the characteristic temperature of virialized gas is

$$T_{\rm vir} = \frac{GM\mu m_{\rm H}}{2r_{\rm vir}k_{\rm B}} = \frac{\mu m_{\rm H} V_c^2}{2k_{\rm B}} \tag{1.1}$$

where μ is the mean molecular weight and V_c is the circular velocity at the virial radius $r_{\rm vir}$ for a halo mass of M. This can be scaled following Bromm & Yoshida (2011) with the

[1] Münch's observations were published later in 1961, but the two appeared to have been in discussion about these results prior to Spitzer's 1956 publication.

density contrast Δ_c as a function of redshift (Bryan & Norman 1998):

$$T_{\rm vir} \simeq 10^4 \left(\frac{\mu}{0.6}\right) \left(\frac{M}{10^8 M_\odot}\right)^{2/3} \left[\frac{\Delta_c}{18\pi^2}\right]^{1/3} \left(\frac{1+z}{10}\right) \text{ K.} \tag{1.2}$$

For a Milky Way-mass halo ($M_{\rm h} \sim 10^{12}\ M_\odot$) at z=0, this yields $T_{\rm vir} \sim 10^6$ K, consistent with Spitzer's prediction. As dark matter halos grow through hierarchical merging, infalling baryons are shock-heated near the virial radius, forming a hot, quasi-hydrostatic atmosphere filling the halo (Birnboim & Dekel 2003; White & Frenk 1991). Whether gas can accrete onto the central galaxy without being shock-heated to the virial temperature depends on the halo mass and redshift, giving rise to the distinction between cold-mode and hot-mode accretion, which we discuss further in Section 3.1.

Despite this expectation of a hot halo, the multiphase nature of the galactic atmosphere was in fact implicit from the beginning: Spitzer's own argument required cool clouds to coexist with the hot corona that confines them. Over the following decades, absorption spectroscopy against background quasars revealed cool and warm halo gas around external galaxies (e.g., Bergeron 1986; Chen et al. 2001). The Cosmic Origins Spectrograph (COS) on the *Hubble Space Telescope* (HST), with its order-of-magnitude improvement in UV sensitivity, enabled systematic surveys that confirmed multiphase gas is ubiquitous in the halos of low-redshift galaxies with cool and warm gas coexisting across temperatures spanning $T \sim 10^4$–$10^{5.5}$ K (Bordoloi et al. 2018; Tumlinson et al. 2011; Werk et al. 2013). Understanding how this multiphase structure arises, what sustains it, and how it participates in gas accretion and the broader baryon cycle has become a central question in galaxy evolution. In this section, we discuss the observational techniques used to characterize this gas (Section 2.1) and the physical processes that govern its origin and survival (Section 2.2).

2.1 Absorption Spectroscopy

The primary tool for characterizing the diffuse CGM is absorption spectroscopy against bright background sources. When light from a distant quasar passes through intervening gas, atoms and ions along the line of sight absorb photons at their characteristic transition wavelengths, imprinting features on the observed spectrum. Because CGM gas has typical hydrogen number densities of $n_{\rm H} \sim 10^{-5}$–10^{-3} cm^{-3} (Fig. 1.1), orders of magnitude lower than the ISM ($n_{\rm H} \gtrsim 10^{-1}$ cm^{-3}). Since emission scales as n^2, the emissivity of CGM gas is at least 4–8 orders of magnitude lower than that of the ISM, making direct detection in emission extremely challenging. Absorption spectroscopy, by contrast, is uniquely powerful for studying this diffuse medium. It is sensitive to column densities as low as $N \sim 10^{12}$ cm^{-2}, and because it measures the fraction of light removed from a background source rather than light emitted by the gas itself, the detection sensitivity is independent of the redshift and luminosity of the host galaxy (Tumlinson et al. 2017). Absorption measurements provide two key quantities along each sight line: the column density of the absorbing ion and the kinematic structure of the gas.

Column densities can be extracted from absorption spectra using several approaches. The apparent optical depth method (AODM; Savage & Sembach 1991) is a non-parametric technique that converts the observed flux decrement at each velocity pixel directly into an apparent column density per unit velocity, without requiring assumptions about the number of components or their line shapes. However, it can underestimate column densities when lines are saturated, as unresolved saturation within the instrument's resolution element causes the apparent optical depth to fall below the true value.

For a more complete characterization, Voigt profile fitting decomposes the observed absorption into individual components, each described by three free parameters: the column density N, Doppler b-parameter, and the line centroid velocity v. This approach is most effective with high spectral resolution data that can resolve individual kinematic

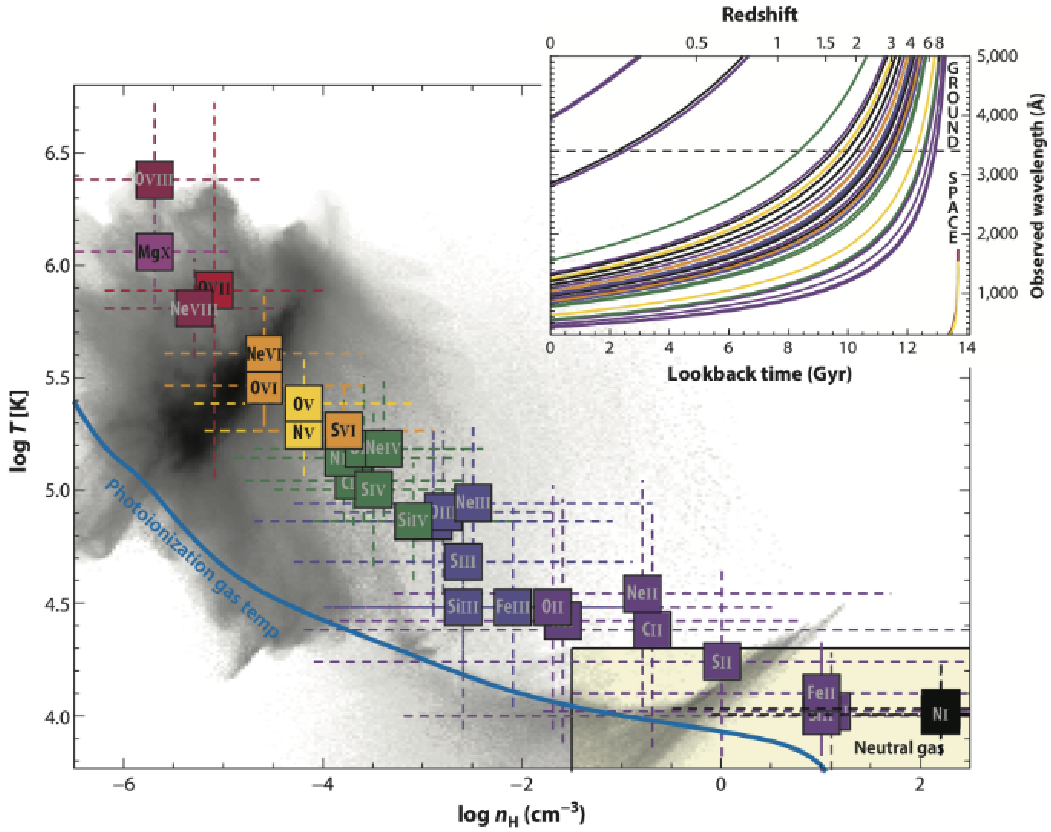

Figure 1.1: Metal absorption lines tracing the multiphase CGM, distributed in the temperature–density (T–$n_{\rm H}$) plane. Each ion is positioned at the temperature where its ionization fraction peaks in collisional ionization equilibrium (CIE) and the density where it peaks in photoionization equilibrium (PIE). Points are colored by ionization state, from neutral (black) to highly ionized (magenta).Rest-frame wavelengths of the same transitions. At $z \lesssim 0.2$, most diagnostic transitions of the cool and warm CGM fall in the UV, motivating *HST*/COS as the primary instrument for low-redshift CGM studies. Reproduced from Tumlinson et al. (2017); CIE and PIE ionization fractions adopted from Gnat & Sternberg (2007) and Oppenheimer & Schaye (2013), respectively.

components, and when multiple transitions of the same ion are fitted simultaneously to break degeneracies between N and b. The Doppler b-parameter encodes both thermal broadening ($b_{\rm th} = \sqrt{2k_{\rm B}T/m}$, where m is atomic mass) and non-thermal contributions such as turbulence ($b_{\rm nt}$), combined as $b = \sqrt{b_{\rm th}^2 + b_{\rm nt}^2}$. For well-resolved components, comparing b values across ions of different atomic mass can disentangle thermal from non-thermal broadening and constrain the gas temperature. The centroid velocity traces the bulk motion of the gas along the line of sight, encoding kinematic information on inflows, outflows, and rotation within the halo. Voigt profile fitting is the primary method employed throughout this dissertation for extracting the physical properties of CGM absorbers.

Metal absorption lines serve as tracers of the multiphase CGM, with different ion species probing gas at different temperatures and densities (Fig. 1.1; reproduced from Tumlinson et al. 2017). Most of the key diagnostic transitions fall in the UV, which is why COS has been the primary instrument for low-redshift ($z \lesssim 1$) CGM studies with large, systematic surveys (e.g., COS-Halos, Tumlinson et al. 2013; Werk et al. 2013; COS-CGM, Lehner et al. 2018) that established the modern observational picture of the CGM. These surveys revealed several key results: H I gas is nearly ubiquitous around star-forming galaxies and extends out to ∼300 kpc (Bordoloi et al. 2018; Wilde et al. 2023); the cool CGM contains a substantial baryonic mass of $M_{\rm cool} \sim 10^{10-11}\ M_\odot$, potentially comparable to the stellar mass of the host galaxy (Werk et al. 2014); the CGM is enriched with metallicities spanning [Z/H] ∼ -1.5 to +0.5 (Prochaska et al. 2017a); and the CGM properties correlate with host galaxy properties, with star-forming galaxies exhibiting higher C IV and O VI column densities absorption than passive galaxies of similar mass (Garza et al. 2025; Tumlinson et al. 2011).

Translating observed column densities into physical properties such as gas density, temperature, and metallicity requires an ionization model. In photoionization equilibrium (PIE), ion fractions are primarily set by the gas density and the intensity of the UV background (e.g., Haardt & Madau 2012), and can be computed using codes such as Cloudy (Ferland et al. 2017). In collisional ionization equilibrium (CIE), ion fractions depend only on temperature, and CIE applies to the hotter CGM phases at $T \gtrsim 10^5$ K. Column density ratios of ions from the same element are particularly powerful diagnostics, as they remove the dependence on chemical abundance and directly constrain the ionization state. However, both mechanisms can operate simultaneously, and for ions such as O VI, which can be produced by either photoionization in low-density gas or collisional ionization at $T \sim 10^{5.5}$ K, the dominant mechanism remains debated (Stern et al. 2018). Gas that is rapidly cooling or recently shocked may not be in equilibrium at (Gnat & Sternberg 2007; Oppenheimer & Schaye 2013), adding further uncertainty to derived physical properties.

2.2 *Cooling and the Origin of Multiphase Gas*

The existence of cool gas within a hot halo raises a fundamental question: what creates and sustains this multiphase structure? The answer is closely tied to radiative cooling. The cooling rate per unit volume scales as $n^2\Lambda(T, Z)$, where the cooling function Λ depends on temperature and metallicity. Metal-line cooling is highly efficient at $T \sim 10^{4.5}$–10^6 K, and when the cooling time becomes short compared to the dynamical time, the hot halo becomes susceptible to thermal instability (Field 1965). This process naturally produces cool, dense clouds embedded in the hot, diffuse halo. A key assumption in many CGM models is that these phases coexist in approximate thermal pressure equilibrium (Maller & Bullock 2004; Mo & Miralda-Escude 1996; Spitzer 1956), though recent observations suggest the picture may be more complex, with non-thermal pressure sources such as turbulence, magnetic fields, or cosmic rays potentially playing a role (Salem et al. 2016; Werk et al. 2014).

The survival and fate of cool clouds within the hot halo is also a critical problem. A cool cloud moving through a hot ambient medium is subject to destruction by hydrodynamic instabilities (Kelvin-Helmholtz, Rayleigh-Taylor) on the cloud-crushing timescale (Klein et al. 1994). However, recent simulations have shown that radiative cooling at the turbulent interface between the cloud and the hot medium can fundamentally alter this picture. If the cooling time of the mixed, intermediate-temperature gas is shorter than the cloud destruction time, the cloud can survive and even grow by accreting material from the hot phase (Gronke & Oh 2018 2020). The turbulent mixing layers at cloud boundaries mediate mass, momentum, and energy exchange between the phases (Fielding et al. 2020), and the efficiency of this process determines whether cool clouds are destroyed, maintained, or grow over time. McCourt et al. (2018) further argued that cooling gas may fragment into small cloudlets with characteristic sizes set by the cooling length $l_{\rm cool} \sim c_{\rm s} t_{\rm cool}$, potentially far below current numerical resolution.

3 Gas Flows within the Circumgalactic Medium

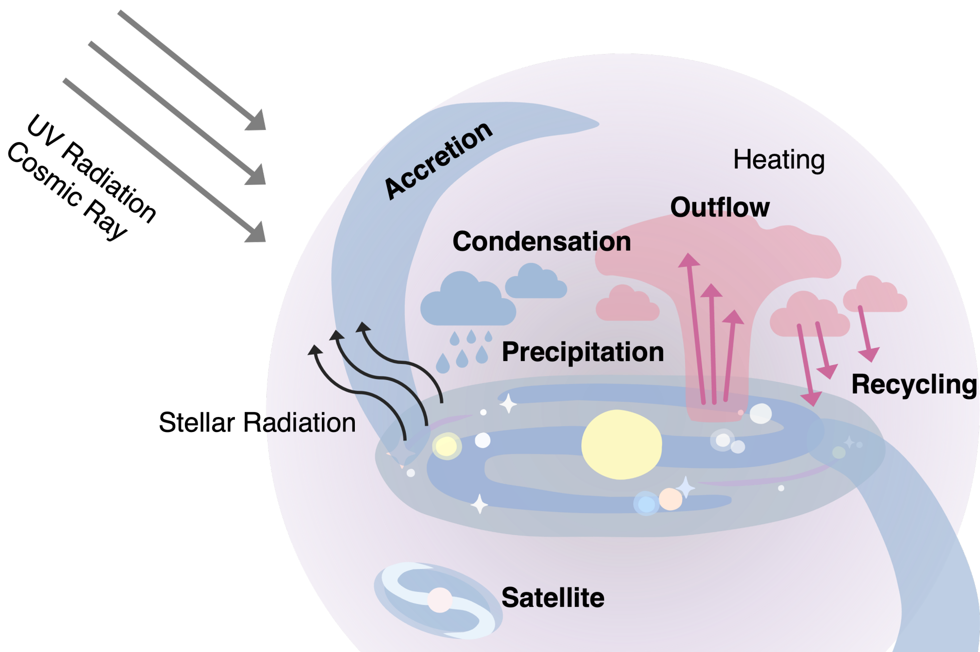

Figure 1.2: Schematic illustration of gas flows and physical processes within the gaseous atmosphere of a galaxy. The central disk hosts stars and the ISM, embedded within a multiphase CGM that extends to the virial radius. Gas accretes from the cosmic web (*Accretion*, blue stream), while feedback from star formation and AGN drives metal-rich material out of the disk (*Outflow*, pink plumes), heating the surrounding halo. Within the halo, radiative cooling and thermal instability lead to *Condensation* of cool clouds out of the hot phase, which subsequently rain down onto the disk as *Precipitation*. Some outflowing material lacks the velocity to escape and falls back as *Recycling* (galactic fountain). Satellite galaxies contribute additional gas through ram-pressure and tidal stripping (*Satellite*), and the diffuse halo gas is ionized by *Radiation* from both young stars in the disk and the extragalactic UV background. These processes, analogous to atmospheric circulation, precipitation, and weather on Earth, collectively constitute the baryon cycle that regulates galaxy evolution.

As introduced in Section 1, the gaseous atmosphere of a galaxy is not a static reservoir of baryons but a dynamic system in which the flow of matter between different components drives the galaxy's evolution. Figure 1.2 illustrates this picture schematically. Gas accretes from the IGM into the halo, where it may be shock-heated or flow directly toward the disk. Within the hot halo, radiative cooling and thermal instability drive condensation and precipitation of cool clouds onto the galaxy, as discussed in Section 2.2. Star formation and active galactic nucleus (AGN) activity in the disk launch outflows that carry gas and metals back into the halo, depositing energy that heats the halo, while the gas itself may recycle back to the disk or escape entirely. Satellite galaxies contribute additional gas through tidal and ram-pressure stripping. These processes, which mirror familiar atmospheric phenomena of weather, precipitation, and circulation, collectively constitute the baryon cycle and determine how a galaxy grows, forms stars, and evolves over cosmic time (Faucher-Giguère & Oh 2023; Tumlinson et al. 2017).

3.1 *Gas Accretion from the IGM*

Sustaining star formation over cosmic time requires a continuous supply of fresh gas. As mentioned in Section 1, the short gas depletion timescale relative to galaxy ages implies that galaxies must accrete gas from their surroundings (Bigiel et al. 2008; Leroy et al. 2008). How this gas is delivered depends critically on the dark matter halo mass. Two distinct modes of gas accretion have been identified in theoretical work and cosmological simulations. In low-mass halos ($M_\mathrm{h} \lesssim 10^{11.5}\ M_\odot$), the cooling time of infalling gas is shorter than the free-fall time, preventing the formation of a stable virial shock. Gas accretes along cold filamentary streams from the cosmic web directly onto the galaxy without being heated to the virial temperature (Dekel & Birnboim 2006; Dekel et al. 2009; Kereš et al. 2005). This "cold-mode" accretion is predicted to dominate at high redshift ($z \gtrsim 2$), when most halos are below the critical mass threshold, and may fuel the peak of cosmic star formation (Kereš et al. 2009; van de Voort et al. 2011). In more massive halos ($M_\mathrm{h} \gtrsim 10^{12}\ M_\odot$), a stable virial shock develops near the virial radius, heating infalling gas to $T \sim T_\mathrm{vir}$. In this “hot-mode" accretion regime, gas must first cool radiatively from the hot halo before it can accrete onto the galaxy, a process that is slower and can be further suppressed by feedback (Birnboim & Dekel 2003; Dekel & Birnboim 2006; Stern et al. 2020). For Milky Way-mass halos at $z \sim 0$, the hot mode is expected to be the dominant accretion channel, with gas cooling from the hot corona supplying fuel to the disk (Fraternali 2017; Hafen et al. 2022; Stern et al. 2020).

Observational evidence for gas accretion onto galaxies remains largely indirect. The existence of low-metallicity absorbers in the cool CGM is consistent with the accretion of relatively pristine IGM gas (Fumagalli et al. 2016; Lehner et al. 2013; Wotta et al. 2019), and kinematic signatures of infalling gas have been identified in some down-the-barrel absorption studies (Martin et al. 2012; Rubin et al. 2012). For the Andromeda galaxy, semi-analytic modeling of the AMIGA project's cool CGM observations (Lehner et al. 2020) favors a low-metallicity infall scenario over an outflow-driven picture (Afruni et al. 2022), providing the cleanest case for IGM-origin accretion in a Local Group L^* galaxy. However, unambiguously identifying accreting gas remains challenging because absorption spectra provide only line-of-sight velocities, and accretion signatures can be mimicked by other gas flows seen in projection. In the Milky Way, certain high-velocity clouds with low metallicities have been interpreted as accreting material (Fox et al. 2019; Wakker et al. 1999), though their origin remains debated (see Section 4.1).

3.2 Galactic Outflows and Fountain

Feedback from star formation and AGN drives gas out of galaxies and into the CGM. Supernovae (SNe), stellar winds, and radiation pressure from massive stars inject energy and momentum into the ISM, launching outflows that can carry gas, metals, and dust into the halo (Veilleux et al. 2005 2020). Observations of blueshifted absorption lines in the spectra of star-forming galaxies provide direct evidence of such outflows at low redshift (Chisholm et al. 2017; Martin et al. 2012; Rubin et al. 2012), and at $z \gtrsim 2$ (Steidel et al. 2010). The connection between outflows and CGM enrichment has been established more directly by the COS-Burst program (Heckman et al. 2017), which finds that the cool CGM around starburst galaxies contains stronger and more kinematically extended metal-line absorption than that around control samples of normal star-forming galaxies, demonstrating that starburst-driven winds actively shape the metal content and kinematics of the surrounding halo gas. The mass-loading factor, $\eta = \dot{M_{\rm out}}/\dot{M}_*$, which quantifies the ratio of the outflow rate to the star formation rate, is a critical but poorly constrained parameter that varies with galaxy mass, star formation rate, and redshift (Heckman & Thompson 2017; Muratov et al. 2015).

Not all outflowing gas escapes the halo. For Milky Way-mass galaxies, much of the ejected material lacks sufficient velocity to overcome the gravitational potential and instead returns to the disk on timescales of $\sim$0.1–1 Gyr, constituting a “galactic fountain" (Bregman 1980; Fraternali 2017; Shapiro & Field 1976). In fountain models, gas is launched from the disk by supernova feedback, rises to heights of a few kpc above the plane, and falls back after cooling and decelerating in the halo (Fraternali & Binney 2006; Marasco et al. 2012). This recycling process is expected to produce CGM gas with near-solar metallicity, reflecting its disk origin, and with kinematics that partially co-rotate with the galaxy (Fraternali & Binney 2008; Marinacci et al. 2011).

A key aspect of the galactic fountain is its interaction with the ambient hot halo gas. As fountain clouds travel through the corona, they can accrete material from the hot medium through radiative cooling at the cloud-halo interface (Fraternali 2017; Gronke & Oh 2020; Marinacci et al. 2010). This process, sometimes called “fountain-driven accretion", provides a mechanism by which hot halo gas, which might otherwise have prohibitively long cooling times, can be efficiently delivered to the disk via mixing with recycled fountain material (Armillotta et al. 2016; Fraternali & Binney 2008). The metallicity of the resulting gas mixture is intermediate between the disk metallicity and the coronal metallicity, providing an observational prediction that can be tested through detailed abundance measurements of halo clouds. Cosmological simulations with the FIRE project have shown that recycled gas (previously ejected from the galaxy) constitutes a significant fraction of CGM mass and subsequent accretion at low redshift, often comparable to or exceeding the contribution from fresh IGM accretion (Anglés-Alcázar et al. 2017; Hafen et al. 2019 2020).

3.3 *Satellite Contributions*

Satellite galaxies provide a third gas-flow channel into the CGM of their host. As satellites orbit through the host's hot halo, ram-pressure stripping removes their interstellar gas, while tidal forces strip material from their outskirts. Both processes deposit gas, often at metallicities reflecting the satellite's prior chemical evolution rather than the host's. In FIRE simulations, gas ejected or stripped from satellites can contribute a CGM mass comparable to that from central-galaxy winds in L^* halos (Hafen et al. 2019). Satellite stripping is especially efficient for dwarf galaxies, whose shallow potential wells allow even modest ram pressure to remove gas; recent simulations show that the CGM of dwarfs is itself easily stripped during interactions with massive hosts (Zhu et al. 2024). Direct observational evidence for this process includes the truncated CGM of the Large Magellanic Cloud (Mishra et al. 2024), where the cool gas envelope is confined to small distances by interaction with the Milky Way halo. The Milky Way's own most prominent satellite-stripped feature, the Magellanic Stream, is discussed in detail in Section 4.1.

3.4 *Metallicity as a Tracer of Gas Flows*

Metals are synthesized by stars in galactic disks and are therefore natural tracers of gas that has been processed through star formation. As metals are produced, they are distributed across the components of the galaxy ecosystem: outflows carry metals into the CGM and beyond, while accretion brings in relatively metal-poor gas from the IGM. At the scale of individual galaxies, only ∼20–25% of the metals produced by stars are retained in the ISM and stars (Peeples et al. 2014); the rest has been transported into the CGM and IGM through feedback-driven outflows (e.g., Tremonti et al. 2004). On cosmic scales, comprehensive metal censuses accounting for all phases (stars, cold neutral gas, warm-hot CGM, and hot intracluster gas) can largely account for the total metal production, leaving little evidence for a global “missing metals problem" (Péroux & Howk 2020). Metals are not lost but redistributed across different gas phases and spatial scales by the baryon cycle.

This redistribution motivates the use of metallicity as a diagnostic of gas-flow origin. In its simplest form, the picture is: metal-poor gas ($Z \lesssim 0.1\ Z_\odot$) traces relatively pristine IGM accretion (Section 3.1), while metal-enriched gas ($Z \gtrsim 0.5\ Z_\odot$) traces material ejected from the disk via outflows or recycled through fountain flows (Section 3.2). This dichotomy is supported observationally by the bimodal metallicity distribution of partial Lyman limit systems at $z \lesssim 1$, by the higher C IV and O VI columns around star-forming versus passive galaxies (Garza et al. 2025; Tumlinson et al. 2011), and by the broad CGM metallicity range spanning $[Z/\mathrm{H}] \sim -1.5$ to $+0.5$ (Prochaska et al. 2017a), which encompasses both pristine IGM gas and disk-enriched material. It is also a necessary feature of equilibrium chemical evolution models: the observed mass-metallicity relation (Maiolino & Mannucci 2019; Tremonti et al. 2004) and the fundamental metallicity relation that includes star formation rate (Mannucci et al. 2010) can be reproduced only if inflow and outflow metallicities are systematically offset, with relatively metal-poor inflows diluting the ISM and metal-rich outflows removing enriched gas (Andrews et al. 2017; Davé et al. 2012; Lilly et al. 2013).

The picture is more complicated in detail. Subsequent absorption-line surveys with larger samples have found that the bimodality reported by Lehner et al. (2013) weakens or disappears with improved statistics (Prochaska et al. 2017a; Wotta et al. 2019), and that CGM metallicity is independent of azimuthal angle relative to the host galaxy (Pointon et al. 2019), contrary to expectations if metal-rich outflows were spatially distinct from metal-poor accretion. Cosmological simulations offer a physical explanation: gas can persist in the CGM for billions of years, allowing recycled outflow material and freshly accreted IGM gas to mix on timescales shorter than the chemical equilibration time (Hafen et al. 2019). As a result, the metallicity of CGM gas is a poor predictor of its origin or its ultimate fate (Hafen et al. 2020). The simple metal-poor-inflow / metal-rich-outflow dichotomy persists in the statistical distributions and in chemical evolution arguments, but at the level of individual gas parcels, metallicity reflects mixing history more than provenance.

These complications matter most at the disk-halo interface, where mixing is most efficient and where the consequences for galaxy evolution are most direct. Gas flows at $d \lesssim 10$ kpc above the disk are the immediate fuel reservoir for the next generation of star formation, and their chemical composition sets the initial conditions for the ISM that follows. Whether the metal-poor/metal-rich distinction survives at this scale, or whether mixing has already homogenized the inflowing material to intermediate metallicities, is poorly constrained observationally. The Milky Way is the only galaxy where individual halo clouds at the disk-halo interface can be resolved spatially, kinematically, and chemically, making it the natural laboratory for testing how the metallicity-flow framework applies on the scales where it matters most for star formation. We turn to this in Section 4.

4 The Milky Way

The Milky Way is where all of the CGM physics described in the previous sections plays out as our own Galaxy's "weather." External CGM surveys give us climate. With samples of hundreds to thousands of background quasar sight lines through galaxies of varying mass, redshift, and orientation (e.g., Lehner et al. 2018; Tumlinson et al. 2013), they yield statistical pictures of how the CGM behaves on average: covering fractions, scaling relations, mass budgets. These pictures are powerful, but they are also necessarily averaged. A single sight line through an external galaxy probes one chord of one realization of the CGM, and the underlying physical conditions, kinematics, and origin of any individual absorber must be inferred indirectly through models. The Milky Way, by contrast, gives us weather. We can map individual halo clouds across the sky in H I emission, bracket their distances using foreground/background halo star pairs, measure their kinematics relative to a known Galactic frame, and probe their physical structure through absorption against multiple background sources. The trade-off is sample size of one, but the resolution and detail are unmatched, and the physical processes operating in the inner Galactic atmosphere can be tested at a level inaccessible in any other galaxy. The Milky Way is therefore a unique laboratory for testing the picture of the baryon cycle on the spatial scales that matter most: the immediate gas supply for the next generation of star formation. This section introduces the observed halo gas population (Section 4.1), the chemical evolution context that this gas supply must satisfy (Section 4.2), and the open questions that motivate this dissertation (Section 4.3).

4.1 High- and Intermediate-Velocity Clouds

The most directly observable halo gas structures in the Milky Way are high-velocity clouds (HVCs) and intermediate-velocity clouds (IVCs), cold and cool gas clouds so named for their line-of-sight velocities that are inconsistent with Galactic disk rotation. HVCs are conventionally defined as clouds with $|v_{\rm LSR}| > 90$ km s^{-1} and IVCs as clouds with $40 \lesssim |v_{\rm LSR}| \lesssim 90$ km s^{-1} (Wakker & van Woerden 1997). In the neutral phase, both populations have been extensively cataloged through all-sky H I 21 cm surveys (HI4PI Collaboration et al. 2016; Kalberla et al. 2005; Peek et al. 2011; Westmeier 2018; Winkel et al. 2016), revealing them to be distributed across the sky and organized into large coherent complexes with a total H I mass of $2.6 \times 10^7\ M_\odot$, excluding the Magellanic Stream (Putman et al. 2012).

HVCs and IVCs are inner-halo structures. Absorption surveys toward halo stars at known distances constrain IVC scale heights to ~ 1 kpc and HVC scale heights to ~ 3 kpc (Lehner et al. 2022; Wakker 2001). The Magellanic Stream is the principal exception. As a trail of gas stripped from the Magellanic Clouds, it extends more than 150° across the southern

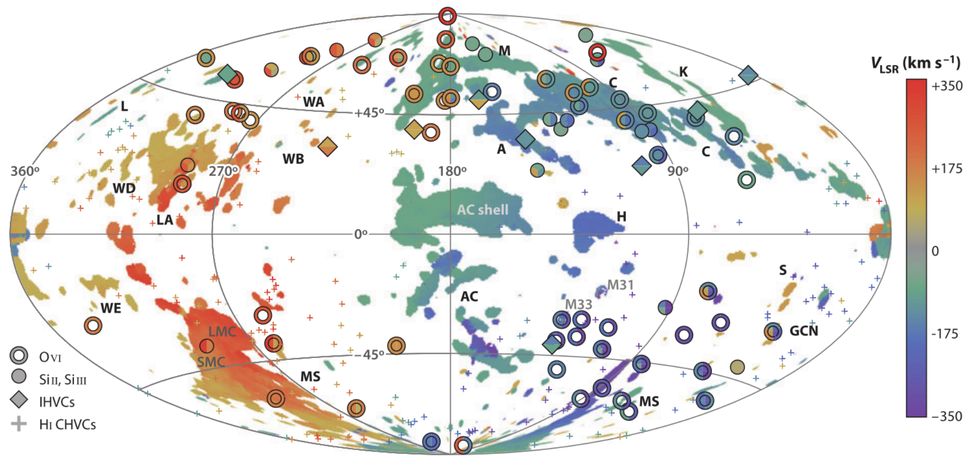

Figure 1.3: All-sky distribution of high-velocity gas in the Milky Way halo, with colors denoting local-standard-of-rest (LSR) velocities. Shaded regions show H I HVCs from 21 cm emission, with plus symbols marking compact HVCs. Open circles, filled circles, and diamonds mark UV absorption-line detections of ionized HVCs in O VI (Sembach et al. 2003), Si II and Si III (Shull et al. 2009), and high-ion species at ~ 15 kpc (Lehner & Howk 2011), respectively. Reproduced from Putman et al. (2012).

Galactic sky at Galactocentric distances of at least $d \gtrsim 20$ kpc (Mishra et al. 2025; Nidever et al. 2010; Putman et al. 2003b). It is estimated to contain $M_{\rm HI} \sim 3 \times 10^8\ M_\odot$ (Brüns et al. 2005) in the neutral phase and $\sim 10^9\ M_\odot$ in ionized gas (Fox et al. 2014) (assuming $d = 55$ kpc), making it the most massive HVC complex in the Milky Way halo.

In the neutral phase, HVCs cover $\sim$ 37% of the sky in H I emission at $N_{\rm HI} \sim 7 \times 10^{17}\ {\rm cm}^{-2}$ level (Murphy et al. 1995). UV absorption observations, which are sensitive to much lower column density gas, reveal that multiphase HVCs cover a substantially larger fraction of the sky: $\sim 80\%$ in Si III tracing photoionized gas at $\sim 10^4$ K (Shull et al. 2009), and $\gtrsim 60\%$ in O VI tracing collisionally ionized gas at $T \sim 10^{5-6}$ K (Sembach et al. 2003). This ionized component likely dominates the total mass of the halo cloud population (Lehner & Howk 2011; Putman et al. 2012). Together, HVCs and IVCs represent the halo gas population closest to the disk and the most directly relevant to the fueling of Galactic star formation.

Whether this halo gas can actually sustain Galactic star formation depends on its mass, its survival as it travels through the hot halo, and its ability to cool and condense onto the disk. Current observational estimates of the total ionized gas inflow rate, derived from UV absorption, are $\dot{M}_{\rm in} \sim 0.5\ M_{\odot}\ {\rm yr}^{-1}$ (Fox et al. 2019; Lehner & Howk 2011), a substantial but incomplete fraction of the Milky Way's current star formation rate of $\sim 1-2\ M_{\odot}\ {\rm yr}^{-1}$ (Chomiuk & Povich 2011; Licquia & Newman 2015). These estimates depend critically on the assumed metallicity of the inflowing gas. If a substantial fraction of inflowing HVCs are more metal-rich than this fiducial value, as suggested by recent measurements of dust-enriched and super-solar HVCs in the inner Galaxy (Cashman et al. 2023; Fox et al. 2023), the true inflow rate would be correspondingly lower. For the neutral component, the total H I mass in the HVC population is of order $\sim 10^8\ M_{\odot}$ (Putman et al. 2012), which alone would be depleted in $\sim 50-100$ Myr at the current star formation rate. Hydrodynamic simulations of HVCs traveling through the hot halo further show that low-mass H I clouds are efficiently disrupted by Kelvin-Helmholtz instabilities and thermal interaction with the hot ambient medium, losing their H I content ~ 10 kpc of their starting position (Heitsch & Putman 2009). The ionized envelopes surrounding these neutral clouds may provide an alternative channel. Cosmological simulations find the ionized component to be roughly six times more massive than the H I, and if this ionized gas can cool efficiently onto the disk, it could supply as much as $\sim 80\%$ of the Galactic star formation rate (Lucchini et al. 2025). Whether this ionized material actually cools and condenses to form stars, however, remains an open question, and is a key uncertainty in the Milky Way's baryon cycle.

Beyond the question of how much halo gas reaches the disk, there is the question of *what kind* of gas it is. The metallicity of HVCs and IVCs provides the primary observational handle on the chemical signature of the material available for future star formation, and on its physical origin. IVCs are predominantly near-solar in metallicity and are therefore thought to trace material recycled through a Galactic fountain (Richter 2017; Wakker 2001, also see Section 3.2). HVCs are predominantly metal-poor ($Z \sim 0.1-0.3\ Z_{\odot}$), such as Complex C (Collins et al. 2007; Fox et al. 2023; Tripp et al. 2003; Wakker et al. 1999), points to accretion of relatively pristine gas from the IGM (Section 3.1) or from disrupted satellites. The Magellanic Stream adds a third, distinct origin channel, gas stripping from satellites (Section 3.3). Its two filaments have metallicities of $\sim 0.1\ Z_{\odot}$ (Fox et al. 2013) and $\sim 0.5\ Z_{\odot}$ (Richter et al. 2013), roughly consistent with SMC and LMC origins.

Recent kinematic modeling of large HVC and IVC samples, however, suggests that the velocity-based division between the two populations does not map cleanly onto physical origin. The data are better described by a unified population participating in the same fountain cycle, with both inflowing and outflowing components at a range of velocities (Marasco et al. 2022). The metallicity spread within the HVC/IVC population, in this picture, reflects the ongoing mixing of ejected disk material with lower-metallicity halo gas.

4.2 Milky Way Chemical Evolution and the Need for Metal-Poor Accretion

The metallicity of gas reaching the Milky Way disk is not just a flow diagnostic; it is a fundamental input to Galactic chemical evolution. The closed-box model (Pagel 1997; Schmidt 1963), in which a galaxy evolves as an isolated system, predicts a far larger fraction of low-metallicity G-dwarfs in the solar neighborhood than is observed, the long-standing "G-dwarf problem" (Pagel & Patchett 1975). The standard resolution requires sustained inflow of metal-poor gas. Continued accretion regulates the ISM metallicity and extends star formation over a long period of moderate enrichment, bringing the predicted metallicity distribution into agreement with observations (Larson 1972; Pagel 1997). Modern Galactic chemical evolution models build on this. The two-infall picture of Chiappini et al. (1997), in which the thick disk forms during an early rapid infall and the thin disk during a later, slower one, is supported by the observed α/Fe bimodality in APOGEE and asteroseismic data (Matteucci 2021; Spitoni et al. 2019), and requires gas accretion below the contemporaneous ISM metallicity in both phases. The same requirement appears in equilibrium models of the mass-metallicity (Maiolino & Mannucci 2019; Tremonti et al.

2004) and fundamental metallicity (Mannucci et al. 2010) relations: these are reproduced only if inflow and outflow metallicities are systematically offset (Andrews et al. 2017; Davé et al. 2012; Lilly et al. 2013).

Whether the present-day Milky Way ISM is itself chemically uniform remains an open question. De Cia et al. (2021) reported metallicity variations of ~ 0.5 dex among nearby sight lines, attributing the low-metallicity material to inefficient mixing of metal-poor HVC infall with the disk. Ritchey et al. (2023), applying a different dust-depletion analysis to a larger sample, instead found a small dispersion of ~ 0.10 dex and concluded that the local ISM is well mixed and chemically homogeneous. The disagreement turns on the treatment of dust depletion and unresolved saturation, with Ritchey et al. (2023) showing that several of the lowest-metallicity sight lines in the De Cia et al. (2021) sample are consistent with solar metallicity once these effects are accounted for. Either way, the metallicity of inflowing gas is the key input. In the De Cia et al. (2021) picture it appears as ISM diversity, while in the Ritchey et al. (2023) picture it is rapidly mixed into the disk, contributing to ISM dilution without leaving distinct chemical signatures.

The chemical evolution picture for the Milky Way, thus, requires sustained accretion of gas with metallicity systematically lower than the present ISM. How far below solar the inflowing gas is sets how much dilution it can provide. This raises a sharp question: *Is the gas actually arriving at the disk metal-poor enough to satisfy the chemical evolution picture?* The conventional answer, based on the $\sim 0.15\ Z_\odot$ metallicity measured in the well-studied metal-poor HVC Complex C, has been yes. But if a substantial fraction of the gas reaching the disk is recycled fountain material with near-solar or super-solar metallicity, as the IVC population suggests (Section 4.1), the inflow-averaged metallicity could be much higher than the standard picture assumes.

4.3 Open Questions

The picture sketched in Sections 4.1–4.2 leaves several specific questions about the Milky Way's inner atmosphere unresolved. Three are central to this dissertation.

Q1. What are the metallicities of the diffuse ionized gas at the disk-halo interface, and what do they imply for its origin?

Most metallicity measurements of halo clouds target the dense, high-column-density regions detectable in 21 cm emission, leaving the more diffuse ionized envelopes that dominate the gas mass (Lehner & Howk 2011; Putman et al. 2012) poorly characterized. The dominant uncertainty is determining the total hydrogen column density, $N_{\rm H} = N_{\rm HI} + N_{\rm HII}$. The ionized component $N_{\rm HII}$ is rarely measured directly and must instead be inferred through photoionization modeling, which requires assumed values for the gas density and ionizing radiation field. How the metallicities of this diffuse ionized phase compare with those of the dense neutral cores, and whether they support or revise the metal-poor inflow/metal-rich outflow picture at the disk-halo interface, are open questions.

Q2. How does gas mix and accrete through the galactic fountain at the disk-halo interface?

Fountain models predict that disk material ejected into the halo cools, mixes with ambient halo gas, and returns to the disk on timescales of few Myrs (Section 3.2). The metallicity, ionization state, and kinematics of the returning gas should encode the efficiency of this mixing: pure recycled material returns at near-disk metallicity, while gas that has substantially mixed with the lower-metallicity halo returns at intermediate values. Whether observed fountain-candidate clouds at the disk-halo interface bear out these predictions, and how much of the mass returning to the disk is dominated by recycled fountain gas versus newly accreted material, remain open questions.

Q3. What is the mass budget and ultimate fate of the Magellanic Stream?

If it survives its journey to the disk, the Magellanic Stream may be the most significant near-future accretion event for the Milky Way. The H I component alone, $\sim 3 \times 10^8\ M_\odot$ (Brüns et al. 2005), is already comparable to the present-day H I content of the LMC, and even more mass in the ionized envelope (Fox et al. 2014). These mass estimates, however, are tied to assumed Stream distances, which span a wide range from $\sim$ 20–100 kpc depending on the formation scenario (e.g., Besla et al. 2012). The recent discovery of a Magellanic Corona around the LMC (Krishnarao et al. 2022; Lucchini et al. 2020) adds a further dimension. The ionized component of the Stream may reflect the LMC's own pre-infall gaseous halo as much as its interaction with the Milky Way. The Corona may have contributed to the formation of the ionized Stream as it was stripped during the LMC's infall. The total mass, the ionization and cooling history of the gas, and what fraction of it will eventually reach the Galactic disk, are open questions central to predicting how this accretion event will unfold.

5 Dissertation Outline

This dissertation comprises three projects addressing the chemical and ionization properties of gas flows at the Milky Way's inner halo. Each project uses UV absorption spectroscopy, primarily HST/COS data, combined with detailed photoionization modeling and, where possible, independent constraints from H I 21 cm emission and pulsar dispersion measures.

In Chapter 2, I constrain the metallicity of the diffuse ionized gas at the Milky Way's disk-halo interface using sight-line pairs of UV-bright halo stars and pulsars in the same globular clusters. The pulsar dispersion measures provide a precise constraint on the electron column density along the same line of sight as the UV absorption, constraining the ionization correction to total hydrogen and breaking the degeneracy between ionization parameter and metallicity that has limited estimates. I address the blending of disk-halo interface gas with foreground Milky Way ISM through joint Voigt-profile fitting across all detected absorption components, and use detailed photoionization modeling to derive metallicities of the ionized clouds. I discuss the implications of the resulting metallicity distribution for the origin of the disk-halo interface gas and its role in the Galactic baryon cycle.

In Chapter 3, I investigate the chemical and kinematic properties of Complex K, a candidate Galactic fountain cloud at the disk-halo interface. I use archival HST/COS spectra of ~ 40 (?) background quasars and halo stars to probe Complex K across its full angular extent. I introduce a Bayesian Voigt-profile fitting and photoionization modeling code that jointly constrains column densities, kinematics, and gas-cloud parameters under informative priors from H I 21 cm emission and from pulsar dispersion measures along the Complex K direction. I use this code to map the metallicity, ionization, and kinematic structure of the cloud, and to test whether its properties are consistent with a galactic fountain origin and with the mixing of recycled disk material with the surrounding halo gas.

In Chapter 4, I search for an ionized extension of the Magellanic Stream on the northern side of the Galactic plane using HST/COS G160M spectra from the Plane Quasar Survey (Werk et al. 2024), which targets quasar sight lines at low Galactic latitudes ($|b| < 30°$) that have been largely unexplored in previous Milky Way CGM studies. I identify C IV absorbers whose position and kinematics align with the established Stream, and use the absence of low ions and the detected high-ion ratios to characterize the ionization conditions of the gas. I discuss the implications of this newly identified extension for the total ionized gas mass of the Stream, for its formation and recent dynamical history, and for the orbital direction of the Magellanic Clouds.

Chapter 5 summarizes the findings of these three projects, places them within the broader context of the Milky Way's baryon cycle, and outlines directions for future work.

Chapter 2

Metallicity Mapping of the Ionized Diffuse Gas at the Milky Way Disk–Halo Interface

Portions of this chapter were originally published in collaboration with Jessica K. Werk, Kirill Tchernyshyov, J. Xavier Prochaska, Yong Zheng, Mary E. Putman, Drummond B. Fielding, and Jay Strader in the December 2024 edition of the Astrophysical Journal (Choi et al. 2024, ApJ, Vol. 976, 222; 2024 © American Astronomical Society, DOI: 10.3847/1538-4357/ad84f8), and are reproduced below with the permission of the American Astronomical Society.

Summary

Metals in the diffuse, ionized gas at the boundary between the Milky Way's interstellar medium (ISM) and circumgalactic medium, known as the disk-halo interface (DHI), are valuable tracers of the feedback processes that drive the Galactic fountain. However, metallicity measurements in this region are challenging due to obscuration by the Milky Way ISM and uncertain ionization corrections that affect the total hydrogen column density. In this work, we constrain the ionization corrections to neutral hydrogen column densities using precisely measured electron column densities from the dispersion measure of pulsars that lie in the same globular clusters as UV-bright targets with high-resolution absorption spectroscopy. We address the blending of absorption lines with the ISM by jointly fitting Voigt profiles to all absorption components. We present our metallicity estimates for the DHI of the Milky Way based on detailed photoionization modeling of absorption from ionized metal lines and ionization-corrected total hydrogen columns. Generally, the gas clouds show a large scatter in metallicity, ranging between $0.04-3.2\ Z_{\odot}$, implying that the DHI consists of a mixture of gaseous structures having multiple origins. We estimate the inflow and outflow timescales of the DHI ionized clouds to be $6-35$ Myr. We report the detection of an infalling cloud with super-solar metallicity that suggests a Galactic fountain mechanism, whereas at least one low-metallicity outflowing cloud ($Z < 0.1\ Z_{\odot}$)

poses a challenge for Galactic fountain and feedback models.

1 Introduction

Gas depletion times of only a few hundred Myrs for star-forming galaxies at $z = 1 - 3$ have raised the question of how galaxies fuel and sustain their star formation over Gyrs of cosmic evolution (Saintonge et al. 2013). The answer is likely to lie in the circumgalactic medium (CGM), a massive reservoir of baryons and metals that extends hundreds of kpc from a galactic disk (Tumlinson et al. 2017). The idea that gas accretion from the CGM continuously fuels the star formation observed in the interstellar medium (ISM) of galaxies has been indirectly supported by numerous observations indicating that cool, ionized gas ($T \sim 10^4$ K) is ubiquitous in low-redshift, L* galaxies out to ∼150 kpc with a characteristic total mass of $M_{\rm cool,CGM} \sim 10^{10-11}\ M_\odot$ (e.g. Prochaska et al. 2017a; Werk et al. 2014). At the same time, the CGM contains metals ejected through outflows by stellar and/or active galactic nuclei (AGN) feedback (e.g. Peeples et al. 2014), and thus plays an essential role in the baryon cycle that drives galaxy evolution.

The Milky Way is an ideal place to test our understanding of gas accretion, recycling, and outflows (collectively called the “baryon cycle") with numerous, high-quality observational datasets of its multiphase ISM, CGM, and the boundary region between the two, known as the disk-halo interface (DHI). Neutral gas clouds moving at radial velocities in the local standard of rest frame (LSR) inconsistent with Galactic rotation have been discovered and catalogued in H I 21 cm emission surveys (e.g. Kalberla et al. 2005; Putman et al. 2002; Winkel et al. 2016). They are commonly referred to as intermediate-velocity clouds (IVCs; $20 \lesssim |v_{\rm LSR}| \lesssim 90\ {\rm km\ s^{-1}}$) or high-velocity clouds (HVCs; $|v_{\rm LSR}| > 90\ {\rm km\ s^{-1}}$) and mostly lie at $d \lesssim 20$ kpc (Putman et al. 2012; Richter 2017; Wakker 2001), placing them in this DHI region.

The infalling cold gas clouds provide valuable information about the gas accretion into the galaxy (Fox et al. 2019; Lehner & Howk 2011). Their origin could be outside of the Milky Way such as gas accretion from the intergalactic medium (IGM) (Fumagalli et al.

2011; Rees & Ostriker 1977) or from satellites. Alternatively, these cold clouds can form in a "Galactic fountain" mechanism in which metal-rich outflowing gas driven by feedback processes mixes with metal-poor halo gas, stimulating the halo gas to cool and fall back to the disk (Fraternali 2017; Shapiro & Field 1976).

In order to understand the origin of gas accretion and the physical processes that power the Galactic fountain, we must simultaneously study the ionized and neutral gas at the DHI that exhibit similar line-of-sight velocities. Observations of Hα emission from warm gas ($T \sim 10^{4-5}$ K) have revealed its prevalence in the DHI region (d $\lesssim$ 3 kpc) and find that the ionized gas is likely related to the Galactic star formation activities (Fang et al. 2006; Haffner et al. 2003; Wang & McCray 1993). The most sensitive probe of this ionized gas at the DHI is ultraviolet (UV) absorption line spectroscopy using background sources like quasars or halo stars. UV absorption studies have uncovered that ionized gas spreads out over a larger spatial extent than its kinematically-associated neutral gas (e.g. Lehner et al. 2022; Sembach et al. 2003; Shull et al. 2009). The ionized gas shows both inflows and outflows, implying that it contains a significant amount of material that could eventually accrete onto the disk and fuel future Galactic star formation (Fox et al. 2019; Lehner & Howk 2011; Lehner et al. 2012).

The detailed kinematic study of ionized gas clouds can provide crucial information about their origin and allow us to draw a picture of physical processes at the DHI. For example, Fox et al. (2003) detected several highly ionized gas clouds along a halo O-star line of sight in O VI, N V, C IV, and Si IV, all having complex absorption-line profiles that vary by ion species. While narrow C IV and Si IV lines trace photoionized gas, broader line profiles are indicative of collisionally ionized gas at the boundary between neutral/warm gas clouds and the surrounding hot medium. Furthermore, recent kinematic studies of warm, ionized gas at the DHI show that its distribution and kinematics, such as the observed velocity gradients of inflows, can be favorably explained by the Galactic fountain (e.g. Bish et al. 2019; Marasco et al. 2022; Werk et al. 2019). This suggests that the Galactic fountain may play a dominant role not only in driving outflows but also in gas accretion to the Milky Way disk, although further investigation is required.

Another way to constrain the origin of DHI gas is to measure its metallicity. For example, a gas-phase metallicity of a few percent solar would indicate accretion from a more metal-poor source like the IGM, while metallicities closer to solar would imply a Galactic origin. However, measuring the metallicity of ionized gas at the DHI is challenging due to poor constraints on the total amount of hydrogen in this region. Studies that measure the metallicity of neutral HVCs and IVCs have been exclusively done by using H I 21 cm observations for the clouds with $N_{\rm HI} \gtrsim 7 \times 10^{17}\ {\rm cm}^{-2}$ (Collins et al. 2007; Sembach et al. 2001; Wakker 2001; Wakker et al. 1999), assuming a negligible ionization correction. Yet the ubiquitous ionized gas clouds in this region are dominated by ionized hydrogen rather than neutral hydrogen, preferably having lower $N_{\rm HI} \lesssim 10^{17}\ {\rm cm}^{-2}$ and unlikely to be detected with H I 21 cm observation. Alternatively, several metallicity studies for ionized gas at the DHI have been taken with hydrogen Lyman series absorption lines in far-UV (FUV) (Cashman et al. 2023; Fox et al. 2005; Zech et al. 2008). Given that the ionized hydrogen likely dominates the total hydrogen column, however, there exists considerable uncertainty in the gas ionization fractions without an independent constraint on ionized hydrogen column density $N_{\rm HII}$.

Howk et al. (2006) were the first to suggest the idea of using the radio dispersion measure (DM) of pulsars to address this issue. The pulsar DM provides a precise value of the electron column density N_e which can effectively serve as an independent constraint on $N_{\rm HII}$ with a correction for helium content. For sight lines toward globular clusters (GC) that include both UV bright stars and radio pulsars, the metallicity of gas can be measured with great precision by combining constraints from UV absorption lines of metal ions, hydrogen Lyman series lines, and the pulsar DM. Howk et al. (2006) successfully measured the overall metallicity of multiphase gas in the sightline toward M3 with this method. However, this work did not separately analyze different gas components at distinct radial velocities (e.g., the Milky Way ISM, IVCs at the DHI) that might have different origins and possibly exhibit variations in metallicity.

In this paper, we build on the method first suggested by Howk et al. (2006) in order to investigate the metallicity of ionized gas at the DHI for a larger sample of sight lines toward the halo GCs. We use archival FUV spectra of UV bright stars in the GCs observed with the Cosmic Origin Spectrograph (COS) or the Space Telescope Imaging Spectrograph (STIS) installed on the *Hubble Space Telescope* (*HST*). We describe our data in Section 2. We separately measure the metallicity of each kinematically-distinct gas cloud by performing Voigt profile fitting (Section 3) and photoionization modeling (Section 4) with an independent $N_{\rm HII}$ constraint given by the pulsar DM. Our results are given in Section 3, and we discuss the origin of ionized gas clouds at the Milky Way DHI in Section 4.

2 Data

2.1 Target Selection

To select targets for this experiment, we first referred to a comprehensive pulsar catalog [1] by Paulo Freire to obtain a list of GCs for which pulsar DMs are available. The pulsar DM can be converted to the electron column and serves as a strict upper limit on the total electron column density of ionized gas along the sight line. Ultimately, this electron column will be converted to a constraint on the H II column density of ionized gas at the Milky Way DHI that will in turn, allow us to measure the metallicity at the DHI. The electron column densities for each line of sight are presented in Table 2.5 in Appendix 8 with references.

We performed an archival search in the Barbara A. Mikulski Archive for Space Telescopes (MAST) for existing high-resolution FUV spectra of UV-bright stars in those GCs. They are post-AGBs that have a continuum with less metal lines, making them a proper

[1] `https://www3.mpifr-bonn.mpg.de/staff/pfreire/GCpsr.html`

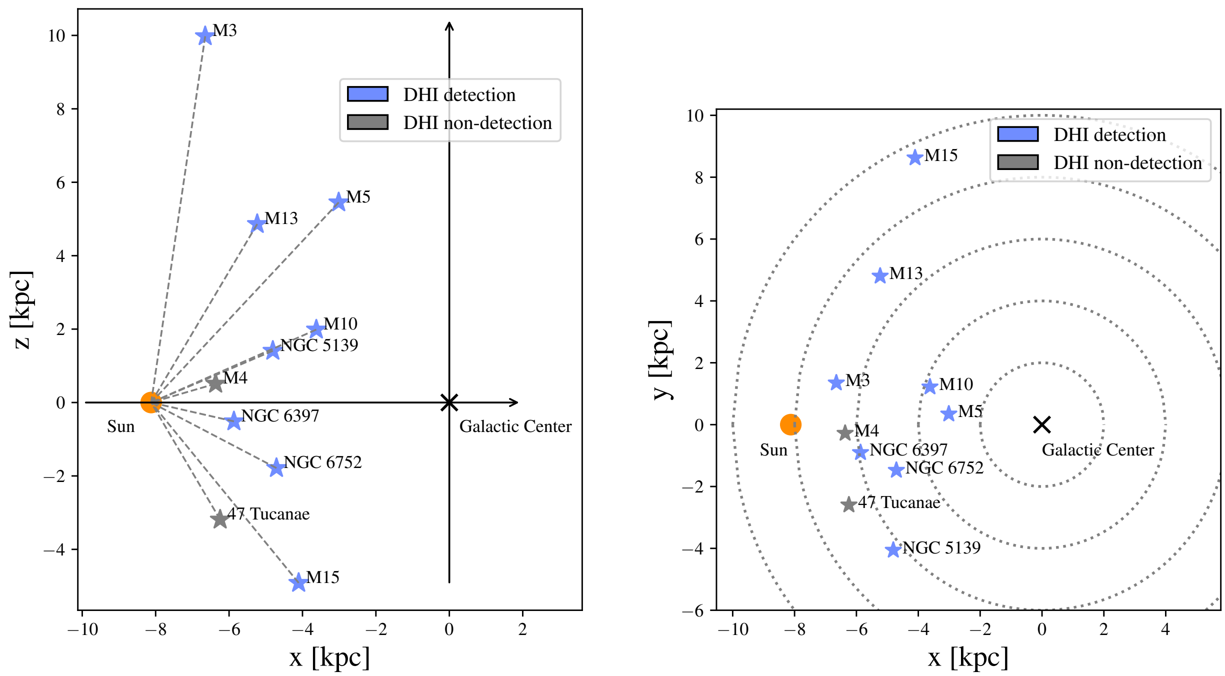

(a) XZ plane (b) XY plane

Figure 2.1: 3D distribution of the targeted GCs in the Galactocentric system where the Galactic center lies at (0, 0, 0) kpc and the Sun is at (-8.122, 0, 0) kpc. We mark the GC sight lines where IVCs or/and HVCs are detected in the UV spectrum as "DHI detection" (blue star). A "DHI non-detection" (gray star) indicates that gas kinematically distinct from the Milky Way ISM was not present in the spectrum.

background source. Table 2.1 lists the ten lines of sight toward globular clusters with pulsar DM measurements for which we were able to obtain FUV spectra. In order to ensure the cluster membership of the UV-bright stars, we only selected the targets of which membership is well studied (e.g. Chayer et al. 2015; Dixon et al. 2019; Moehler et al. 2019), and confirmed that their (photo)geometric distances estimated with *Gaia* DR3 (Bailer-Jones et al. 2021) are comparable to the distances to the GCs (Baumgardt & Vasiliev 2021).

The selected targets all lie at Galactic heights of $z \lesssim 10$ kpc (Table 2.1) and thus serve as lines of sight sensitive to the DHI. Their spatial distribution with respect to the Milky Way disk is shown in Fig. 2.1. We note that, here, we refer to and use the distance to the clusters as the distance to the targets, considering the confidence in their cluster membership and errors on the order of a few kpc in the Gaia distances to the individual stars.

2.2 *HST/COS and STIS*

The majority of our archival data are FUV spectra observed with the *HST*/COS G130M and 160M gratings. The wavelength coverage spans 1132-1775 Å with a characteristic spectral resolution of $R \sim 12,000 - 20,000$. The relatively high S/N (S/N > 30) of the FUV spectra allows us to analyze a number of absorption lines from low ions (e.g., O I, C II, Si II, Si III) and intermediate ions (e.g., Si IV, C IV, N V) that trace the warm ionized gas at the DHI.

For the two sight lines M5 and NGC 6397, *HST*/STIS E140M data are available. These high S/N spectra cover wavelengths of 1144–1730 Å with a characteristic spectral resolution of $R \sim 30,000$, corresponding to a velocity resolution of $\sim 10 \text{ km s}^{-1}$. We continuum-normalize all COS co-added spectra from the HSLA (Peeples et al. 2017a) and STIS spectra using “lt_continuumfit" a Python tool in the open-source package `Linetools` (Prochaska et al. 2016).

2.3 *FUSE*

Far Ultraviolet Spectroscopic Explorer (FUSE) spectra are available for six lines of sight (Table 2.1). The spectra were obtained with the SiC2A, LiF1A, and LiF2A channels, with segments that cover 916-1005 Å, 987-1082 Å, and 1086-1181 Å, respectively, with a spectral resolution of $R \sim 10,000 - 20,000$. This wavelength range covers additional metal ions such as S III and Fe III that are unavailable in the COS or STIS spectra.

Furthermore, *FUSE* spectra provide a constraint on H I column density. Although we focus on ionized clouds close to the disk where H II likely accounts for a significant fraction of the total hydrogen, the H I column density ($N_{\rm HI}$) is an important, additional constraint on the photoionization modeling that is discussed in Section 4.

A way to precisely to measure H I column density of the absorbing clouds is using H I Lyman series absorption lines in high-resolution FUV spectra. Although recent all-sky H I 21 cm surveys such as the Leiden/Argentine/Bonn survey (LAB; Kalberla et al. 2005) and the HI4PI survey (HI4PI Collaboration et al. 2016) have been successfully used to measure $N_{\rm HI}$ of neutral-gas bearing clouds in emission, these data offer only coarse constraints on the $N_{\rm HI}$ for two reasons. First of all, these surveys have an effective beam size of 10 - 30′ which is at least several tens of times larger than the HST/COS aperture (2.5″) or STIS (0.2″) and possibly gives a larger or smaller value of $N_{\rm HI}$ due to beam smearing (Howk et al. 2006). Additionally, we were not able to detect any possible IVCs and HVCs from both LAB and EBHIS data for most of our sample lines of sight, indicating that the ionized clouds we are finding either have $N_{\rm HI}$ below the detection limit of H I surveys of $N_{\rm HI} \gtrsim 10^{18}$ cm^{-2} and/or are small and thus spatially-unresolved (Richter 2017). We finally note that $N_{\rm HI}$ measurements on the order of 10^{15-18} cm^{-2} would be consistent with several previous studies on ionized gas clouds at the DHI (Cashman et al. 2023; Collins et al. 2004; Zech et al. 2008). Therefore, we use the FUSE spectra to measure H I Lyman series absorption lines with wavelengths shorter than Lyγ down to Lyμ at 916 Å to probe $N_{\rm HI}$ of $\sim 10^{14-16}$ cm^{-2}.

Table 2.1: Archival FUV spectral data

GC	Star	l (°)	b (°)	z_{GC} (kpc)	z_* (kpc)	Instrument	Grating	S/N	Detection	Proposal ID
M5 (NGC 5904)	NGC5904-KUST723	3.86	46.79	5.47	$4.12^{+3.84}_{-1.36}$	STIS	E140M	29.81	✓	9410
	....	......	.....	.....	....	FUSE	SiC2A/LiF1A/LiF2A	10.94	....	D157
M10 (NGC 6254)	NGC6254-ZNG1	15.16	23.09	1.74	$2.68^{+0.42}_{-0.32}$	COS	G130/160M	41.48	✓	13721
M3 (NGC 5272)	NGC5272-ZNG1	42.50	78.68	10.02	$10.94^{+3.37}_{-2.55}$	COS	G130/160M	36.98	✓	11527
	....	......	.....	.....	....	FUSE	SiC2A/LiF1A/LiF2A	13.96	....	P101
M13 (NGC 6205)	NGC6205-ZNG1	58.97	40.94	4.67	$5.90^{+1.76}_{-1.27}$	COS	G130/160M	56.60	✓	11527
	....	......	.....	.....	....	FUSE	SiC2A/LiF1A/LiF2A	12.02	....	P101
M15 (NGC 7078)	NGC7078-ZNG1	65.04	-27.29	-4.76	....	COS	G130/160M	40.90	✓	11527
	[J76] B212734.4+115714	65.02	-27.31	-4.76	$-2.32^{+0.71}_{-1.24}$	FUSE	SiC2A/LiF1A/LiF2A	8.50	....	D157
47 Tucanae (NGC 104)	NGC104-BS	305.91	-44.88	-3.24	$-3.65^{+1.28}_{-2.18}$	COS	G130/160M	36.63	✗	13721
ω Centauri (NGC 5139)	NGC5139-ROA-5701	309.24	15.05	1.36	$1.62^{+0.33}_{-0.20}$	COS	G130/160M	40.32	✓	12032
NGC 6752	NGC6752-BUON-1754	336.62	-25.64	-1.72	$-2.92^{+0.72}_{-0.80}$	COS	G130/160M	57.56	✓	12032
	....	......	.....	.....	....	FUSE	SiC2A/LiF1A/LiF2A	7.46	....	C076
NGC 6397	NGC6397-ROB162	338.19	-11.94	-0.46	$-0.48^{+0.03}_{-0.03}$	STIS	E140M	41.94	✓	9410
	....	......	.....	.....	....	FUSE	SiC2A/LiF1A/LiF2A	7.22	....	A026
M4 (NGC 6121)	NGC6121-Y453	350.98	16.05	0.62	$0.58^{+0.06}_{-0.06}$	COS	G130/160M	32.53	✗	13721

Note. The 10 sight lines toward the halo GCs of which both pulsar DM and UV spectral data are available. The Galactic coordinates (l, b) and height from the disk of the targeted GCs (z_{GC}) and UV bright stars (z_*) are presented. We detect IVCs and/or HVCs for 8 of the sightlines (checkmark). All the data presented here can be found in MAST:https://doi.org/10.17909/k15n-zp34.

3 Ion Column Density Measurements

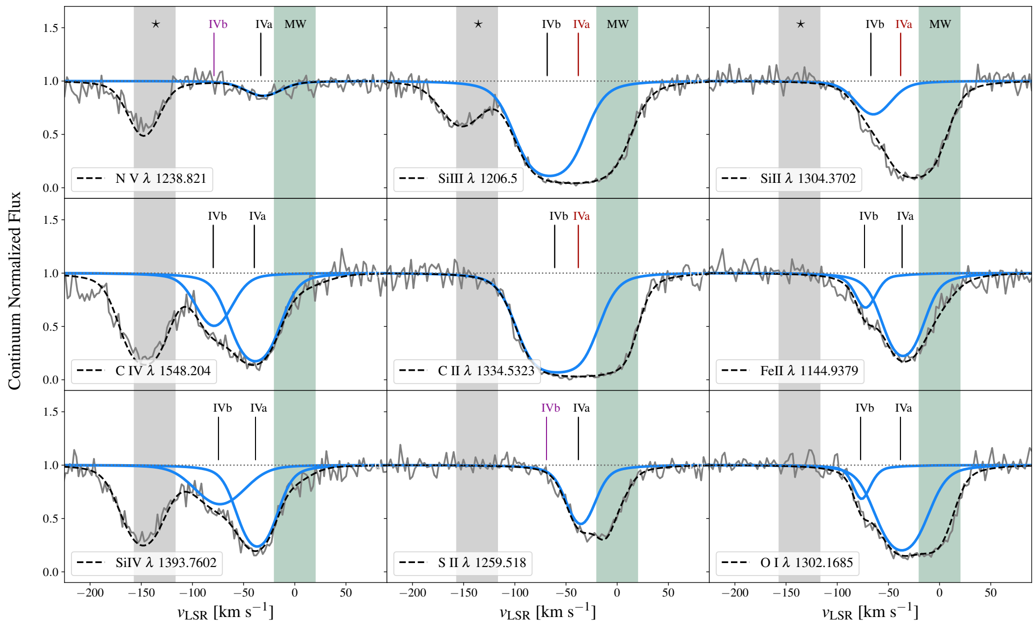

Figure 2.2: The Voigt profile fit for the M3 sight line (NGC5272-ZNG1). The Black dashed line shows the joint fit including all the absorption components. We separate two intermediate velocity gas clouds, IVa and IVb (blue-solid lines), from the Milky Way ISM (green-shaded) and star (gray-shaded). The component labeled IVa is well-detected in highly-ionized metal species, but is severely blended with saturated absorption from the Milky Way in a few low-ionization metal species (red labels), which makes it impossible to constrain gas column densities from those absorption lines. We mark IVC non-detections in a given ion species with a purple label.

We apply Voigt profile fitting to the ion absorption lines detected in the continuum-normalized UV spectra to precisely measure the ion column densities. In order to measure the metallicity of ionized gas clouds at the DHI, the absorption features that originate from ionized gas clouds need to be separated from the Milky Way ISM absorption or stellar absorption. Because the only distance information on gas clouds is an upper limit constraint from the background GCs, we identify the absorption features in velocity space, in the LSR rest frame. The components with $|v_{\rm LSR}| \leq 20$ km s^{-1} are classified as the Milky

Way ISM absorption, and the components with $|v_{\rm LSR} - v_{\rm star}| \leq 20$ km s^{-1} are regarded as stellar absorption. We adopt the terminology of IVC and HVC to refer to components of which absolute LSR velocity is $20 < |v_{\rm LSR}| \leq 90$ km s^{-1} and $|v_{\rm LSR}| > 90$ km s^{-1}, respectively (Putman et al. 2012; Wakker 2001; Werk et al. 2019). For defining IVCs, a lower velocity limit of 40 km s^{-1} is more generally accepted, as velocities below this threshold can be indistinguishable from galactic rotation on certain sight lines (e.g. van Woerden et al. 2004). However, we adopt a lower value of 20 km s^{-1} to maximize the detection of clouds distinguishable from the ISM and to maintain a consistent threshold across all samples.

We identify all the absorption components within $|v_{\rm LSR}| < 400$ km s^{-1} using `pyigm`[2] `IGMGuesses` GUI, which shows each absorption line in velocity space, allowing us to easily identify components by eye using velocity offsets. Also, it makes the first estimate of Voigt profile parameters for each ion species: ion column density $N_{\rm ion}$, Doppler parameter b, and $v_{\rm LSR}$. Some absorption features are saturated; given that the line-spread function of the COS instrument features a broad core and extended wings, compared to Gaussian, the line profile convoluted with the COS line-spread function typically exhibits a peak value about 0.8 times that of an equivalent Gaussian profile (Ghavamian et al. 2009). Therefore, we defined a feature as saturated if there were three or more consecutive pixels with flux values below the normalized flux of 0.2. If multiple lines are available for the ion species, we select the line with the lowest oscillation strength for the identification to avoid saturation and minimize uncertainty in the measurements.

We detect HVCs and/or IVCs in the sight lines toward 8 of 10 GCs. We consider it a detection when absorption components of at least three different ions are identified for robustness. We note that, despite the lower velocity threshold of $|v_{\rm LSR}| < 20$ km s^{-1}, all detected IVCs are found at $|v_{\rm LSR}| > 35$ km s^{-1}, aligning closely with the more commonly considered threshold (Table 2.5 in Appendix 8). With the initial values given by `IGMGuesses`, we jointly fit Voigt profiles for every absorption component using a public python package

[2] `https://github.com/pyigm/pyigm`

Table 2.2: Voigt profile measurements and ion column densities for the M3 line of sight.

Comp.	Ion	$\log N$ ($\mathrm{cm^{-2}}$)	b ($\mathrm{km\ s^{-1}}$)	v_{LSR} ($\mathrm{km\ s^{-1}}$)
Total	e^-	$<^{a}19.91 \pm 0.01$	....	....
IVa	H I	$> 16.96 \pm 0.16$	....	....
	O I	$> 14.81 \pm 0.07$	21.8 ± 5.3	-38.3 ± 2.7
	Fe II	14.92 ± 0.02	27.9 ± 0.8	-37.5 ± 0.7
	S II	14.83 ± 0.04	12.5 ± 1.9	-38.0 ± 1.7
	Fe III	14.40 ± 0.08	19.8 ± 2.9	-45.8 ± 1.7
	S III	14.41 ± 0.10	21.9 ± 3.5	-23.7 ± 4.1
	Si IV	13.63 ± 0.11	16.9 ± 3.1	-38.2 ± 1.8
	C IV	14.21 ± 0.06	19.6 ± 3.5	-39.6 ± 1.7
	N V	13.15 ± 0.05	19.1 ± 4.3	-33.2 ± 2.6
IVb	H I	$> 16.92 \pm 0.16$	....	....
	O I	13.92 ± 0.29	8.6 ± 5.7	-73.1 ± 4.1
	Fe II	14.02 ± 0.12	4.0 ± 0.9	-73.3 ± 1.0
	Si II	14.23 ± 0.06	26.2 ± 2.7	-76.7 ± 3.2
	S II	$< 14.63 \pm 0.03$	....	....
	C II	$> 14.64 \pm 0.22$	27.0 ± 3.4	-61.9 ± 7.5
	Fe III	13.82 ± 0.23	21.9 ± 7.9	-81.4 ± 8.9
	Si III	$> 13.61 \pm 0.28$	25.2 ± 5.3	-68.4 ± 11.0
	S III	13.75 ± 0.45	18.0 ± 9.1	-56.3 ± 11.5
	Si IV	13.17 ± 0.30	28.0 ± 13.0	-74.6 ± 15.6
	C IV	13.64 ± 0.14	17.8 ± 4.9	-79.7 ± 4.9
	N V	$< 12.55 \pm 0.19$	....	....

[a]Pulsar DM by Hessels et al. (2007)
Note. Properties of all the detected absorption lines in the sight line toward M3. The two IVCs are detected at $v_{\mathrm{LSR}} \sim -37\ \mathrm{km\ s^{-1}}$ and $\sim -70\ \mathrm{km\ s^{-1}}$ which are IVa and IVb, respectively. The electron column density given by pulsar DM is the total column density for this sight line. $\log N$ is ion column density, and b is the Doppler parameter of the absorption line.

`veeper`[3]. We present the best-fit Voigt profiles for the M3 sight line (NGC5272-ZNG1) as an example in Fig. 4.2. In Fig. 4.2, the green-shaded band is the Milky Way ISM absorption, and the gray-shaded band shows stellar absorption. For this sight line, we detect two IVCs, 'IVa' at $v_{\mathrm{LSR}} \sim -37\,\mathrm{km\,s^{-1}}$ and 'IVb' at $\sim -70\,\mathrm{km\,s^{-1}}$. Blue-solid lines show the best-fit Voigt profile for each component marked with black labels. We also mark 'no-information' absorption lines with the red label in cases of severely blending with the Milky Way ISM and 'non-detections' with the purple label. Table 2.2 presents the corresponding best-fit

[3]The original version of `veeper`: `https://github.com/jnburchett/veeper`. In this work, we use a custom version (`https://github.com/mattcwilde/veeper`).

parameters of the Voigt profile for each ion species. The ion column density measurements determined by fitting Voigt profiles for all the sight lines are presented in Table 2.5 in Appendix 8. We present lower or upper limits for several ions because of saturation or non-detection, respectively. For the saturated lines, the measured column density is taken as a lower limit. In the case of a non-detection, an upper limit is estimated by the apparent optical depth method (AODM; Savage & Sembach 1991) with the 2σ level of significance (95 % confidence). Please refer to Bowen et al. (2008) for the detailed method.

We also constrain $N_{\rm HI}$ using H I Lyman series lines detected in absorption for M5, M3, M15, and NGC 6397 when a *FUSE* spectrum is available. We measure H I column density using the AODM applied to the Lyman absorption lines. Similar to the approach taken for other ion species, we select lines with the lowest oscillation strengths, specifically at $\lambda 916$, $\lambda 917$, and $\lambda 918$, to minimize saturation. Nevertheless, we consider these column density estimates as lower limits because the lines are still found to be saturated, and Voigt profile fitting is not appropriate considering their low S/N (Table 2.1).

4 Photoionization Modeling

Since the majority of detected ion species in our samples are low ions that may have undergone photoionization, we conduct photoionization modeling to correct for ionization effects, characterize the ionized clouds, and ultimately estimate their metallicity. We also detect intermediate ions, Si IV, C IV, and N V, that may be part of the photoionized warm gas ($T \sim 10^{4-5}$ K) or also may be in a collisionally-ionized transitional phase at $\sim 10^5$ K (Werk et al. 2019). Photoionization modeling is a valuable tool for understanding the behavior of intermediate ions. By applying a photoionization model, we can determine the extent to which the observations of the intermediate ions can be explained by photoionization, and evaluate the need for other mechanisms (e.g. turbulent mixing layers, shock ionization) to account for discrepancies.

The spectral synthesis code CLOUDY (Ferland et al. 2017) is used for photoionization

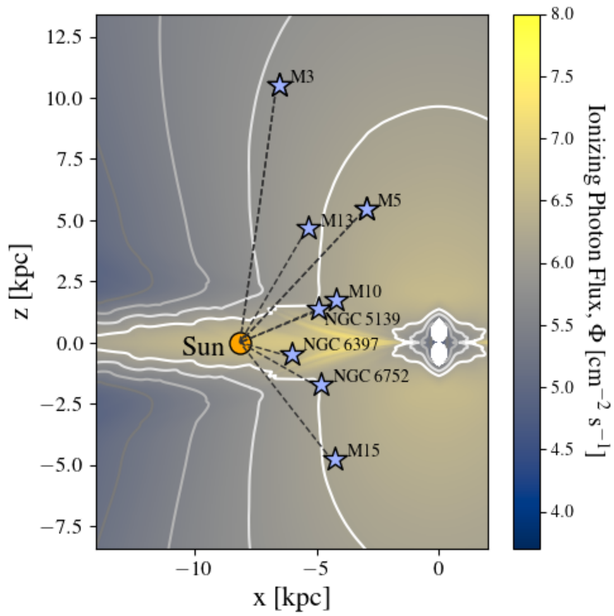

Figure 2.3: The Milky Way radiation field modeled by Fox et al. (2005), with the positions in xz space of our 8 targets marked by blue stars. The color scale indicates the level of the assumed ionizing photon flux, Log Φ, in units of photons cm^{-2} s^{-1}.

modeling. We use the Milky Way radiation model developed by Fox et al. (2005) as the ionizing source that includes stellar radiation and extragalactic background radiation (Fig. 2.3). We generate a grid of gas cloud models parameterized by neutral hydrogen column density $N_{\rm HI}$, metallicity $Z/Z_\odot$, and ionization parameter U, where the ionization parameter U is defined as the ratio between the number density of ionizing photons and hydrogen ($U \equiv n_\gamma/n_{\rm H} = \Phi/cn_{\rm H}$). The ionization parameter U is useful for our models because it inherently scales with both the ionizing photon flux and the hydrogen number density. Thus, U effectively incorporates the variations in ionizing flux that may arise from uncertainties in the distances to the clouds. Our grid spans $\log N_{\rm HI} = 14.5$ to 20 in steps of 0.25 dex, $\log Z/Z_\odot = -2$ to +1 in steps of 0.1 dex, and $\log U = -4$ to 0 in steps of 0.25 dex. The main assumptions made are that gas clouds (1) are in thermal and ionization equilibrium, (2) have a plane-parallel slab geometry with a uniform density, and (3) have relative solar abundances of the elements. We discuss the systematic uncertainties inherent in this method in Section 5.2.

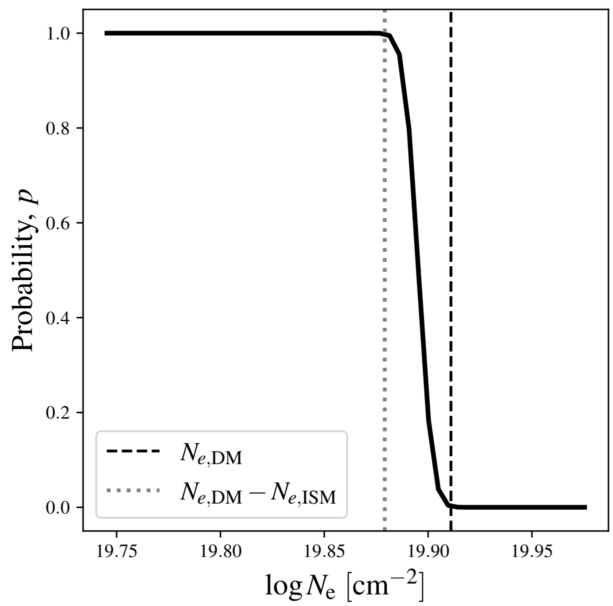

Figure 2.4: The applied likelihood of $N_{\rm e}$ for the M3 sight line.

We apply a Hamiltonian Markov chain (HMC) approach to estimate metallicity by comparing a linearly interpolated grid model to observational constraints, which are ion column densities determined in Sec 3 including $N_{\rm HI}$. We refer to the method described in Fumagalli et al. (2016) which worked successfully for estimating metallicities of the CGM of low-redshift galaxies (Prochaska et al. 2017b).

Furthermore, our strategy to find the best-fit photoionization model and estimate metallicity uses the electron column density from pulsar DMs, $N_{e,\rm DM}$, as a strict upper limit of N_e of a gas cloud. Given that about 4-8 % of the ISM is ionized (de Avillez et al. 2012; Jenkins 2013), we subtract the approximate contribution from the ISM to $N_{e,\rm DM}$ using the NE2001 Galactic free electron density model (Cordes & Lazio 2002). This model provides an electron column density for the given sight line with a distance. Since the model also includes the contribution from the thick disk component that may be a part of the DHI, we exclude the thick disk component from the model and estimate the ISM contribution, $N_{e,\rm ISM}$. The model electron column density, $N_{e,\rm model}$, is directly calculated with a helium correction by the CLOUDY model ($N_{e,\rm model} = N_{\rm HII} + N_{\rm HeII} + 2N_{\rm HeIII}$). The likelihood of N_e

is defined as Q-function with the given $N_{e,\mathrm{DM}}$ and $N_{e,\mathrm{ISM}}$ (Fig. 2.4). Fig 4 shows the probability function of Ne, and that the subtraction of the ISM based on NE2001 extends the transition region in the Q-function. With internally self-consistent ionization corrections and helium corrections, this method effectively constrains the ionized hydrogen column density N_{HII}, which is expected to dominate in mass over H I in the diffuse gas around the Milky Way (Putman et al. 2012).

For the sight lines of M3 and M5, we detect multiple clouds with different velocity offsets. Since $N_{e,\mathrm{DM}}$ is the upper limit of the total electron column density of all the clouds in the same line of sight, we perform a joint HMC fitting for the gas clouds in order to satisfy the constraint on the total electron column density. For example, two IVCs, IVa and IVb, were detected in the M3 line of sight. Thus, the upper limit of the total electron column density $N_{e,\mathrm{tot}}$ is given by $N_{e,\mathrm{DM}} > N_{e,\mathrm{tot}} = N_{e,\mathrm{IVa}} + N_{e,\mathrm{IVb}}$, where $N_{e,\mathrm{IVa}}$ and $N_{e,\mathrm{IVb}}$ are the model electron column density of IVa and IVb, respectively. We validate the self-consistency by ensuring that $N_{e,\mathrm{tot}}$ estimated by the best-fit model is below $N_{e,\mathrm{DM}}$. Finally, in order to determine the ionization parameter, add constraints from ion column density measurements with a wide range of ionization potentials, specifically including a series of ion species of an element (e.g., Si II, Si III, and Si IV, Fe II and Fe III).

For each target, we perform 4 HMC runs of 12,000 steps each, discarding the first 3,000 steps, for the full range of the model grid. The probabilistic programming library `NumPyro` is used for the HMC fitting processes (Bingham et al. 2019; Phan et al. 2019).

We implement HMC fitting against several cloud models to assess the degree to which photoionization can account for the observed data. The considered cloud models are as follows:

- Photoionized low-ion cloud ("Low ion"): We assume the detected intermediate ions such as Si IV, C IV, and N V arise from a transitional-temperature gas phase at $\sim 10^5$ K, and are collisionally ionized. In this case, we apply the photoionization

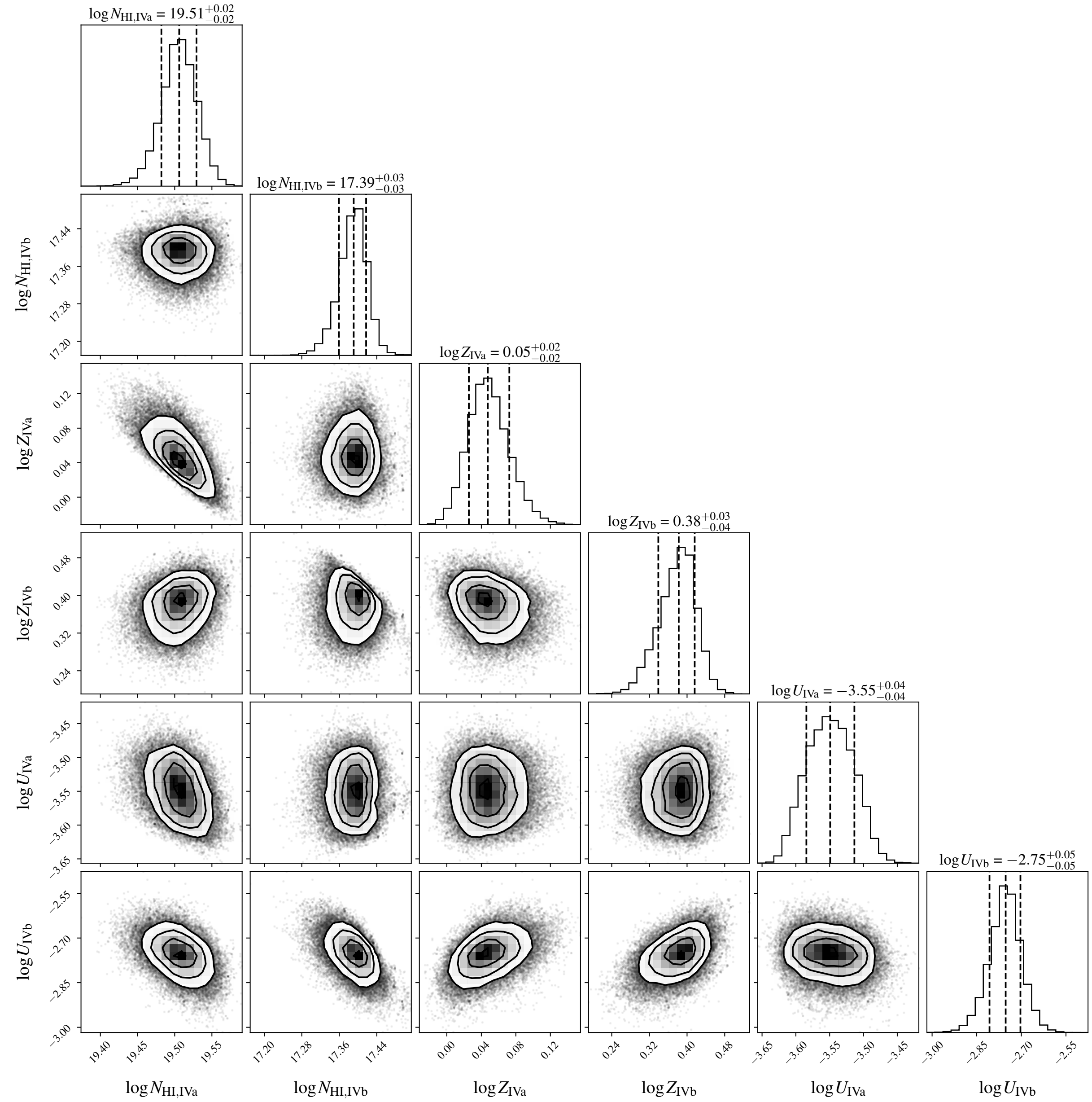

Figure 2.5: The HMC corner plot of M3 fitting to the photoionized low-ion cloud model. The fitted parameters are neutral hydrogen column density $N_{\rm HI}$, metallicity $Z/Z_{\odot}$, and ionization parameter U. The median values of posteriors for each IVC are presented with $\pm 1\sigma$.

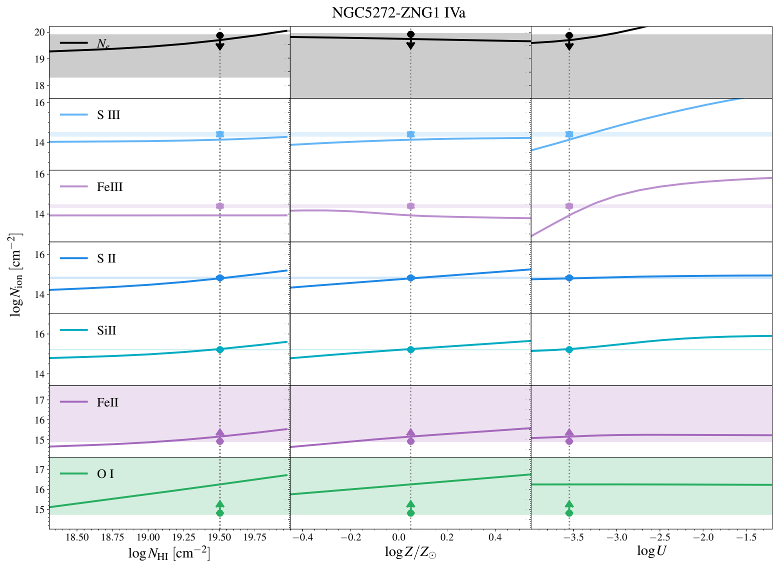

(a) The best-fit photoionization model for the IVa cloud detected along the sight line toward M3

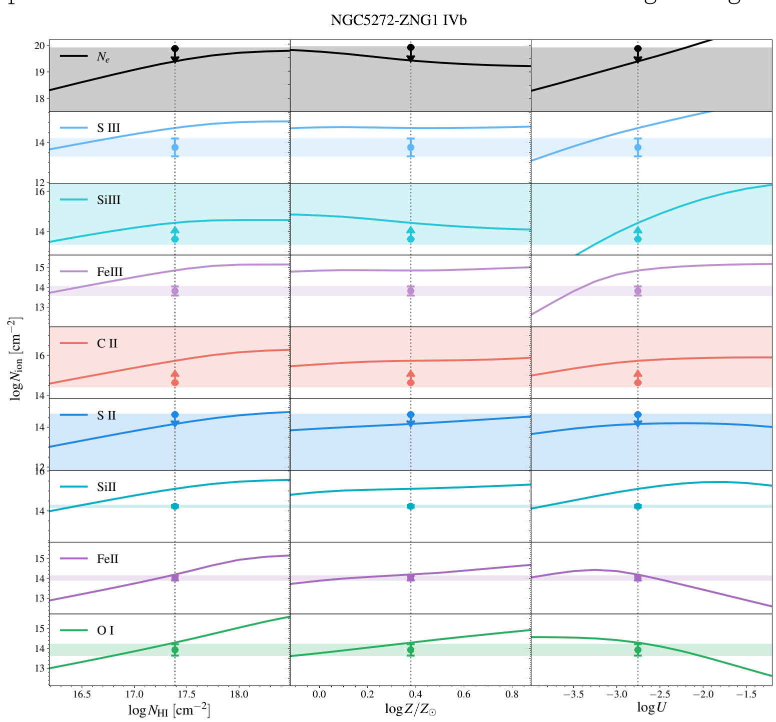

(b) The best-fit photoionization model for the IVb cloud detected along the sight line toward M3

Figure 2.6: The best-fit CLOUDY photoionization models for low ion clouds (solid lines) and ion column density $N_{\rm ion}$ measurements (points and shaded regions, showing the errors) for IVa and IVb detected along the M3 sight line. Each column shows how the CLOUDY model varies by a single parameter, with the other two parameters held at the best fit values from the HMC analysis. The model parameters we vary are H I column density $N_{\rm HI}$ (left), metallicity $Z/Z_\odot$ (middle), and ionization parameter U (right). The best-fit value for each parameter is presented by the gray-dotted vertical line. We mark upper and lower limits with arrows.

modeling to only the low-ion species' column densities.

- Single-phase photoionized cloud ("Single-phase"): This model assumes a single-phase cloud with a uniform density and that the cloud is predominantly photoionized. Since all the ions are in the same photoionized phase in this model, all the observed ion species are used as the constraints on the model.

- Two-phase photoionized cloud ("Two-phase"): We can think of a photoionized cloud in the line of sight with a multi-density structure (Stern et al. 2016). In this case, intermediate and high ions could arise from a low-density part of the gas cloud while low ions would mostly reside in the higher-density (inner) region of the cloud. All of the ion species are employed in the HMC fitting the same as the single-phase model, but there are twice as many free parameters, $\Sigma_\rho(N_{\rm HI,\rho}, Z_\rho, U_\rho)$, where $\rho =$ high, low. We note that we treat the metallicity as a free parameter in both gas phases, motivated by the possibility that they could have different metallicities due to distinct origins and mixing processes.

We present an HMC corner plot for M3 with the photoionized low-ion cloud model as an example in Fig. 2.5. The first row of each column shows the posterior probability distribution function (PDF) of the corresponding parameter with the median and $\pm1\sigma$ value of the PDF. Fig. 2.6 presents the comparison between this low-ion CLOUDY photoionization model and the observational constraints for both IVa (upper panel) and IVb (lower panel) detected along the M3 sight line. We vary each parameter over the full grid range of values in each column, keeping the other two model parameters as the best fit values (solid, colored lines). The vertical gray-dotted line marks the best-fit value for the given parameter on the x-axis, while the circular points with errors given by the shaded regions mark the column density measurements from the absorption-line data.

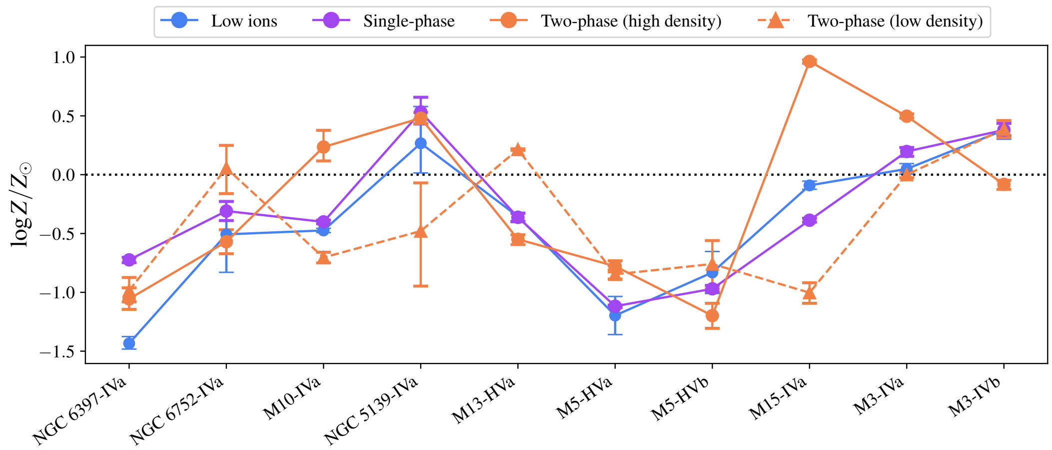

Figure 2.7: The metallicity comparison between photoionized cloud models. The errors are provided by the HMC PDF with 2σ confidence. The blue circle points are for "photoionized low-ion cloud", purple points represent "single-phase photoionized cloud", and orange points show "two-phase photoionized cloud" of which each density phase is noted with point shape and line style, circle points with solid line (high density) and triangle points with dashed line (low density). Solar metallicity $Z_\odot$ is marked with black dotted line.

5 Results

5.1 *Photoionization Model Comparison*

We display the metallicity of the detected DHI clouds in Fig. 2.7 for each of the photoionized cloud models. The metallicities estimated by the "low ion" model are represented by blue circle points connected by the blue solid line. Similarly, the "single-phase" model is illustrated by purple circle points connected by the purple solid line. The metallicity estimations with the "two-phase" model are represented as triangle points, with the high-density phase depicted in blue with a dotted line, and the low-density phase shown in orange with a dashed line. The metallicity estimations derived from the low ion and single-phase models generally exhibit good agreement within a few tenths of a dex. This result is likely attributed to the substantial contribution of low ions in the HMC fitting procedure, as they account for a significant fraction of the observed constraints in the majority of cases. To compare the two-phase model with the other models, the metallicity

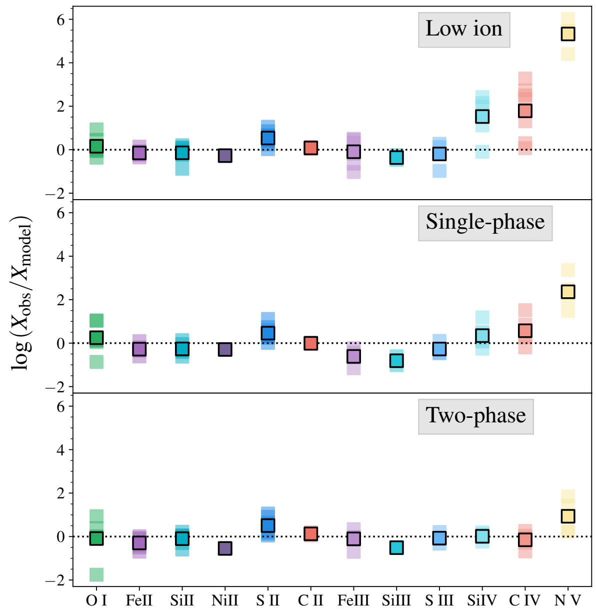

Figure 2.8: The deviation of the ionic column densities derived from the UV absorption observations from the values derived using best-fit Cloudy model. Ions are ordered on the x-axis in order of increasing ionization potential energy. Median deviations for every cloud are shown with a black box outline. While the low-ion model does not use the observational constraints on N_{SiIV}, N_{CIV}, or N_{NV}, both the single-phase and two-phase models do.

provided by the low ion model or single-phase model is compatible with that of the dominant gas phase in the two-phase model except for M15-IVa in which they converge to the middle value between the two phases. It is notable (and challenging to explain physically) that two-phase model for the M15-IVa cloud suggests a low density gas phase with low metallicity, and a high density gas phase with solar metallicity.

In order to examine the goodness of fit for each model, we calculate the deviation of the observed ion column densities, X_{obs}, from the predicted values by the best-fit model, X_{model}. Fig. 2.8 presents the deviation for each ion species in order of ionization potential energy. The scattered points along vertical lines are the deviations for each cloud. We mark the mean deviation for each ion species with the point with a black edge. The low ion model (top) successfully reproduces the observed low ions showing the lowest-level deviations, while the single-phase model (middle) shows larger deviations. Neither satisfactorily matches with the column density constraints from observed intermediate ions (Si IV, C IV, and N V), even these ions are considered in the HMC fitting for the single-phase model. This result implies that low ions and intermediate ions in the DHI gas cannot be explained simultaneously with a single-phase photoionized cloud model. Therefore, it is required to consider a multi-phase gas structure or/and other ionization mechanisms (Fox et al. 2005; Stern et al. 2016; Werk et al. 2019).

The two-phase model (bottom) shows good agreement with observations, notably in successfully reproducing both low and intermediate ions. However, we cannot conclude the two-phase model is the most suitable for DHI clouds since it requires a high-dimensional parameter space compared to the limited number of observational constraints. Furthermore, a thorough exploration of other potential ionization processes is essential, considering that the model still shows offsets from the data in N V with about 0.8 dex. Thus, we discuss in detail the potential ionization mechanisms for intermediate ions in Section 6.1. In the subsequent section, our focus shifts to presenting results based on the low ion model, as it is built on the most physically robust assumptions regarding the ionization processes. Moreover, this model effectively accounts for the observed low ions and in most cases (6/8) reasonably represents the high-density gas phase metallicity of the two-phase model.

5.2 *Physical properties of the photoionized low-ion clouds*

We present the physical properties of the detected clouds derived from HMC fitting to the photoionized low-ion cloud model in Table 2.3. The H I column density $N_{\rm HI}$, metallicity Z, and ionization parameter U are the free parameters of the CLOUDY model, and the best-fit values are given by the median value of the HMC PDFs. The errors are given with 2σ confidence (95%). The H II column density $N_{\rm HII}$ is calculated in the model with the given best-fit parameters. The hydrogen number density $n_{\rm H}$ can be directly converted from the ionization parameter by $n_{\rm H} = n_\gamma / U = \Phi/(cU)$, where Φ is ionizing photon flux.

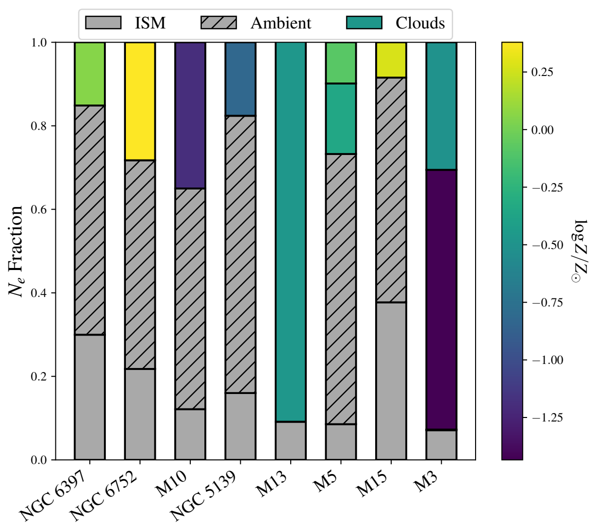

Figure 2.9: Bar chart showing the the electron column density, N_e, fraction for each gas component along the GC sight lines, ordered by increasing distance to the GCs. Each bar is divided into three components: Milky Way ISM (gray), clouds (color), and ambient (gray-hatched). The fraction of the bar representing the IVCs and HVCs is color-coded according to metallicity. The ISM fraction is calculated by the NE2001 model, as discussed in Section 4. The electron column density of each cloud is estimated from the HMC fitting with photoionization modeling. Since we set N_e given by the pulsar DMs as an upper limit, this allows for an additional component of electron column density besides that of the clouds and ISM, possibly ambient hot halo gas. The ambient gas is the dominant source of free electrons along most lines of sight.

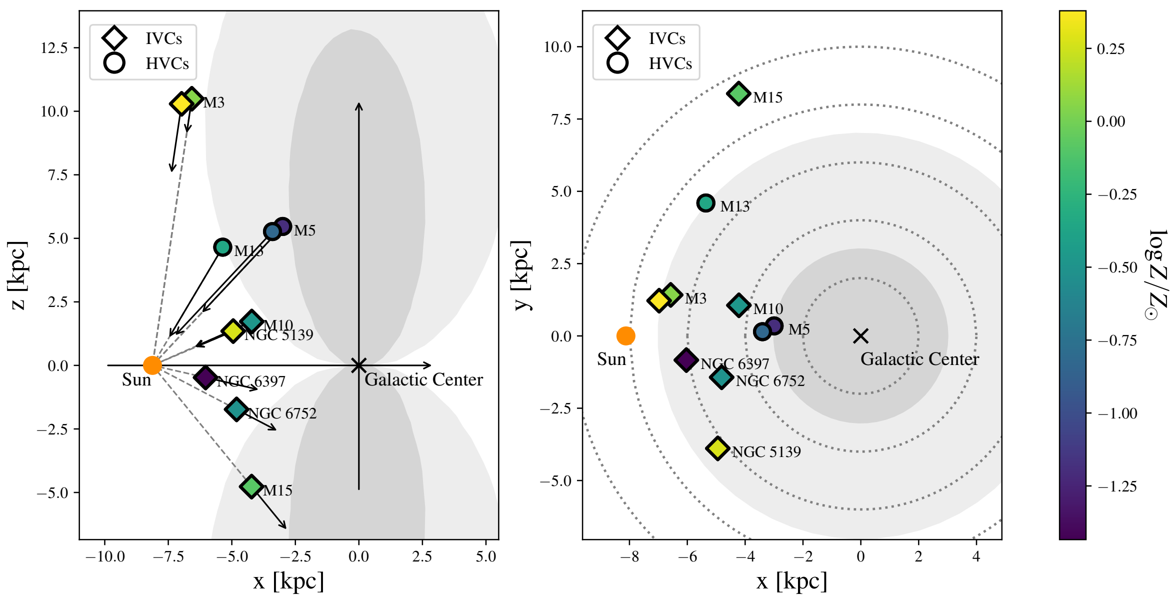

Figure 2.10: The detected IVCs (diamond) and HVCs (circle) in the Galactocentric system where the Sun is at (-8.122, 0, 0) kpc. The left panel shows the distribution in the XZ plane and the right panel is for the XY plane. We show our metallicity estimation in color. The vector sizes are proportional to the line of sight velocity centroids in the LSR. We also present the Fermi (dark gray-shaded) and eROSITA bubbles (gray-shaded) with their approximate size (Predehl et al. 2020).

Table 2.3: The cloud property estimations based on the photoionized low-ion cloud model using the HMC method. The errors are given with 2σ confidence in the PDF.

GC	$z_{\rm max}$ (kpc)	b (°)	Comp	$\overline{v}_{\rm LSR}$ (km s^{-1})	$\log N_{\rm HI}$ (cm^{-2})	$\log N_{\rm HII}$ (cm^{-2})	$\log Z/Z_\odot$	$\log U$	$\log n_{\rm H}$ (cm^{-3})
M3 (NGC 5272)	10.02	78.68	IVa	-37.3	$19.51^{+0.05}_{-0.05}$	19.69	$0.05^{+0.05}_{-0.05}$	$-3.55^{+0.06}_{-0.06}$	$-1.08^{+0.80}_{-0.13}$
			IVb	-71.6	$17.39^{+0.06}_{-0.06}$	19.40	$0.38^{+0.07}_{-0.08}$	$-2.76^{+0.10}_{-0.11}$	$-1.87^{+0.80}_{-0.13}$
M5 (NGC 5904)	5.47	46.79	HVa	-119.2	$16.99^{+0.17}_{-0.17}$	19.18	$-1.20^{+0.16}_{-0.16}$	$-3.24^{+0.11}_{-0.11}$	$-1.09^{+0.50}_{-0.21}$
			HVb	-142.9	$17.00^{+0.20}_{-0.20}$	18.95	$-0.83^{+0.18}_{-0.18}$	$-3.45^{+0.16}_{-0.15}$	$-0.89^{+0.50}_{-0.21}$
M10 (NGC 6254)	1.74	23.09	IVa	-64.4	$18.47^{+0.04}_{-0.04}$	19.66	$-0.47^{+0.02}_{-0.02}$	$-3.33^{+0.01}_{-0.01}$	$-0.81^{+0.31}_{-0.21}$
M13 (NGC 6205)	4.67	40.94	HVa	-106.2	$18.55^{+0.09}_{-0.07}$	19.92	$-0.36^{+0.04}_{-0.04}$	$-3.03^{+0.02}_{-0.03}$	$-1.58^{+0.78}_{-0.07}$
M15 (NGC 7078)	-4.76	-27.31	IVa	60.1	$18.74^{+0.06}_{-0.07}$	19.22	$-0.09^{+0.04}_{-0.03}$	$-3.80^{+0.04}_{-0.04}$	$-0.90^{+0.87}_{-0.17}$
NGC 5139	1.36	15.05	IVa	-43.3	$19.66^{+0.22}_{-0.29}$	19.72	$0.27^{+0.31}_{-0.25}$	$-3.87^{+0.22}_{-0.13}$	$-0.30^{+0.34}_{-0.11}$
NGC 6397	-0.46	-11.94	IVa	51.9	$18.46^{+0.09}_{-0.09}$	19.66	$-1.43^{+0.06}_{-0.05}$	$-3.58^{+0.04}_{-0.04}$	$-0.24^{+0.02}_{-0.19}$
NGC 6752	-1.72	-25.64	IVa	48.0	$18.99^{+0.41}_{-0.40}$	19.46	$-0.51^{+0.29}_{-0.32}$	$-3.72^{+0.24}_{-0.24}$	$-0.44^{+0.33}_{-0.23}$

Note. The model parameters are neutral hydrogen column density $N_{\rm HI}$, metallicity $Z/Z_\odot$, and ionization parameter U. We present ionized hydrogen column density $N_{\rm HII}$ given by the best-fit model.

First, we point out some sources of systematic error inherent to photoionization modeling. The primary uncertainty in our method arises from the modeled fraction of the electron column density contributed by the detected ionized clouds. Despite this uncertainty, when combined with the constraints from ion species with various ionization potentials, our DM method still yields more reliable constraints on the gas ionization parameter than photoionization modeling without the electron column constraints from the pulsar DM. When we perform the modeling without any DM constraints, there are several sight lines that are driven to much higher values of N_H (and correspondingly lower metallicity) than allowed by the DM constraints (M3, M5, M10, and NGC 6397). For example, in the M3 sight line, the pulsar DM provides a maximum electron column of $\log N_e = 19.91$ (Table 2.2). Without this constraint, the best-fit model yields the total electron column density of $\log N_e = 21.66$, and the estimated metallicity for M3-IVb decrease to $\log Z = -1$, and ionization parameter increase to $\log U = -1.5$. The importance of the N_e constraint given by pulsar DMs becomes evident considering that the metallicity estimates of ionized DHI has has been challenging since strong constraints on neutral hydrogen column density are unavailable for most sight lines. Another source of systematic error is the uncertainty in Φ, which is directly proportional to the hydrogen number density. This error can be considerable because we cannot pinpoint the precise 3D location of the clouds, nor do we have precise constraints on the escape of ionizing photons from the Milky Way (Fig. 2.3). Both of these sources of error are always present for any metallicity measurements of ionized gas detected in absorption, but we cannot eliminate them even with the additional DM constraint.

In Figure 2.9, each GC sight line is represented by a bar chart divided into three components: the Milky Way ISM (gray), clouds (colored) that correspond to the detected IVC or HVC ("Component" in Table 2.3), and an additional ambient medium (gray-hatched). Thus, the total electron column density given by pulsar DM, is composed of contributions from the ISM, the clouds, and the ambient medium, expressed as $N_{e,\mathrm{DM}} = N_{e,\mathrm{ISM}} + N_{e,\mathrm{cloud}} + N_{e,\mathrm{ambient}}$. The ISM fraction is calculated using the NE2001 model, while the electron column density of the clouds is derived from our HMC fitting with photoionization modeling. Given that we use N_e values from pulsar DMs as an upper limit of the total electron column density, there is an uncertainty regarding the precise allocation of N_e between the clouds and any remaining sources of free electrons not probed by the UV data (e.g. hot gas at T $\approx 10^6$K). We can see that for six of our eight sight lines, the "ambient" component accounts for approximately 50% of the total electron column. We can additionally use the minimum and maximum Φ values reported by (Fox et al. 2005) to estimate a higher and lower limit of n_H, respectively. Combining these two sources of systematic uncertainty, both of which affect the best-fit ionization parameters and metallicities, we conservatively estimate that they can contribute at most 0.5 dex of error on our reported values. We conclude that our metallicities are likely generally reliable to within a few tenths of a dex. As a result, moving forward, we refer to clouds as sub-solar ($< 0.3\ Z_\odot$), near-solar (0.3 - 1 $Z_\odot$), and super-solar ($> Z_\odot$).

The spatial distribution of the detected IVCs (diamond) and HVCs (circle) in the Milky Way is illustrated in Fig. 2.10. We mark the metallicity with color: sub-solar ($< 0.3\ Z_\odot$; blue), near-solar (0.3 - 1 $Z_\odot$; purple), and super-solar ($> Z_\odot$; pink). Each range of metallicity could reflect the origin of gas clouds. Super-solar metallicity implies the Galactic origin, whereas sub-solar gas might have originated from the intergalactic medium or metal-poor satellite given that the metallicity of hot halo gas is thought to be $\sim 0.3\ Z_\odot$ (Miller & Bregman 2015). The intermediate metallicity range may indicate either the mixing between metal-poor infalling gas and metal-rich Galactic medium (Heitsch & Putman 2009) or the Galactic fountain process that metal-rich gas ejected from the disk is mixed with metal-poor halo gas through condensation and falls back to the disk (Fraternali et al. 2015; Richter 2017). Our targeted sight lines cover a wide region between the Sun and the Galactic center, and the metallicity of the DHI is largely scattered from sub-solar to super-solar. This wide range of metallicity may reflect the complex origin of the gas clouds and/or incomplete mixing processes in this DHI region (Howk et al. 2018). We explore the origin of gas clouds and examine possible scenarios to explain the observed metallicity distribution in Section 6.3.

The hydrogen number density spans from $\log n_{\rm H} = -1.4$ to -0.2 (cm^{-3}), having the mean value of -0.82, and we note that this value is comparable with previous observational and simulational studies of warm ionized gas at the DHI (Gaensler et al. 2008; Melso et al. 2019).

Using the hydrogen number density and the total hydrogen column density, we estimate the length scale of the gas clouds, $D = N_{\rm H}/n_{\rm H}$. The length scales range from 20 - 1000 pc, with a median value on the order of $\sim$ 100 pc (Fig. 2.11). We further note that this size scale is self-consistent with the best photoionization model in that all of the cloud sizes lie below the limit determined by the distance to the targets. The primary uncertainty in cloud size can be largely attributed to their undetermined locations, which dictates the flux of photoionizing radiation to which they are subjected. Nonetheless, the cloud sizes

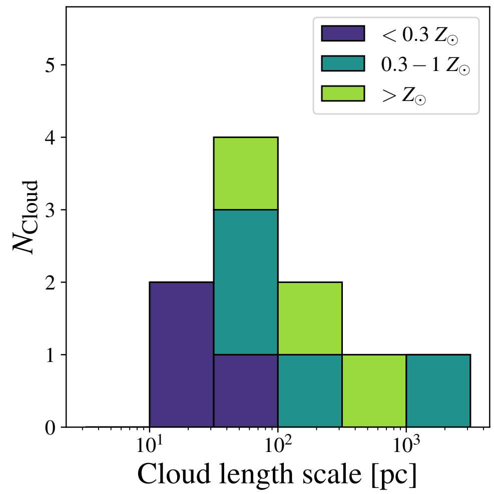

Figure 2.11: A histogram of cloud size. Most of the clouds have a size on the order of ~ 100 pc. The color shows the three metallicity ranges, less than 0.3 $Z_{\odot}$ (blue), 0.3 - 1 $Z_{\odot}$ (purple), and super-solar (pink).

we derive are consistent with the findings of previous observational constraints on DHI gas based on the spatial variation of Ca II column density (Bish et al. 2019). In this study, the cloud sizes are determined exclusively through photoionization modeling, which provides estimates based on ion column density, gas density, and ionization states. On the other hand, in Bish et al. (2019), cloud size estimation was derived from spatial investigations, assessing the extent of DHI gas clouds through observations of low-ion cloud detection and non-detection across the sky, supported by well-constrained distances. They assume from their study that they are tracing clouds with temperatures $T \lesssim 10^4$ K with cloud sizes < 0.5 kpc, similar to our constraints in this independent study using a very different cloud size estimation method.

6 Discussion

6.1 *Photoionization of Intermediate Ions*

We present the physical properties of the identified ionized DHI clouds in Section 5.2, with a specific focus on metallicity based on detailed photoionization modeling of low

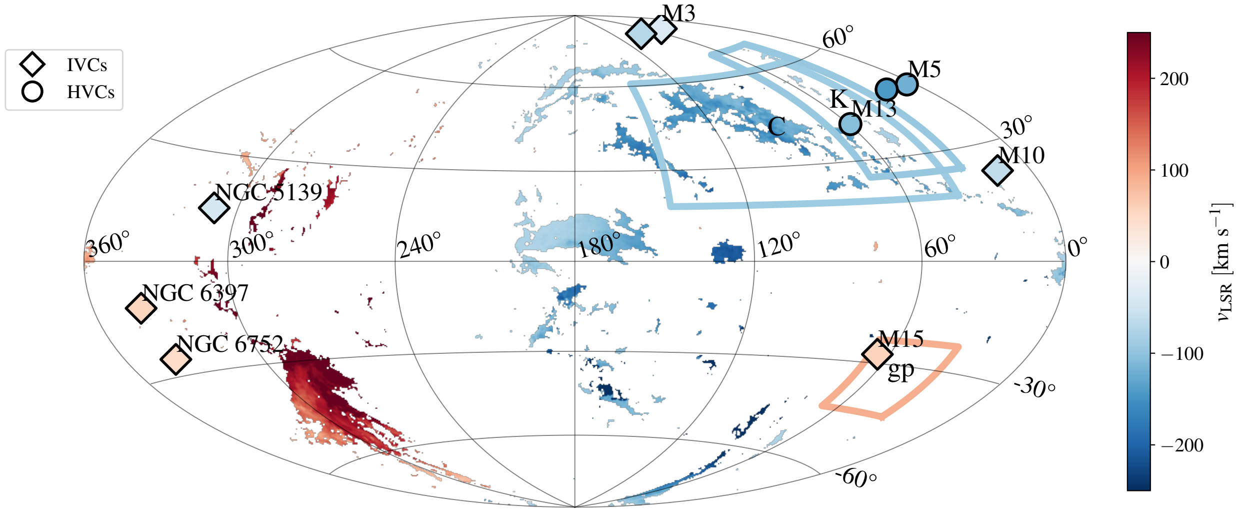

(a) The Galactic distribution of detected IVCs (diamond) and HVCs (circle) with an all-sky H I velocity map from the 21-cm HI4PI survey (Westmeier 2018). Our clouds are potentially part of the known IVC and HVC complexes, Complex C, Complex K, and Complex gp. The three complexes are presented with boxed outlines having a color corresponding to their average LSR velocity.

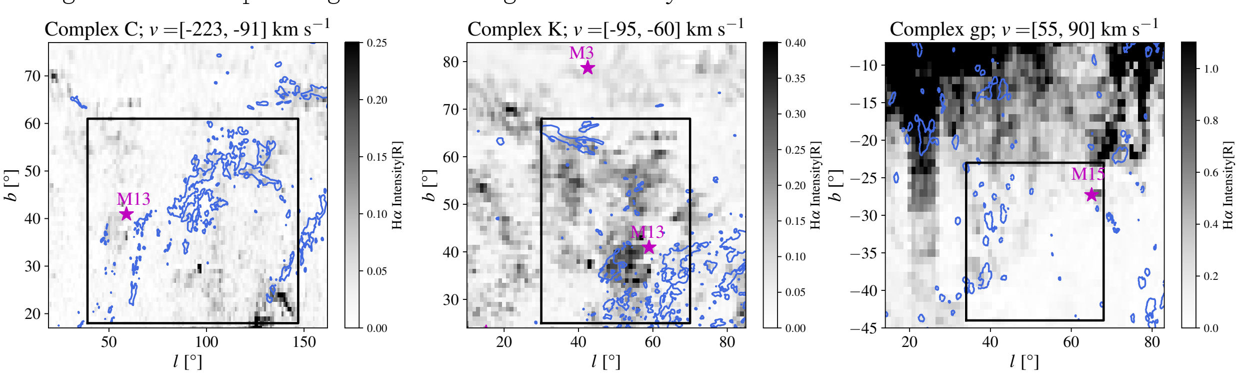

(b) The WHAM map for Complex C (left), Complex K (center), and Complex gp (right). The black boxes correspond to the location of the known complexes. The Hα intensity is integrated for the LSR velocity ranges of each complex, presented on top of the map. The LSR velocity ranges are referred to van Woerden et al. (2004). We note that the WHAM survey covers the velocity range of roughly $(-100, 100)$ km s^{-1}, thus it only covers a small fraction of the velocity range of Complex C. The range of intensities varies for each map, as indicated by the corresponding color bar. The H I map from the HI4PI survey (HI4PI Collaboration et al. 2016) is presented with blue contours with the column density of $N_{\rm HI} = 10^{19.5}, 10^{19}$, and 10^{18} cm^{-2} for Complex C, Complex K, and Complex gp, respectively. We show the location of our three sight lines that are potentially associated with the complexes (magenta stars).

Figure 2.12: (a) The Galactic distribution of detected IVCs and HVCs with all-sky H I map. (b) The WHAM map of the known HVC and IVC complexes that are potentially associated with the detected ionized clouds.

ions. The results exhibit good agreement with observed low ions and maintain consistency with pulsar DMs. The disparity between measured column densities of intermediate ions, Si IV, C IV, and N V, and their predicted values from the low ion and single-phase model indicates that these ions likely reside in distinct gas phases (top and middle of Fig. 2.8). We here explore the potential photoionization of intermediate ions and discuss its validity. We discuss other potential ionization mechanisms for the intermediate ions in Appendix 8.2.

We conduct the “two-phase" photoionized cloud model in Section 4 with the motivation of the hierarchical structure of photoionized clouds along the line of sight, where small dense clouds are embedded in larger low-density clouds (Stern et al. 2016). The results presented in Fig. 2.8 (bottom) demonstrate that the observed column densities of Si IV and C IV can be reproduced by the photoionization model, in particular, a significant fraction of Si IV and C IV resides in the low-density cloud at a temperature of $T \sim 10^4$ K.

The $N_{\rm HII}$ of low-density clouds is approximately 70 % on average compared to that of high-density clouds, indicating that low-density clouds contribute significantly to the total $N_{\rm HII}$ in the two-phase photoionization model. We also find a discrepancy in the metallicity estimation for each density phase (Fig. 2.7). This discrepancy may reflect the nature of the DHI where multi-phase gas flows with various origins are incorporated and affected by feedback, possibly being accreted onto the disk and fueling star formation. The distance to the background halo star serves as a strict upper limit for the cloud length scale. By using this upper limit, we can validate the photoionization model and rule it out if it predicts a larger size for the clouds than the distance to the star. The length scales of the low-density cloud fall within the distance to the star, with a mean value of $\simeq 1$ kpc. Therefore, from the cloud size analysis alone, there remains a possibility that Si IV and C IV originate from photoionized low-density gas clouds. The low-density clouds in the best-fit two-phase model have a median hydrogen number density of $n_{\rm H} = 0.01$ cm^{-3}, while that of the high-density phase gas is $n_{\rm H} = 0.2$ cm^{-3}. Considering a similar gas temperature of the two phases, $T \sim 10^4$ K, there is more than an order of pressure imbalance between the two phases under the hydrostatic equilibrium assumption. Consistent with Stern et al. (2016), we conclude that either there must be a hydrodynamic solution to explain this density structure or the highly ionized species are collisionally ionized as discussed in Appendix 8.2.

6.2 *Association with Known H I IVCs and HVCs*

In Fig. 2.12a, we present the Galactic distribution of the identified IVCs (diamonds) and HVCs (circles) in this work with their LSR velocities, along with an all-sky H I velocity map sourced from the 21 cm HI4PI survey (Westmeier 2018). The ionized clouds identified in this work could potentially be part of or associated with known H I IVCs and HVCs (Wakker 2001). This potential association is based on their spatial alignment in Galactic coordinates and comparable LSR velocities. The potentially associated IVC and HVC complexes are marked with boxed contours colored by their LSR velocities. Their locations in Galactic coordinates are referenced from van Woerden et al. (2004). Fig. 2.12b shows a zoom-in Hα map of the complexes, and the black boxes correspond to the colored boxes in Fig. 2.12a. The Hα map is sourced from the Wisconsin H-Alpha Mapper (WHAM) survey (Haffner et al. 2003), with the Hα intensity integrated over the LSR velocity range of the known complexes (Wakker 2001). We overplot an H I contour (blue) as well with the column density of $N_{\rm HI} = 10^{19.5}$, 10^{19}, and 10^{18} cm^{-2} for Complex C, Complex K, and Complex gp, respectively.

6.2 *M3 - Complex K*

Two IVCs, labeled IVa and IVb, are identified along the line of sight toward M3, exhibiting $v_{\rm LSR}$ of -37 km s^{-1} and -72 km s^{-1}, respectively (see Fig. 4.2 and Table 2.3). Their negative LSR velocities suggest motion indicative of an infalling gas component, particularly notable since M3 is situated near the galactic North Pole ($b = 79°$), where the rotational component of the motion of the Milky Way disk is negligible. It is noteworthy that IVa probably traces IV Arch, a huge H I complex. It is evident from its high H I column density of $N_{\rm HI} \sim 10^{19.5}$ cm^{-2} and its solar metallicity (Table 2.3) that is consistent with previous estimates (Wakker 2001). On the other hand, for IVb, we suggest the possibility of its association with Complex K, an IVC complex characterized by LSR velocities in the range of $-90 < v_{\rm LSR} < -60$ km s^{-1}.

The presence of the IVb cloud was initially reported by de Boer & Savage (1984) based on C II and C IV absorption features observed at $v_{\rm LSR} \sim -70$ km s^{-1} in the UV spectrum of M3 vZ1128 (NGC5272-ZNG1) taken by the International Ultraviolet Explorer (IUE). Wakker (2001) discussed the potential association of this cloud with Complex K; however, they contended that the detection is inconclusive due to the absence of strong absorption lines in the FUSE spectrum of the star and the lack of associated emission in the H I 21 cm map surrounding it. It is crucial to highlight that the high S/N COS spectrum of the same star, combined with joint Voigt profile fitting employed in this study, enables us to differentiate IVb from the strong absorption features of IVa or the Milky Way ISM. The low H I column density estimated at $N_{\rm HI} \sim 10^{17.4}$ cm^{-2} through the HMC fitting is consistent with non-detection in H I 21 cm emission. If IVb is indeed associated with Complex K, it indicates the presence of a more extensive ionized structure surrounding the complex. It is supported by the WHAM map near Complex K (center; Fig. 2.12b). Hα emission around the neutral complex extends to the M3 sight line. Furthermore, the super-solar metallicity of IVb, measured at $Z = 2.4\,Z_{\odot}$, implies a likely origin as a Galactic fountain-driven cloud. We note that this metallicity value is higher than previous measurements for neutral part of Complex K ($Z \sim 1 - 2\,Z_{\odot}$; van Woerden et al. 2004; Wakker 2001).

6.2 M13 - Complex C

We detect an ionized HVC at $v_{\rm LSR} = -106$ km s^{-1} along the line of sight toward M13 that is passing through a lower latitude part of Complex C, a well-known massive, infalling HVC.

Although M13 is closer than the average distance to Complex C ($d \sim 10$ kpc; Thom et al. 2008), we cannot rule out the possibility that the detected HVC is part of a more extended ionized region of the complex (Fox et al. 2004).

Complex C displays low metallicity across the complex in the range of $Z = 0.1 - 0.3\ Z_\odot$ (Fox et al. 2023; Tripp et al. 2003) consistent with our metallicity estimation of $Z = 0.4\ Z_\odot$. It could be possible that the detected HVC lies within the region where metal-poor HVC interacts with a fountain outflow (Tripp et al. 2003). Another potential scenario is that Complex C is formed via the Galactic fountain (Fraternali et al. 2015), and the detected ionized HVC traces a more metal-rich part of the fountain-driven cloud. It is noteworthy that the hydrodynamic simulation of the fountain-driven formation of Complex C by Fraternali et al. (2015) shows a slight metallicity gradient by H I column density, having higher metallicity at lower $N_{\rm HI}$. Our metallicity estimation is in agreement with the predicted value at $N_{\rm HI} \sim 10^{18.5}$ cm^{-2}.

6.2 M15 - Complex gp

The ionized IVC in the sight line toward M15 is part of a known IVC, Complex gp, with LSR velocity of $v_{\rm LSR} \sim 60$ km s^{-1}. The metallicity of Complex gp has been thought to be near-solar based on equivalent widths of several UV absorption lines (Wakker 2001), which is consistent with our measurement of $Z = 0.8\ Z_\odot$.

6.2 M5 - Fermi Bubbles

The HVCs toward M5 have been regarded to be embedded in the Fermi bubbles (Fig. 2.10). The Fermi bubbles are largely extended ($\sim -20° < l < 20°$ and $-50° < b < 50°$) plasma bubbles launched at the Galactic center (Su et al. 2010), and they are clear evidence of Galactic outflows. Several HVCs tracing these outflows were detected within the bubbles, and Ashley et al. (2022) showed that they have a wide range of metallicity from below $0.2\ Z_\odot$ to $3.2\ Z_\odot$. They explained this wide scatter in metallicity by two populations of clouds with different origins. One population of clouds has a Galactic origin, similar to the bubbles themselves, so they are likely to be metal-rich and found at low Galactic latitudes. The other population is pre-existing low-metallicity halo gas shocked and accelerated by the Fermi bubbles as they expand. This latter population can explain the Fermi bubble HVCs with very low metallicity below $\sim 0.2\ Z_{\odot}$, and is more likely to be found at high latitudes.

The HVCs that we detect toward M5 with sub-solar metallicity of $\sim 0.1\ Z_{\odot}$ here were also studied in Ashley et al. (2022); however, they regarded them as super-solar clouds with the metallicity of $3.2\ Z_{\odot}$, referring to a previous study (Zech et al. 2008, hereafter Z08). We describe a few possible reasons that might have given rise to such a large discrepancy. First, our study considers the $N_{\rm HI}$ measured with a *FUSE* spectrum as a lower limit ($N_{\rm HI} > 10^{16.46}$ cm^{-2}) because of the visible saturation. Z08 used $10^{16.50}$ cm^{-2} of $N_{\rm HI}$ as the actual measurements of $N_{\rm HI}$, and consequently, this value is lower than the $N_{\rm HI}$ estimated by our photoionization modeling of $N_{\rm HI} = 10^{17.30}$ cm^{-2}. In addition, while Z08 used the Legendre polynomial to fit the continuum, we normalize the spectra with a stellar-like continuum, characterized by a blackbody and flat in a narrow wavelength range, to avoid an over-correction. Last, and most importantly, they derived a metallicity only using O I and performed an ionization correction using silicon ions at different ionization stages (Si II, Si III, and Si IV). However, the Si III absorption line is saturated as they note, therefore, it could affect the ionization correction and metallicity.

If we assume that the HVCs detected toward M5 have low metallicity as we derive, a potential explanation for their low metallicity would be that they originated from low-metallicity halo gas and were accelerated by the Fermi bubbles as discussed in Ashley et al. (2022).

6.3 *The Nature of the DHI Gas Clouds*

We find that ionized DHI gas at $|z| < 10$ kpc has a wide range of metallicities, $0.04 - 3\ Z_{\odot}$. This spread suggests that ample inflows and outflows from multiple origins are incorporated in the DHI region.

Historically, the categorization of IVCs and HVCs, primarily based on their LSR velocities, has treated them as distinct populations due to their differing metallicities. IVCs, distributed within $d < 1 - 2$ kpc, exhibit near-solar metallicity, suggesting a Galactic fountain origin. On the other hand, HVCs, found at greater distances in the halo (mostly $d < 10 - 15$ kpc), show lower metallicites, indicating an external origin, possibly from satellites or the IGM. Utilizing a significant sample of IVCs and HVCs detected in UV spectra of halo stars, covering a wide fraction of the sky (Lehner et al. 2022), Marasco et al. (2022) challenged this division. They proposed that the kinematics of ionized IVCs and HVCs likely constitute a unified population characterized by a combination of diffuse inflows and collimated outflows, rather than separate populations, thereby supporting the Galactic fountain concept.

At the same time, the region near the Galactic center where the samples studied here mainly cover exhibits dramatic and complex outflow features. As introduced in Section 2.4, the Fermi/eROSITA bubbles are extended to several kpc, and HVCs tracing these outflows have been detected in multiphase (Ashley et al. 2022; Di Teodoro et al. 2020 2018). Furthermore, Mou et al. (2023) argued that the asymmetric structures in morphology and surface brightness shown in the eROSITA bubbles can be reproduced with the CGM wind model, implying dynamic gas flows around the Milky Way.

In this section, we compare our samples with several kinematic models and discuss the nature of DHI gas clouds. We apply the rotation-dominated inflow and outflow models suggested by Marasco et al. (2022) that consider disk-like DHI gas of which velocity vectors are in cylindrical coordinates, $(v_{\rm r}, v_{\phi}, v_{\rm z})$. The kinematic models provide the LSR velocity of a gas cloud at a specific distance from the Sun for any sight lines in the sky. Since we can only determine the upper limit of the distances to the detected DHI clouds from background halo stars, we calculate a range of acceptable LSR velocities for our sample of sight lines as a function of distance. We then compare these predictions with the observed

Table 2.4: Kinematic model parameters.

Parameter ($\mathrm{km\ s^{-1}}$)	Inflow	Outflow	Stagnant
v_r	30^{+15}_{-11}	-22^{+39}_{-35}	0
v_ϕ	233 ± 18	232^{+91}_{-54}	200 ± 30
v_z	-67^{+8}_{-11}	-22^{+39}_{-35}	0

LSR velocities (Fig. 2.13). For reference, we also consider stagnant models where only the rotational motion exists, thus $v_\mathrm{r} = v_\mathrm{z} = 0\ \mathrm{km\ s^{-1}}$. The applied model parameters are presented in Table 2.4. The parameters for the inflow and outflow models are directly adopted from the best-fit parameters provided by Marasco et al. (2022).

In Fig. 2.13, we classify the detected IVCs (diamond) and HVCs (circle) into three groups, inflow (blue), outflow (red), and ambiguous (gray), based on the comparison with the kinematic models. The exceptions are the HVCs in the sight line of M5. Despite their negative LSR velocities, they are likely to trace the outflows as discussed in Section 2.4. Di Teodoro et al. (2018) proposed an outflow model where gas moves away from the Galactic center at a constant velocity. This model adequately explains the negative LSR velocities observed for the M5 HVCs by suggesting that their motion is more horizontal than vertical, implying their relative proximity, approximately 3-4 kpc away. In addition, we note that the HVC toward M13 could potentially be part of Complex C, a well-known infalling HVC.

In order to further examine the nature of these gas clouds, we calculate the inflow and outflow timescale τ for infalling and outflowing gas, respectively. We assume that the vertical velocity component, v_z, is solely responsible for the difference between the measured v_LSR and LSR velocities given by the stagnant model, v_stag. Based on this assumption, we define τ as follows.

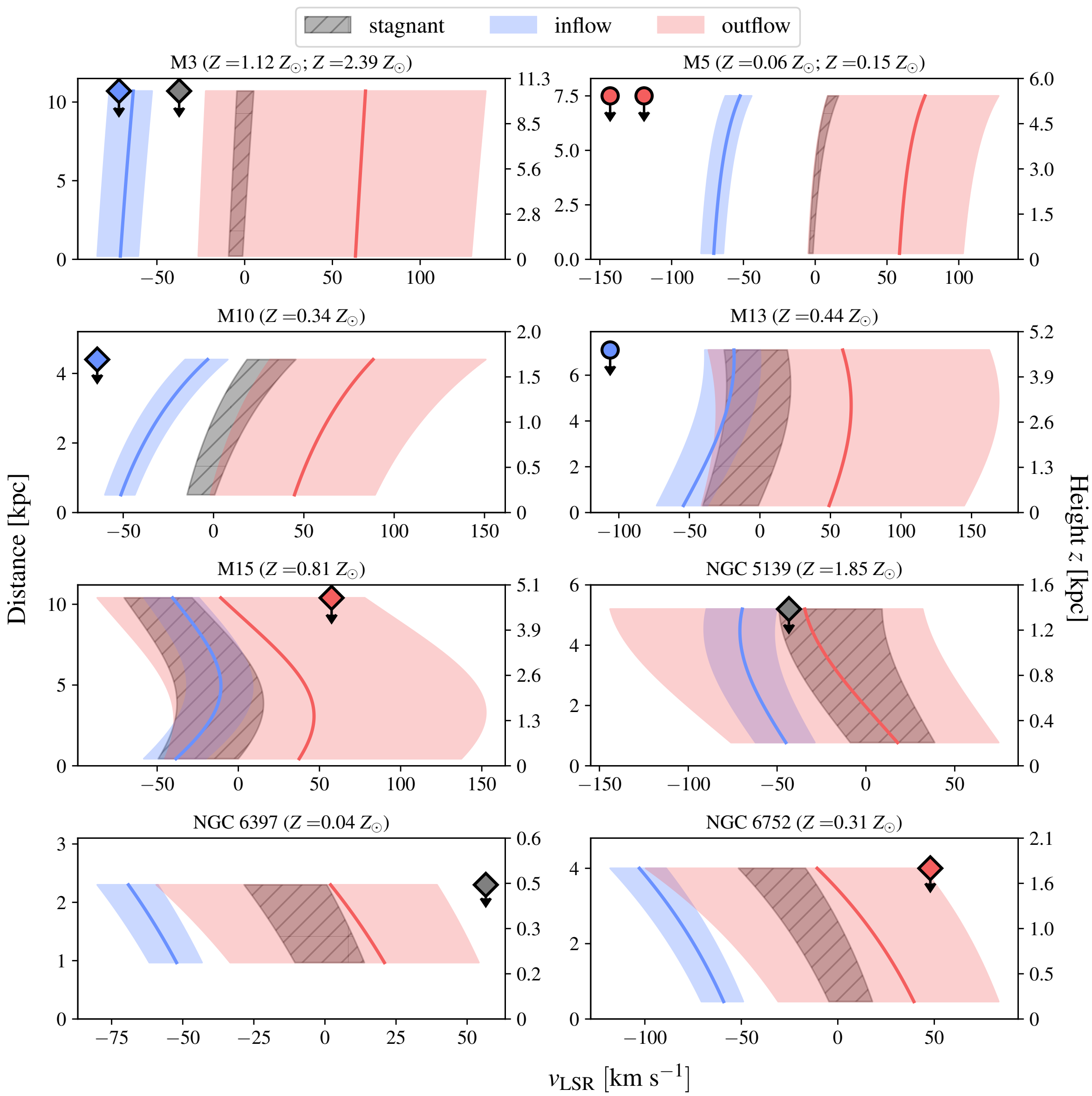

Figure 2.13: Kinematic modeling of LSR velocity for each sight line and observed LSR velocity of the detected IVCs (diamond) and HVCs (circle). LSR velocity is a function of distance from the Sun (left y-axis), and the maximum distance is given by the distance to the targeted halo stars. We present the predictions of inflow (blue-shaded), outflow (red-shaded), and stagnant (hatched) models with the parameters given in Table 2.4. The color of the data points denotes the categorization of inflow (blue), outflow (red), and ambiguous (gray).

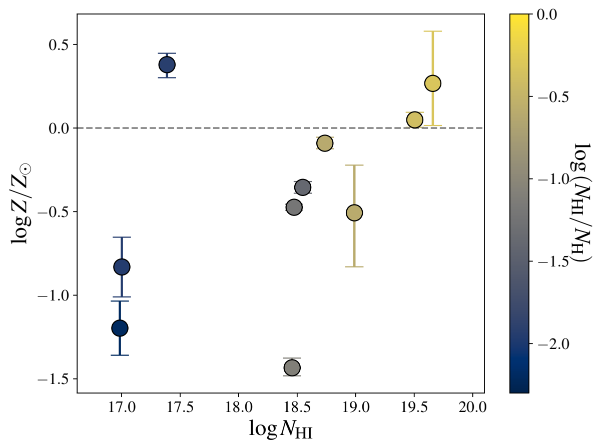

Figure 2.14: The estimated $N_{\rm HI}$ and metallicity of the ionized DHI clouds. The color shows H I fraction over the total hydrogen. We note that most clouds are more than 90 % ionized, and the existence of metal-poor gas clouds in the form of ionized clouds.

$$v_z = \frac{v_{\rm LSR} - v_{\rm stag}}{\sin|b|}, \tag{2.1}$$

$$\tau \equiv \frac{z_{\rm max}}{|v_z|} = \left|\frac{z_{\rm max}\sin|b|}{v_{\rm LSR} - v_{\rm stag}}\right|$$
$$\approx 10\left(\frac{z_{\rm max}}{1\ {\rm kpc}}\right)\left(\frac{\sin|b|}{1}\right)\left(\frac{100\ {\rm km\ s^{-1}}}{v_{\rm LSR} - v_{\rm stag}}\right)\ {\rm Myr}, \tag{2.2}$$

where $z_{\rm max}$ is the maximum Galactic height, and b is Galactic latitude. The characteristic timescales for inflows and outflows mostly range between 6-35 Myrs, except for M3-IVb, which has a timescale of about 150 Myrs. We note that our estimates of inflow/outflow timescales approximate the duration required for gas accretion or the time elapsed since gas clouds were ejected.

For M3-IVb, this longer timescale is attributed to its location at a higher Galactic height of 10 kpc, compared to other targeted GCs predominantly within 5 kpc. We discuss the potential association of M3-IVb with Complex K in Section 2.1. If we adopt the z-height limit of Complex K from Wakker (2001) ($z < 4.5$ kpc), the timescale falls to around 65 Myrs. Given its LSR velocity of $v_{\rm LSR} \simeq -70\ {\rm km\ s^{-1}}$ and high Galactic latitude ($b = 79°$), we infer that the cloud is indeed infalling into the disk, with a high likelihood of accreting onto the star-forming disk within this timescale. Its super-solar metallicity of $Z = 3.2\ Z_{\odot}$ suggests a Galactic origin, indicative of it being a part of a Galactic fountain. In addition, previous studies of gas flows near Complex K for both cool (Bish et al. 2019) and warm phases (Werk et al. 2019) showed that the inflows are confined within a z-height of 3.4 kpc, and their physical and kinematic properties further support a Galactic fountain model.

Unlike M3-IVb, we also observe metal-poor infalling clouds in the sight lines of M10 and M13 (Fig 2.13). Given their low Galactic height of $z < 10$ kpc, these clouds are likely to survive and accrete onto the disk (Tan et al. 2023). Both metal-poor and metal-rich outflows are also observed. We propose that metal-rich clouds trace outflowing material, while metal-poor clouds trace halo gas that has been shocked and accelerated by outflows, as discussed in Section 2.4. This observation highlights the complexity of gas flows on the small scale of the DHI. The presence of both metal-rich and metal-poor components in inflows and outflows indicates that metallicity alone cannot reliably trace the nature or origin of gas flows.

Notably, we detect low-metallicity ionized clouds with $N_{\rm HI} < 10^{19}\ {\rm cm^{-2}}$, which is challenging to detect and determine metallicity given the H I 21 cm emission detection limit for many surveys (Fig. 2.14). The Galactic chemical evolution model requires the continuous accretion of low-metallicity gas to explain the observed stellar abundance and scaling laws (Chiappini et al. 2001; Sánchez Almeida et al. 2014), and lines of hydrodynamic simulation have predicted that a substantial portion of gas accretion occurring in the form of ionized matter (e.g., Heitsch & Putman 2009; Joung et al. 2012; Kim & Ostriker 2018). The detection of low-metallicity ionized clouds evidently shows gas accretion in the form of ionized material and implies its role in fueling Galactic star formation.

7 Summary

In this work, we estimate the metallicity of the diffuse warm ionized gas at the DHI with a strong constraint on ionized hydrogen column density given by the radio pulsar DM. We analyze archival COS, STIS, and *FUSE* spectra of 10 halo GCs and detect ionized IVCs and HVCs along the 8 sight lines within the Galactic height of $z \lesssim 10$ kpc.

All the absorption components within $|v_{\rm LSR}| < 200\,{\rm km\,s^{-1}}$ are identified, therefore, the ionized clouds with $|v_{\rm LSR}| > 20$ km s^{-1} are deblended from the Milky Way ISM absorption and stellar absorption. We measure their ion column densities separately by Voigt profile fitting to estimate the metallicity of an individual gas cloud.

We perform photoionization modeling using CLOUDY under three distinct scenarios: (1) where low ions exist in a photoionized gas phase while intermediate and high ions are collisionally ionized (referred to as the “low ion” model), (2) where all ions are uniformly photoionized within a single gas phase (“single-phase”), and (3) where all ions are photoionized, but the clouds are structured into two distinct density phases (“two-phase”). We find that low ions and intermediate and high ions cannot be in a single phase of photoionized gas, clearly indicating the multi-phase structure of ionized clouds.

We present self-consistent and statistically preferred metallicity estimates of ionized IVCs and HVCs using the HMC method based on the low ion model. The DHI gas clouds show a large scatter in metallicity, spanning the range of $0.04 - 3\ Z_\odot$. These inhomogeneities may indicate a widespread Galactic Fountain in which outflowing and inflowing gas are neither well-mixed nor of a single origin.

Some of our samples may trace the extended ionized envelope of known neutral HVC and IVC complexes. The IVC detected in the sight line of M3 may be part of the ionized envelope of Complex K, and its super-solar metallicity of $3.2\ Z_\odot$ and the inflow signature suggest a fountain-driven flow. The M13 HVC might be associated with Complex C, a well-known infalling low-metallicity HVC, and our metallicity estimate based on low ions is

$Z = 0.4\,Z_{\odot}$. This value is slightly higher than previous measurements of the neutral parts, possibly indicating mixing with metal-rich Galactic material. The IVC in the sight line of M10 could be an ionized counterpart of Complex gp, and its near-solar metallicity of $Z = 0.8\,Z_{\odot}$ is comparable to the metallicity estimate of the neutral part. We also report low-metallicity HVCs toward M5 that are potentially associated with the Fermi bubbles. Interestingly, these findings diverge from previous studies that suggested a super-solar metallicity of $3.2\,Z_{\odot}$ for these HVCs (Ashley et al. 2022; Zech et al. 2008). Although they trace outflows, their low metallicity of $\sim 0.1\,Z_{\odot}$ suggests that they are likely preexisting halo gas accelerated by the expansion of the bubbles rather than directly tracing outflow material.

In the unambiguous cases for which we are able to identify inflows and outflows, the characteristic timescales on which material cycles into and out of the disk mostly range between $6 - 35$ Myrs. We detect a super-solar infalling cloud, and a low-metallity outflowing cloud, which poses a challenge for Galactic fountain and feedback models.

8 Appendix

8.1 Ion Column Density Measurements and the Voigt Profile Fitting Parameters

We present all the electron column density N_e measured by pulsar DM and ion column density measurements N_{ion} for every GC sight line studied in this paper. The discussion about an upper limit and lower limit can be found in Section 3. For the GCs with multiple available pulsar DMs, the mean value of the DMs is adopted and the uncertainty is given by 5 times of the standard error of the mean.

Table 2.5: Voigt profile measurements and ion column densities of the detected ionized gas clouds

GC	Component	Ion	log N (cm^{-2})	b ($km\ s^{-1}$)	v_{LSR} ($km\ s^{-1}$)
M3 (NGC 5272)	Total	e^-	$<$ a 19.91 $\pm$ 0.01	....	....
	IVa	H I	$>$ 16.96 $\pm$ 0.16	....	....
		O I	$>$ 14.81 $\pm$ 0.07	21.8 $\pm$ 5.3	-38.3 $\pm$ 2.7
		Fe II	14.92 $\pm$ 0.02	27.9 $\pm$ 0.8	-37.5 $\pm$ 0.7
		S II	14.83 $\pm$ 0.04	12.5 $\pm$ 1.9	-38.0 $\pm$ 1.7
		Fe III	14.40 $\pm$ 0.08	19.8 $\pm$ 2.9	-45.8 $\pm$ 1.7
		S III	14.41 $\pm$ 0.10	21.9 $\pm$ 3.5	-23.7 $\pm$ 4.1
		Si IV	13.63 $\pm$ 0.11	16.9 $\pm$ 3.1	-38.2 $\pm$ 1.8
		C IV	14.21 $\pm$ 0.06	19.6 $\pm$ 3.5	-39.6 $\pm$ 1.7
		N V	13.15 $\pm$ 0.05	19.1 $\pm$ 4.3	-33.2 $\pm$ 2.6
	IVb	H I	$>$ 16.92 $\pm$ 0.16	....	....
		O I	13.92 $\pm$ 0.29	8.6 $\pm$ 5.7	-73.1 $\pm$ 4.1
		Fe II	14.02 $\pm$ 0.12	4.0 $\pm$ 0.9	-73.3 $\pm$ 1.0
		Si II	14.23 $\pm$ 0.06	26.2 $\pm$ 2.7	-76.7 $\pm$ 3.2
		S II	$<$ 14.63 $\pm$ 0.03	....	....
		C II	$>$ 14.64 $\pm$ 0.22	27.0 $\pm$ 3.4	-61.9 $\pm$ 7.5
		Fe III	13.82 $\pm$ 0.23	21.9 $\pm$ 7.9	-81.4 $\pm$ 8.9
		Si III	$>$ 13.61 $\pm$ 0.28	25.2 $\pm$ 5.3	-68.4 $\pm$ 11.0
		Si IV	13.17 $\pm$ 0.30	28.0 $\pm$ 13.0	-74.6 $\pm$ 15.6
		C IV	13.64 $\pm$ 0.14	17.8 $\pm$ 4.9	-79.7 $\pm$ 4.9
		N V	$<$ 12.55 $\pm$ 0.19	....	....
M5 (NGC 5904)	Total	e^-	$<$ b 19.96 $\pm$ 0.02	....	....
	HVa	H I	$>$ 16.27 $\pm$ 0.09	....	....
		O I	13.32 $\pm$ 0.04	....	-125.8
		Fe II	$<$ 13.25 $\pm$ 0.16	....	....

Continued on next page

Table 2.5 – continued

GC	Component	Ion	log N (cm^{-2})	b ($km\ s^{-1}$)	v_{LSR} ($km\ s^{-1}$)
		Si II	12.88 ± 0.03	10.7 ± 0.9	-124.2 ± 0.8
		S II	< 13.26 ± 0.54	....	....
		C II	14.11 ± 0.03	16.2 ± 0.9	-125.5 ± 1.1
		Si III	13.14 ± 0.19	15.1 ± 4.6	-115.2 ± 2.5
		Si IV	12.55 ± 0.03	11.9 ± 1.4	-111.4 ± 0.9
		C IV	13.55 ± 0.20	12.0 ± 3.0	-113.4 ± 1.7
	HVb	H I	> 16.00 ± 0.12	....	....
		O I	13.31 ± 0.04	....	-140.8
		Fe II	< 13.23 ± 0.18	....	....
		Si II	13.25 ± 0.02	5.7 ± 0.3	-144.6 ± 0.3
		S II	< 13.25 ± 0.34	....	....
		C II	14.28 ± 0.49	4.4 ± 1.5	-143.6 ± 0.5
		Si III	12.96 ± 0.09	6.9 ± 1.1	-140.5 ± 1.0
		Si IV	12.64 ± 0.02	6.9 ± 0.7	-144.4 ± 0.4
		C IV	13.34 ± 0.05	8.7 ± 1.5	-143.4 ± 1.0
M10 (NGC 6254)	Total	e^-	< c 20.13 ± 0.02	....	....
	IVa	O I	14.68 ± 0.02	20.4 ± 1.2	-62.9 ± 1.0
		Fe II	14.28 ± 0.01	25.0 ± 1.2	-64.8 ± 0.7
		Si II	14.30 ± 0.01	16.2 ± 0.4	-63.2 ± 0.5
		S II	14.38 ± 0.03	22.0 ± 2.7	-62.4 ± 1.5
		Si III	> 13.69 ± 0.07	....	....
		Si IV	13.35 ± 0.02	28.1 ± 2.0	-65.2 ± 1.3
		C IV	13.70 ± 0.03	26.7 ± 1.8	-67.8 ± 1.5
		N V	< 12.77 ± 0.36	....	....
M13 (NGC 6205)	Total	e^-	< d 19.97 ± 0.02	....	....
	HVa	O I	> 14.64 ± 0.02	16.3 ± 0.9	-95.0 ± 0.5
		Fe II	14.16 ± 0.01	21.4 ± 1.5	-111.4 ± 0.7

Continued on next page

Table 2.5 – continued

GC	Component	Ion	log N (cm^{-2})	b ($km\ s^{-1}$)	v_{LSR} ($km\ s^{-1}$)
		Si II	14.32 ± 0.01	22.9 ± 0.3	-98.4 ± 0.4
		S II	14.44 ± 0.01	13.3 ± 1.0	-107.4 ± 0.6
		C II	> 14.05 ± 0.07	29.2 ± 3.4	-114.3 ± 9.2
		Fe III	14.17 ± 0.07	27.9 ± 3.9	-96.1 ± 3.7
		S III	14.65 ± 0.02	23.6 ± 1.1	-111.2 ± 0.9
		C IV	13.60 ± 0.42	18.5 ± 7.0	-110.4 ± 12.0
M15 (NGC 7078)	Total	e^-	< e 20.32 ± 0.01	....	....
	IVa	H I	> 16.86 ± 0.06	....	....
		O I	> 14.86 ± 0.09	12.4 ± 1.8	62.0 ± 1.6
		Fe II	14.19 ± 0.02	17.9 ± 1.3	58.0 ± 0.8
		Si II	14.39 ± 0.02	16.1 ± 0.4	57.5 ± 0.5
		S II	14.83 ± 0.02	10.7 ± 0.6	63.0 ± 0.4
		Fe III	14.02 ± 0.04	....	....
		Si IV	13.14 ± 0.27	31.3 ± 11.9	42.6 ± 16.0
		C IV	13.27 ± 0.12	13.6 ± 4.6	61.8 ± 3.8
NGC 6397	Total	e^-	< f 20.35 ± 0.01	....	....
	IVa	H I	> 16.66 ± 0.10	....	....
		O I	13.81 ± 0.02	7.7 ± 0.6	43.6 ± 0.4
		Fe II	< 12.84 ± 0.63	....	....
		S II	< 13.98 ± 0.05	....	....
		C II	> 14.12 ± 0.06	16.5 ± 1.3	59.5 ± 1.8
		Fe III	13.70 ± 0.13	23.0 ± 8.8	46.4 ± 5.3
		Si IV	12.53 ± 0.05	14.4 ± 1.9	59.8 ± 1.3
		C IV	13.29 ± 0.12	16.0 ± 3.5	57.6 ± 3.7
		N V	13.24 ± 0.38	27.3 ± 15.6	65.5 ± 15.7
NGC 5139	Total	e^-	< g 20.48 ± 0.03	....	....
	IVa	N I	> 15.07 ± 0.21	14.6 ± 2.1	-39.6 ± 4.7

Continued on next page

Table 2.5 – continued

GC	Component	Ion	log N (cm^{-2})	b ($km\ s^{-1}$)	v_{LSR} ($km\ s^{-1}$)
		O I	$> 14.77 \pm 0.27$	15.0 ± 4.8	-48.2 ± 5.9
		Fe II	15.20 ± 0.03	8.6 ± 0.4	-50.7 ± 0.5
		Ni II	13.91 ± 0.07	14.2 ± 1.8	-43.8 ± 1.8
		S II	15.53 ± 0.08	20.8 ± 1.8	-34.5 ± 3.1
		Si IV	13.57 ± 0.18	12.0 ± 3.4	-44.3 ± 1.8
		C IV	13.99 ± 0.19	18.5 ± 4.8	-32.4 ± 2.3
		N V	13.39 ± 0.15	25.0 ± 8.5	-45.6 ± 7.2
NGC 6752	Total	e^-	$<$ h 20.01 ± 0.01	....	....
	IVa	O I	15.15 ± 0.04	14.2 ± 1.4	38.8 ± 1.2
		Fe II	14.15 ± 0.04	14.5 ± 1.8	45.7 ± 1.7
		Si II	14.61 ± 0.37	19.6 ± 7.8	39.6 ± 11.1
		S II	14.59 ± 0.08	18.4 ± 3.1	41.5 ± 3.3
		Fe III	13.73 ± 0.09	12.7 ± 3.4	55.2 ± 2.2
		Si IV	13.29 ± 0.04	28.0 ± 2.8	47.7 ± 2.3
		C IV	13.86 ± 0.05	20.1 ± 2.5	45.3 ± 2.4
		N V	13.37 ± 0.32	33.6 ± 17.8	45.7 ± 20.4

References. (a) Hessels et al. (2007); (b) Freire et al. (2008); Pallanca et al. (2014); (c) Pan et al. (2021); (d) Wang et al. (2020); (e) Anderson (1993); (f) D'Amico et al. (2001); Zhang et al. (2022); (g) Dai et al. (2020); (h) D'Amico et al. (2002)

Note. The electron column density given by pulsar DM is the total column density for the GC sight line. log N is ion column density, and b is the Doppler parameter of the absorption line. The errors correspond to 1σ given by Voigt profile fitting procedure using `veeper`.

8.2 Collisional ionization

While the two-phase photoionization model shows a good agreement with the observation for Si IV and C IV (Fig. 2.8), the observed N V column densities still show about 1 dex excess compared to the model, supporting the idea that photoionization alone is insufficient to produce ions with such a high ionization state (Fox et al. 2004). Consequently, the intermediate ions potentially reside in a hotter gas phase ($T \gtrsim 10^5\ K$) where collisional ionization becomes dominant (Fox et al. 2005; Savage & Wakker 2009; Werk et al. 2019).

At the DHI, a gas phase at transitional temperature of 10^5 K can arise from various collisional ionization mechanisms and processes, encompassing collisional ionization equilibrium (CIE; Sutherland & Dopita 1993), radiative cooling of hot gas (Edgar & Chevalier 1986), turbulent mixing layers (Fielding et al. 2020; Slavin et al. 1993; Tan & Oh 2021), conduction fronts (Borkowski et al. 1990), and shock ionization (Dopita & Sutherland 1996). We evaluate multiple potential mechanisms against the data, specifically examining their compatibility with the photoionization model presented in Section 5.2 to ensure robust consistency. While a detailed analysis of absorption line profiles and column density ratios could serve as diagnostics for ionization mechanisms and gas properties (Fox et al. 2004; Gnat & Sternberg 2007), such an examination is beyond the scope of this work, which primarily centers on deriving the metallicity of ionized gas. Additionally, our observed set of ions is limited for such analysis, predominantly composed of low ions and occasionally missing higher ions than C IV.

We compare the observed intermediate ions with CIE, non-equilibrium radiative cooling, and turbulent mixing layers models among various mechanisms. Other mechanisms are excluded because of their complexity and dependence on uncertain parameters. For instance, thermal conduction is intricately linked to magnetic field (Borkowski et al. 1990). Shock ionization typically results from fast shocks (Dopita & Sutherland 1996), however, the detected clouds are mostly IVCs that exhibit a relatively low velocity ($|v_{\rm LSR}| < 90\,{\rm km\,s^{-1}}$, though this is a projected velocity), making them less likely to be relevant.

CIE serves as a basic depiction of collisionally ionized gas, assuming a balance between ionization and recombination at a fixed temperature. When the timescale for radiative cooling is rapid compared to recombination, gas deviates from CIE, necessitating consideration of non-equilibrium radiative cooling. We adopt the CIE and non-equilibrium cooling models developed by Gnat & Sternberg (2007) for a temperature range of $10^{4.5} \leq T \leq 10^{5.5}$ K. Isobaric (constant pressure) and isochoric (constant density) cooling con-

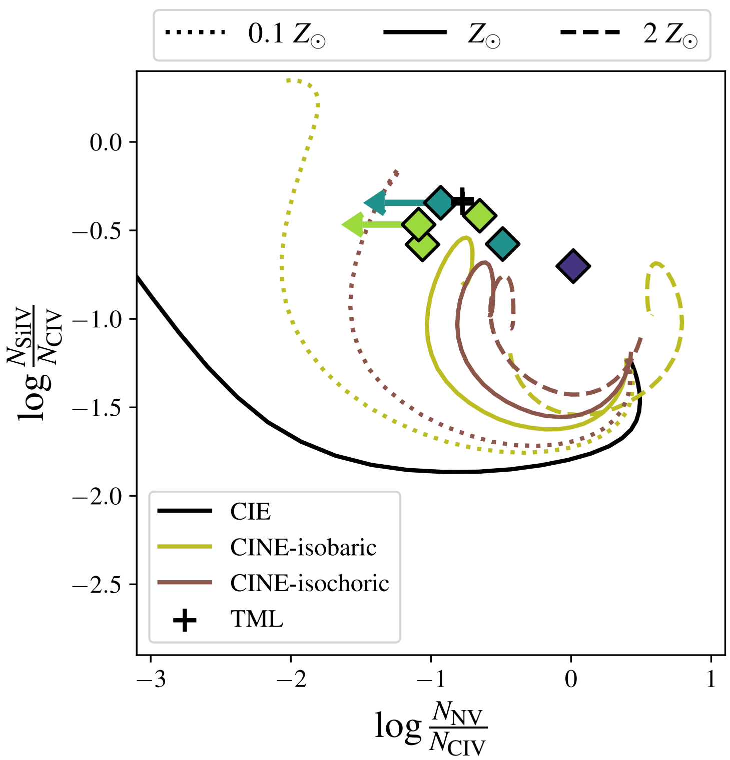

Figure 2.15: Column density ratios of N V/C IV vs. Si IV/C IV, comparing the observation and predicted values by various ionization mechanisms, CIE (black), isobaric (olive) and isochoric (brown) cooling, and turbulent mixing layers (plus mark). Non-equilibrium cooling depends on metallicity as the model of 0.1 (dotted), 1 (solid), and 2 $Z_\odot$ (dashed) shows.

ditions are explored for gas with metallicity of $Z/Z_{\odot} = 0.1, 1$, and 2, reflecting our wide-ranging metallicity measurements. Turbulent mixing layers are relevant to DHI gas, given their prevalence in multiphase gas and ample multiphase gas flows at the DHI. These layers can be conceptualized in scenarios involving neutral clouds either ejected from the disk via feedback (Fraternali 2017) or accreted from outside of the Milky Way (Heitsch & Putman 2009) and traveling through a hot halo medium. We apply the analytic model of turbulent radiative mixing layers developed by Chen et al. (2023) with $p_{\rm hot}/k_{\rm B} = 10^3\,{\rm K\,cm^{-3}}$, considering a hot medium with a temperature of $T = 10^6$ K and hydrogen number density of $n_{\rm H} = 10^{-3}$ cm^{-3}, which correspond to those of hot halo gas. We note that the prediction from turbulent radiative mixing layers shows almost constant column density ratios for $p_{\rm hot}/k_{\rm B} = 10^{3-5}$ K cm^{-3}.

We utilize column density ratios, specifically $N_{\rm SiIV}/N_{\rm CIV}$ and $N_{\rm NV}/N_{\rm CIV}$, as diagnostic tools for ionization mechanisms, displayed in Fig. 2.15. The observational constraints include instances where N V absorption was detected or where no interface from other absorption features hindered the estimation of the upper limit of N V, denoted by diamond points. The color represents metallicity derived from low ions (Section 5.2) categorized into sub-solar ($< 0.3\,Z_{\odot}$; blue), near-solar ($0.3{-}1\,Z_{\odot}$; purple), and super-solar ($> Z_{\odot}$; pink). The observed $\log N_{\rm SiIV}/N_{\rm CIV}$ spans a range between -1 and -0.35, significantly surpassing the predicted ratio by CIE (black solid line). As a result, CIE is ruled out as an explanation for the highly ionized gas portion of the detected DHI clouds. The observed column density ratios fall within the isobaric (olive) and isochoric (brown) cooling regimes, while the models show considerable dependence on metallicity. We note that the metallicity estimate based on low ions may differ from the transitional temperature gas, especially in situations where metal-poor or metal-rich cool gas travels through an ambient hot halo medium. This difference arises because low ions primarily trace the colder core of the cloud, whereas the transitional gas could represent a more diffuse wake produced by the cooling of halo gas. The turbulent radiative mixing layers model with solar abundance

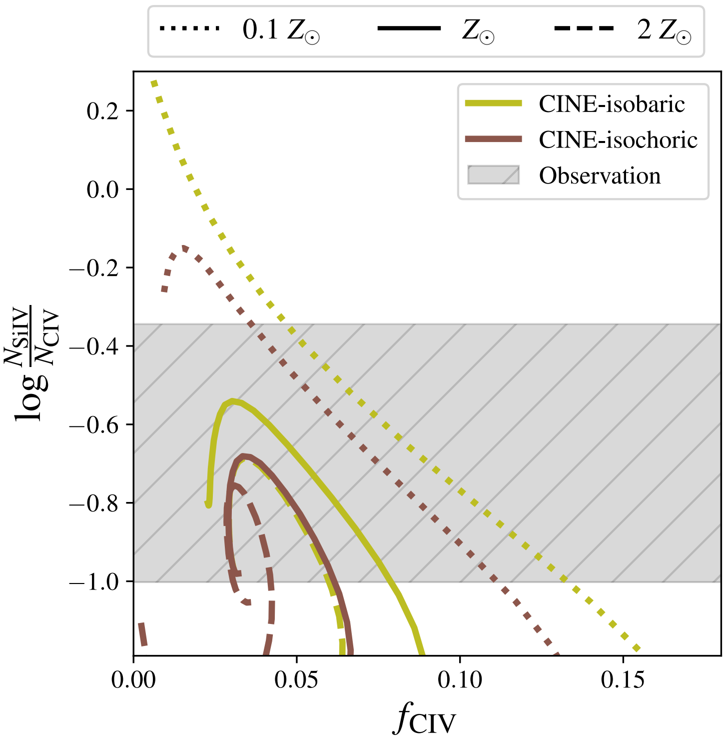

Figure 2.16: C IV fraction to total carbon and column density ratios of Si IV and C IV predicted by isobaric (olive) and isochoric (brown) non-equilibrium radiative cooling at 0.1, 1, and 2 $Z_\odot$ metallicity. The observed column density ratios of Si IV and C IV are within the gray-shaded range.

(plus mark) also matches with the observed ion ratios.

To corroborate the consistency of collisional ionization models with the photoionization model, we calculate the fraction of gas in the transitional temperature phase to the photoionized low-ion gas ($T = 10^{3.5-4}$ K). For the photoionized gas, we use the ionized hydrogen column density provided in Table 2.3. As shown in Fig. 2.16, we employ C IV fraction to the total carbon, $f_{\rm CIV}$, to estimate the ionized hydrogen column density of the transitional phase gas, $N_{\rm HII,trans}$. The C IV fraction, determined by the models using the column density ratio of Si IV and C IV, varies with metallicity. Assuming the cooling of hot halo gas at sub-solar metallicity ($Z \sim 0.1\ Z_\odot$; Ponti et al. 2023), we find $N_{\rm HII,trans}$ to be $25 - 150$ % of the photoionized gas, and these values remain consistent within the upper limit of the total electron column density provided by pulsar DMs along the sight line.

On the other hand, for solar-metallicity hot gas expected in feedback-driven outflows, the model fails to find a solution for gas clouds with a high Si IV/C IV ratio (Fig. 2.16), and it yields much lower $N_{\mathrm{HII,trans}}$ ranging from $4 - 30$ % of the photoionized gas.

The observed intermediate ions, Si IV, C IV, and N V, are more likely to reside in a gas phase at transitional temperature of 10^5 K, rather than in photoionized gas ($T \sim 10^4$ K). This temperature regime can be attributed to radiative cooling of hot gas and turbulent mixing layers, along with the observed ion ratios shown in Fig. 2.15. Additionally, our photoionization model for low ions is compatible with collisional ionization for intermediate ions under moderate condition, maintaining consistency with electron column densities derived from pulsar DMs.

Chapter 3

Resolving Gas Recycling Flow in the Milky Way Halo

The work in this chapter was produced in collaboration with Jessica K. Werk and Kirill Tchernyshyov and will be submitted for publication in the Astrophysical Journal.

Summary

The metallicity of gas accreting onto the Milky Way disk is a fundamental input to Galactic chemical evolution. In the Milky Way and nearby spiral galaxies, a significant fraction of this accretion is thought to be driven by the galactic fountain, in which stellar feedback ejects disk gas into the halo, where it triggers the cooling and condensation of the surrounding hot corona before returning to the disk. The returned gas is therefore a mixture of recycled disk material and condensed coronal gas, but the relative proportions and their spatial distribution within individual fountain clouds have not been resolved observationally. We present a spatially resolved study of Complex K, an intermediate-velocity cloud spanning ∼40° in the northern Galactic halo, using archival far-ultraviolet spectra from HST/COS toward 20 background QSOs and 8 halo stars. We perform Voigt profile fitting and joint Bayesian photoionization modeling, constrained by H I 21 cm priors and an independent electron column density limit derived from pulsar dispersion measures. The majority of Complex K components have super-solar metallicities ($\langle \log Z/Z_{\odot} \rangle = 0.38$, i.e., ∼2.4 $Z_{\odot}$) and infalling kinematics ($v_z \sim -100$ km s^{-1}), confirming a Galactic disk origin. A minority of 3–4 components have sub-solar to near-solar metallicities, high densities, low Hα intensities, and peripheral spatial locations consistent with recently condensed coronal gas at the cloud boundary. We estimate a total gas mass of ∼5×10^5 $M_{\odot}$, assuming distance of 3 kpc, and a mass infall rate of ∼0.01 $M_{\odot}$ yr^{-1}. These results demonstrate that fountain-driven accretion returns gas to the disk spanning a range of metallicities set by the degree of coronal mixing, substantially higher than the metal-poor infall assumed in

standard chemical evolution models.

1 Introduction

The nature of gas accreting onto galaxy disks is a central question in galaxy evolution. Cosmological simulations predict that at low redshift, the gas fueling star formation in Milky Way-mass galaxies is not predominantly pristine material from the intergalactic medium but rather a mixture of recycled wind material, gas stripped from satellites, and condensed halo gas (Hafen et al. 2019 2020). The metallicity of this accreting gas is a fundamental input to Galactic chemical evolution. Models require sustained inflow of metal-poor gas, typically $Z \lesssim 0.1\ Z_\odot$ (Chiappini et al. 2001; Schönrich et al. 2010; Tosi 1988), to resolve the G-dwarf problem (Larson 1972; Pagel & Patchett 1975) and reproduce the observed metallicity distribution of disk stars. But if a substantial fraction of the gas reaching the disk is recycled material with near-solar or even super-solar metallicity, as the intermediate-velocity cloud (IVC) population suggests (Richter 2017; Wakker 2001), the averaged metallicity of inflow could be much higher than the standard picture assumes. Recently, Johnson et al. (2025) demonstrated that stellar metallicities in the Milky Way disk are approximately independent of age up to ∼9 Gyr at fixed Galactocentric radius, favoring a chemical equilibrium in which metal production by star formation is balanced by losses to outflows and star formation itself, and by dilution from accretion. What sets the metallicity of this accreting gas, and through what physical mechanism it reaches the disk, remain open questions.

The galactic fountain provides one mechanism for delivering gas to the disk. Supernova feedback ejects metal-rich ISM gas into the lower halo, where it decelerates, cools, and returns on timescales of ∼50–100 Myr (Bregman 1980; Fraternali & Binney 2006; Shapiro & Field 1976). As fountain clouds travel through the hot Galactic corona, turbulent mixing at the cloud-halo interface triggers radiative cooling of the ambient coronal gas, whose cooling time would otherwise exceed several Gyr (Armillotta et al. 2016; Marinacci et al. 2010). This fountain-driven condensation entrains metal-poor coronal material into the returning flow, producing gas at intermediate metallicities between the disk and the corona (Fraternali 2017). The fountain thereby converts hot, inaccessible halo gas into cold, accreting material, potentially providing the metal-poor dilution that GCE models require. Evidence for this process extends beyond the Milky Way. Extraplanar H I gas lagging behind disk rotation has been observed in nearby edge-on spirals such as NGC 891 (Oosterloo et al. 2007) and NGC 2403 (Fraternali et al. 2002), and its kinematics require the accretion of material with low angular momentum consistent with coronal condensation (Fraternali & Binney 2008; Marinacci et al. 2011). These observations establish the fountain as a generic feature of star-forming disk galaxies.

In the Milky Way, the extraplanar cold gas clouds are observed as high-velocity clouds (HVCs; $|v_{\rm LSR}| > 90\,{\rm km\,s^{-1}}$) and intermediate-velocity clouds (IVCs; $40 \lesssim |v_{\rm LSR}| \lesssim 90\,{\rm km\,s^{-1}}$), extensively cataloged in H I 21 cm surveys (e.g., Putman et al. 2002). IVCs are predominantly near-solar in metallicity and lie close to the disk ($d \lesssim 3$ kpc), consistent with recycled fountain material (Richter 2017; Wakker 2001). HVCs tend to be more metal-poor ($Z \sim 0.1$–$0.3\ Z_\odot$) and more distant, with origins attributed to IGM accretion, satellite stripping, or fountain-driven condensation at large halo distances (Fox et al. 2013; Putman et al. 2012; Wakker et al. 1999). Fraternali et al. (2015) demonstrated this last mechanism for Complex C, the prototypical HVC, showing that it originated from a superbubble blowout ∼150 Myr ago whose ejecta triggered the condensation of coronal gas that now dominates the cloud's mass. This result shows that the low metallicity of Complex C does not require a purely extragalactic origin; instead, it reflects the large fraction of coronal gas that has condensed onto the fountain ejecta over its trajectory.

While the IVC population as a whole is thought to trace fountain recycling, with near-solar metallicities consistent with a disk origin (Richter 2017; Wakker 2001), the gas that ultimately returns to the disk is expected to be a mixture of this metal-rich fountain material and metal-poor coronal gas accumulated along the trajectory. In the fountain-driven accretion scenario, the distinction between IVCs and HVCs may largely reflect this mixing process. More energetic ejections reach greater heights, spend more time in the halo, and accumulate more coronal material, producing the sub-solar metallicities characteristic of HVCs, while less energetic ejections remain closer to the disk and return with compositions closer to the ISM from which they were launched (Fraternali 2017). The relative proportions of recycled disk gas and condensed coronal material in the returning flow determine the effective metallicity of fountain-driven accretion, which in turn sets its impact on the chemical evolution of the Galactic disk. However, metallicity measurements for individual IVCs are typically limited to one or a few sight lines, leaving the internal mixing structure of the fountain flow unresolved.

A further limitation is that most metallicity studies of halo clouds have targeted the dense neutral gas detectable in H I 21 cm emission, assuming negligible ionization corrections (Collins et al. 2007; Wakker 2001; Wakker et al. 1999). Yet the ionized gas envelopes surrounding these clouds likely dominate the total mass (Lehner & Howk 2011; Putman et al. 2012), and their metallicities are poorly constrained. Measuring the metallicity of this ionized phase requires knowing the total hydrogen column density $N_{\rm H} = N_{\rm HI} + N_{\rm HII}$, where $N_{\rm HII}$ is not directly observable and must be inferred through photoionization modeling. This introduces degeneracies between metallicity, ionization parameter, and $N_{\rm HI}$ that are difficult to break without an independent constraint on the total ionized column (Collins et al. 2007; Fox et al. 2005). Howk et al. (2006) first demonstrated that pulsar dispersion measures can serve as an independent constraint on the ionized hydrogen column by providing a precise measurement of the electron column density along the same sight lines. In Choi et al. (2024, Chapter 2), we extended this approach to separately measure the metallicity of kinematically distinct gas components, tightening metallicity estimates for ionized halo gas.

Resolving the mixing between recycled disk gas and condensed coronal material within a single fountain cloud requires spatially resolved measurements of metallicity and kinematics across its extent. Such measurements would constrain both the physical mechanism of fountain-driven condensation and the effective metallicity at which fountain gas returns to the disk, a quantity that directly affects the rate of metal dilution in chemical evolution models. In this paper, we study Complex K as a test case. Complex K is a large (∼40° on the sky) IVC in the northern Galactic halo ($l \approx 30-70°$, $b \approx 25-70°$) at velocities of $v_{\rm LSR} \approx -95$ to -60 km s^{-1}, with a distance upper limit of $d < 3.6$ kpc (Lehner et al. 2022). Previous studies have shown near-solar to super-solar metallicity along individual sight lines (Choi et al. 2024; Wakker 2001), supporting a disk origin, but have not probed the cloud with sufficient spatial coverage to map its internal structure. Its large angular extent enables absorption spectroscopy toward multiple background sources, and in this paper, we exploit this to construct the spatially resolved map of metallicity, ionization, and kinematics across this potential fountain-driven cloud. We use archival far-ultraviolet (FUV) spectra from the *Hubble Space Telescope* (*HST*) Cosmic Origins Spectrograph (COS) toward 20 background QSOs and 7 halo stars to probe Complex K. We describe our data in Section 2. We perform Voigt profile fitting to measure ion column densities for each kinematic component (Section 3), followed by joint Bayesian photoionization modeling with CLOUDY, constrained by H I 21 cm priors from HI4PI (HI4PI Collaboration et al. 2016) and an independent electron column density limit from pulsar dispersion measures (Section 4). We present our results in Section 5, including additional distance constraints from optical spectroscopy of blue horizontal branch stars (Section 6). We estimate mass and discuss the implications for the Galactic fountain and chemical evolution in Section 7.

2 Data

The FUV is ideal for probing absorption from Complex K, as copious transition lines from various ionized metals characteristic of cold and cool ionized gas fall in this wavelength regime. We obtain FUV spectra of background QSOs and halo stars from the Barbara A. Mikulski Archive for Space Telescopes (MAST), searching for *Hubble Space Telescope* (*HST*) observations taken with the Cosmic Origins Spectrograph (COS). To spectrally resolve absorption components associated with Complex K ($v_{\rm LSR} \sim -95$ to -60 km s^{-1}) from the Galactic ISM (typically $|v_{\rm LSR}| \lesssim 20$ km s^{-1}), we use the COS G130M and G160M, which provide FUV coverage at spectral resolutions of $R \sim 12{,}000$–$17{,}000$ and $13{,}000$–$20{,}000$, respectively.

We select sight lines whose Galactic coordinates fall within the known H I extent of Complex K ($l \approx 30-70^\circ$, $b \approx 25-70^\circ$), extending our search box by $\sim 10^\circ$ given that ionized gas may be more extended than the H I. Our search returns a sample of 20 QSOs and 10 UV-bright halo stars, including post-AGB stars and blue horizontal branch (BHB) stars. The QSOs are drawn from the COS-GAL dataset (Zheng et al. 2019), which provides fully reduced and normalized FUV spectra of QSOs as High-Level Science Products (HLSPs) in MAST. The halo star sight lines use coadded spectra from the HST Spectroscopic Legacy Archive (HSLA; Peeples et al. 2017b). We exclude halo stars whose radial velocities in the LSR frame fall within $-115 \leq v_{\rm LSR} \leq -45\,{\rm km\,s^{-1}}$, corresponding to the Complex K velocity range extended by ~ 20 km s^{-1} on each side, within which stellar absorption cannot be resolved from Complex K by COS.

For the COS-GAL sight lines, we adopt the normalized spectra as provided. For the remaining sight lines, we normalize the continua using the continuum-fitting tool in `linetools` (Prochaska et al. 2017b), which interactively fits a spline to absorption-free regions selected by visual inspection. This matches the procedure used by COS-GAL, ensuring consistent continuum normalization across the full sample. A summary of all sight lines, including coordinates, COS gratings, and S/N, is presented in Table 3.1 for QSOs with their redshifts, and in Table 3.2 for halo stars with their (spectro)photometric distances.

Table 3.1: Summary of COS-GAL QSO Archival Data.

ID	R.A. (deg)	Decl. (deg)	l (deg)	b (deg)	z	Grating	S/N	Program ID
2MASS J1431258+244220	217.86	24.71	32.42	67.42	0.406	G130M	17.2	12603/13342

Continued on next page

Table 3.1 – continued

ID	R.A. (deg)	Decl. (deg)	l (deg)	b (deg)	z	Grating	S/N	Program ID
Mrk 877	245.05	17.41	32.89	41.08	0.112	G130M	16.2	12569
2MASX J15474353+2052167	236.93	20.87	33.90	49.46	0.264	G130M/G160M	17.2	13398/6611
2MASX J14510879+2709272	222.79	27.16	39.95	63.43	0.065	G130M/G160M	8.5	12248
2MASX J16194054+2543233	244.92	25.72	43.59	43.70	0.269	G130M/G160M	9.1	13832
2MASS J15442726+2743242	236.11	27.72	44.13	51.81	0.163	G130M	5.1	12603
Ton 236	232.17	28.43	44.43	55.35	0.450	G130M/G160M	18.0	12038
QSO J1541+2817	235.34	28.29	44.86	52.57	0.375	G130M	7.8	12603
2MASS J15443053+2827567	236.13	28.47	45.32	51.91	0.231	G130M	7.1	13423
QSO J1454+3046	223.60	30.78	48.07	62.94	0.465	G130M	6.3	12603
Mrk 504	255.28	29.41	51.08	35.65	0.035	G130M	8.1	12275
QSO J1619+3342	244.82	33.71	54.59	45.18	0.471	G130M/G160M	11.5	11598
QSO J1445+3428	221.30	34.47	56.74	64.59	0.697	G130M/G160M	5.9	11598
QSO J1553+3548	238.27	35.81	57.26	50.67	0.722	G130M/G160M	7.2	11598
QSO J1555+3628	238.77	36.48	58.32	50.27	0.714	G130M/G160M	5.7	11598
Mrk 478	220.53	35.44	59.24	65.03	0.079	G130M	20.6	12569
QSO B1630+3744	248.00	37.63	60.34	42.94	1.478	G130M/G160M	36.8	11741
QSO J1435+3604	218.80	36.08	61.52	66.26	0.429	G130M/G160M	5.7	11598
QSO J1550+4001	237.70	40.03	63.96	50.94	0.497	G130M/G160M	6.5	11598
QSO J1616+4154	244.21	41.90	66.28	45.91	0.441	G130M/G160M	6.5	11598

Table 3.2: Summary of Halo Star COS Archival Data.

ID	R.A. (deg)	Decl. (deg)	l (deg)	b (deg)	d (kpc)	$v_{*,\mathrm{LSR}}$ (km s^{-1})	Grating	S/N	PID
PG 1708+142	257.82	14.15	34.91	28.47	10.3 ± 2.0^a	-28.0	G130M/G160M	22.4	11592
2MASS J13411984+2823586	205.33	28.40	42.39	78.89	11.3 ± 1.1^b	-114.5	G160M	14.7	14140
vZ 1128	205.57	28.43	42.50	78.68	10.7 ± 0.9^c	-137.0	G130M/G160M	37.0	11527
PG 1704+222	256.69	22.10	43.06	32.36	7.0 ± 1.8^d	-14.2	G130M/G160M	39.5	11592
2MASS J16413368+3626077	250.39	36.44	58.97	40.94	7.9 ± 0.6^c	-227.0	G130M/G160M	56.6	11527
SDSS J141557.13+371658.2	213.99	37.28	67.92	69.51	9.9 ± 1.0^b	-121.9	G160M	14.7	14140
SDSS J145953.97+412851.1	224.98	41.48	69.94	60.08	15.3 ± 1.5^b	-168.9	G160M	12.1	14140

Note. Distance references: ^{a}Gaia Collaboration et al. (2023); ^{b}Xue et al. (2011); ^{c}O'Malley et al. (2017); ^{d}Mooney et al. (2002).

3 Absorption Line Fitting

We present an absorption-line fitting framework for identifying absorption components, measuring ion column densities, and constraining the metallicity and ionization properties of halo clouds. The procedure consists of three steps: (1) identifying absorption lines across multiple ion species (Section 3.1), (2) fitting Voigt profiles informed by the line identifications from step (1), including components inferred from other ion species that may be missing or saturated in a given transition (Section 3.2), and (3) photoionization modeling with CLOUDY (C17; Ferland et al. 2017) to estimate metallcity (Section 4.2).

3.1 Component Identification

We identify absorption components in the continuum-normalized UV spectra to separate features originating from Complex K, Milky Way ISM, other halo clouds, and stellar absorption in the case of halo stars. The identification is performed in velocity space in the local standard of rest (LSR) frame which is conventionally used for Galactic halo studies and enables direct comparison with previous work.

Complex K spans $-90 \lesssim v_{\rm LSR} \lesssim -60$ km s^{-1}, but Complex C, which overlaps with the lower region of Complex K in projection, extends over $-220 \lesssim v_{\rm LSR} \lesssim -90$ km s^{-1}. To ensure that our velocity window fully covers both complexes and allows us to distinguish their absorption if both are detected along a given sight line, we search for components over the range $-250 < v_{\rm LSR} < 50$ km s^{-1}. We identify all strong ISM lines[1] that fall within the spectral coverage using the `IGMGuesses` GUI in `pyigm`[2], which displays each transition in velocity space, facilitating visual identification of components by their velocity offsets. Initial estimates of the Voigt profile parameters — ion column density $N_{\rm ion}$, Doppler parameter b, and $v_{\rm LSR}$ — are recorded for each component. Where multiple transitions

[1] As defined in the `linetools` line list (Prochaska et al. 2017b); these include the most commonly observed transitions in UV.

[2] `https://github.com/pyigm/pyigm`

are available for a given ion species, we base the identification on the transition with the lowest oscillator strength to minimize the effects of saturation.

3.2 Voigt Profile Fitting

Based on the component identification described in Section 3.1, we perform Voigt profile fitting to measure ion column densities ($N_{\rm ion}$), Doppler parameters (b), and LSR velocity centroids ($v_{\rm LSR}$) for each absorption component.

Component Grouping. Before fitting, we group the identified components across all ion species by their velocity centroids. Components are sorted by $v_{\rm LSR}$ and sequentially assigned to the nearest existing group within a velocity tolerance of $\Delta v = 30\,{\rm km\,s^{-1}}$, subject to the constraint that each velocity group represents a single kinematic component per ion species. If no eligible group exists, a new group is created, and the group mean velocity is updated after each assignment. Because this initial assignment depends on the order in which components are processed, and because group mean velocities shift as new members are added, the assignment may not be optimal after a single pass through all components across all ion species. We therefore repeat the group assignment iteratively. In each iteration, the algorithm cycles through every component individually: the component is removed from its current group, the group mean velocity is recalculated without it, and the component is reassigned to the nearest eligible group based on the updated means. This process repeats until no component changes its group assignment.

Voigt Profile Fitting. For each ion species, we jointly fit Voigt profiles to all identified components across all available transitions of that ion within the spectral coverage. The fitting is performed over the same velocity window as the component identification, $-250 < v_{\rm LSR} < 50$ km s^{-1}. The Voigt profiles are convolved with the instrument line-spread function (LSF). Before fitting, we flag and exclude transitions from the fit where lines from other ion species are present in the fitting window, as they are potentially blended. We adopt the COS G130M and G160M LSFs (Ghavamian et al. 2009), selecting the appropriate grating based on the spectral coverage of the data. The algorithm allows any available COS grating/lifetime position (LP); however, the coadded spectra used in this work do not retain individual LP information, and thus we adopt LP3 for all observations.

The model parameters, $\log N$, b, and $v_{\rm LSR}$ for each component, are sampled using a Hamiltonian Monte Carlo (HMC) method. We adopt uniform priors centered on the initial estimates from the component identification (Section 3.1), with half-widths of $\Delta \log N = 1$ dex, $\Delta b = 15\,{\rm km\,s^{-1}}$, and $\Delta v = 15\,{\rm km\,s^{-1}}$. We use the No-U-Turn Sampler (NUTS; Hoffman & Gelman 2011) implemented in `NumPyro` (Bingham et al. 2019; Phan et al. 2019), with a normalizing flow reparameterization (Hoffman et al. 2019) to improve sampling efficiency. We run four parallel chains with $N_{\rm warmup} = 2000$ and $N_{\rm samples} = 5000$. Posterior medians and 1σ uncertainties are adopted as the final measurements.

The fitted $v_{\rm LSR}$ values may differ from the initial estimates used for grouping in Section 3.1, and we accordingly re-group the components based on the fitted values using the same algorithm. After re-grouping, we check whether any two groups are separated by less than 20 km s^{-1} (about COS resolution). If so, the two groups are merged into one, unless at least one ion species has components in both groups, indicating that the two groups are kinematically distinct.

Inferred Components and Upper Limits. After fitting and grouping, some velocity groups may lack a component in certain ion species. This can arise either from a true non-detection or because the component is unresolved, blended with a neighboring component which is common in saturated or nearly saturated lines. Since we focus on resolving Complex K, for groups within its velocity range ($-100 \leq v_{\rm LSR} \leq -50\,{\rm km\,s^{-1}}$), we check whether significant absorption ($> 3\sigma$) is present within the velocity range of the group. If absorption is detected, we inject an *inferred component* with initial column density estimated from the solar abundance ratio relative to the closest ion in ionization potential that has a detection in the same group, and re-fit the full set of components for that ion. This procedure allows the fit to recover column densities for components that are blended or too weak to be identified independently but whose presence is informed by detections in other ion species.

In the case of non-detection, we estimate a 2σ upper limit (95% confidence) on the column density using the apparent optical depth method (AODM; Savage & Sembach 1991). We refer to Bowen et al. (2008) for a detailed description of the method.

4 Photoionization

We fit the UV absorption lines using photoionization models to simultaneously constrain $\log N_{\rm HI}$, $\log Z$, and $\log U$ for each Complex K absorption component, classified as "group". We predict ion column densities $N_{\rm ion}$ from Cloudy grid via linear interpolation over ($\log N_{\rm HI}$, $\log Z$, $\log U$), generate model Voigt profiles, and jointly fit the UV spectra under the priors described below, together with an upper limit on the electron column density derived from pulsar dispersion measures.

4.1 Photoionization Model Grids

We perform photoionization modeling with the spectral synthesis code CLOUDY (C17; Ferland et al. 2017). Following Fox et al. (2005), we adopt a Milky Way ionizing radiation field that combines stellar radiation from the Galactic disk with the extragalactic UV background (Fig. 2.3). We generate a grid of cloud models parameterized by neutral hydrogen column density $N_{\rm HI}$, metallicity $Z/Z_\odot$, and ionization parameter U, the latter defined as the ratio of ionizing photon density to hydrogen density ($U \equiv n_\gamma/n_{\rm H} = \Phi/(c\,n_{\rm H})$). The grid spans $\log(N_{\rm HI}/{\rm cm}^{-2}) = 14$ to 21.5 in steps of 0.5 dex, $\log(Z/Z_\odot) = -2$ to $+1$ in steps of 0.1 dex, and $\log U = -5$ to 0 in steps of 0.5 dex. The metallicity range is deliberately extended well above solar to accommodate the super-solar values expected for fountain-origin gas, which is a key motivation for this study. Our grid adopts the standard simplifying assumptions that clouds are (1) in thermal and ionization equilibrium, (2) plane-parallel slabs of uniform density, and (3) characterized by solar relative abundances of the elements in the gas phase.

4.2 Joint Photoionization Fit

We perform a joint Bayesian fit of all absorption components within each sight line's fitting window. For each Complex K velocity component, CLOUDY interpolation yields the gas temperature T and predicted ion column densities $N_{\rm ion,comp}$, which are combined with the component velocity centroid $v_{\rm comp}$ and non-thermal Doppler parameter $b_{\rm comp}$ to generate Voigt profiles. Because we aim to characterize Complex K specifically, we restrict photoionization modeling to components within $-105 \leq v_{\rm LSR} \leq -50$ km s^{-1}, corresponding to the known Complex K velocity range (-95 to -60 km s^{-1}) expanded by ±10 km s^{-1}. Components outside this range, primarily from the Milky Way ISM, stellar, and other halo complexes, are held fixed at the Voigt-fit parameters from Section 3.2. All component profiles within the fitting window are summed, convolved with the COS LSF, and jointly fit to the continuum-normalized spectra under a Gaussian likelihood with per-pixel uncertainties from the COS error array. The code will be available at `https://github.com/boeunchoi`; a detailed description and validation will be presented in a separate software paper. We present an example of the joint Voigt profile fit to the absorption features in Fig. 3.2, using the photoionization modeling described in this section.

H I column density. We use the HI4PI 21-cm all-sky survey (HI4PI Collaboration et al. 2016) to estimate $N_{\rm HI}$ toward each sight line over the velocity range of Complex K. Because the HI4PI beam (FWHM $\sim 16.2'$) is substantially larger than the COS aperture ($2.5''$), and because not every UV sight line intersects a detected H I cloud, these measurements are subject to beam-smearing effects and are available only for a subset of sight lines. We therefore use HI4PI to place priors on $N_{\rm HI}$ rather than fixed values.

For each velocity component at $v_{\rm group}$, we integrate the HI4PI spectrum over $v_{\rm group} \pm 20$ km s^{-1}, chosen to encompass the typical line widths of the detected low ions in our sample ($b \lesssim 40\,{\rm km\,s^{-1}}$). If the integrated column density exceeds the HI4PI column-density sensitivity over this velocity window ($N_{\rm HI} = 2.3 \times 10^{18}$ cm^{-2}), we adopt a uniform prior on $\log N_{\rm HI}$ spanning ± 0.3 dex around the measured value to conservatively allow for beam-smearing effects. If the integrated value falls below the sensitivity limit, we compute the rms of the HI4PI spectrum over the integration window and derive a 3σ upper limit on $N_{\rm HI}$; in this case, we adopt a uniform prior on $\log N_{\rm HI}$ over the range [14, $\log N_{\rm HI,upper}$], where the lower bound corresponds to the minimum $N_{\rm HI}$ of our CLOUDY model grid.

Doppler b-parameter. The Doppler b-parameter for each ion is decomposed into thermal and non-thermal components,

$$b = \sqrt{b_{\rm th}^2 + b_{\rm nt}^2}, \quad b_{\rm th} = \sqrt{\frac{2k_{\rm B}T}{m_{\rm ion}}}, \tag{3.1}$$

where T is the gas temperature predicted by the Cloudy model and $m_{\rm ion} \approx 2\,Z_{\rm atom}\,m_{\rm p}$ is the ion mass, approximated as twice the atomic number $Z_{\rm atom}$ times the proton mass. The non-thermal component is treated as a free parameter shared across all ions of a given velocity component, with a uniform prior over [0, 25] km s^{-1}.

Velocity centroid. The velocity centroid $v_{\rm comp}$ is treated as a free parameter shared across all ions of a given component. We adopt a uniform prior of width ± 15 km s^{-1} centered on the group velocity determined in Section 3.2, comparable to the COS spectral resolution.

Electron column density from pulsar dispersion measures. H I constraints are available for only a subset of our sight lines, limiting our ability to constrain $\log N_{\rm HI}$ and therefore metallicity directly from 21-cm data alone. We supplement the H I constraint with an upper limit on the total electron column density N_e derived from pulsar dispersion measures (DMs), which effectively constrains the ionized hydrogen column density $N_{\rm HII}$ that dominates the gas mass in the diffuse Galactic halo (Putman et al. 2012). Pulsar DMs have previously been used to constrain the metallicity of Galactic halo gas by pairing pulsars in globular clusters with UV-bright halo stars at matched distances (Choi et al. 2024; Howk et al. 2006). Our sample lacks such pulsar–halo star pairs, especially the majority of our sight lines target QSOs, which provide no line-of-sight distance information, and thus, we adopt a statistical approach based on the distribution of pulsar DMs in the direction of Complex K.

Figure 3.1a shows the total electron column density $N_{e,\rm DM}$ from the ATNF pulsar catalog (Manchester et al. 2005) as a function of pulsar distance. Teal points show all ATNF pulsars more than 1 kpc from the Galactic plane, while pink points show pulsars within the Complex K region on the sky. Complex K has a known distance upper limit of $d < 3.6$ kpc (Lehner et al. 2022), and all pulsars in this region within that distance have $\log\,(N_{e,\rm DM}/{\rm cm}^{-2}) \lesssim 20.25$. We use this distribution to place a probabilistic upper limit on N_e through the halo gas toward Complex K.

The model electron column density is computed self-consistently by CLOUDY with a helium correction, $N_{e,\rm model} = N_{\rm HII} + N_{\rm HeII} + 2\,N_{\rm HeIII}$. We define the N_e likelihood as a one-sided Gaussian in $\log N_{e,\rm model}$,

$$\mathcal{L}_{N_e} = \frac{1}{2}\left[1 + {\rm erf}\left(\frac{\log N_{e,\rm limit} - \log N_{e,\rm model}}{\sqrt{2}\,\sigma_{N_e}}\right)\right], \tag{3.2}$$

with $\log N_{e,\rm limit} = 20.25$ and $\sigma_{N_e} = 0.25$ dex reflecting the scatter in pulsar-derived $\log N_{e,\rm DM}$ values within the Complex K region. This formulation penalizes models progressively as $N_{e,\rm model}$ approaches and exceeds the observed pulsar distribution, rather than imposing a hard cutoff. The spectral likelihood evaluates a Gaussian term for each of the thousands of fitted pixels, whereas the N_e constraint contributes only a single scalar term. Without

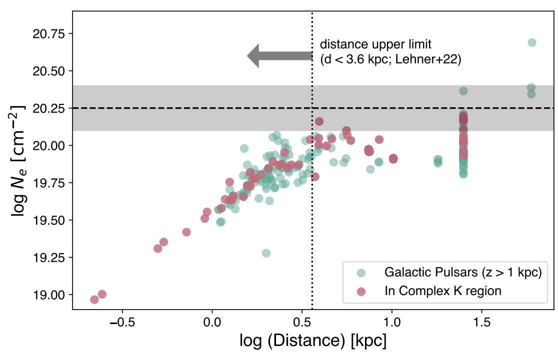

(a) Electron column densities derived from ATNF pulsar dispersion measures

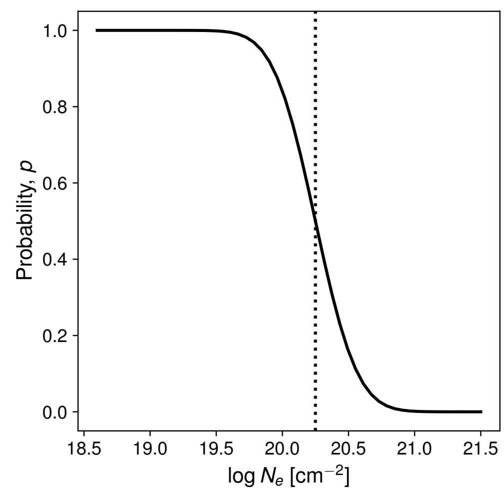

(b) The applied likelihood of N_e

Figure 3.1: Electron column density derived from ATNF pulsar dispersion measures as a function of pulsar distance (left). All Galactic pulsars at $|z| > 1$ kpc are shown (teal), along with pulsars within the Complex K region on the sky (red). Pulsars in the Complex K region within the upper distance limit of $d < 3.6$ kpc (Lehner et al. 2022) all lie below $\log(N_e/\mathrm{cm}^{-2}) \lesssim 20.25$, which we adopt as the electron column density upper limit. The N_e likelihood function $\log N_{e,\mathrm{model}}$ (right; Equation 3.2).

reweighting, the N_e constraint would be negligible relative to the combined spectral likelihood despite being an informative external constraint on the ionized gas column. We therefore multiply $\log \mathcal{L}_{N_e}$ by the total number of fitted spectral pixels, giving the N_e constraint weight comparable to the spectral data as a whole. Together with the H I prior and the observed metal-line column densities, this N_e likelihood breaks the degeneracy between N_{HI}, Z, and U that would otherwise limit our metallicity constraints on sight lines lacking direct H I measurements.

Posterior sampling. Posterior sampling proceeds in two stages. We first train a block neural autoregressive flow guide (`AutoBNAFNormal` in `NumPyro`; Phan et al. 2019) via stochastic variational inference to learn an approximate posterior. The trained guide is then used as a neural transport reparameterization (NeuTra; Hoffman et al. 2019) for the No-U-Turn Sampler (NUTS; Hoffman & Gelman 2011), with $N_{\mathrm{warmup}} = 2000$ and $N_{\mathrm{samples}} =$

8000 across six parallel chains initialized at the posterior median from the guide. Posterior medians and 1σ (16th/84th percentile) uncertainties are adopted as the final measurements.

5 Photionization Modelling Results

We present the gas properties inferred from the photoionization modelling described in Section 4. We refer to a velocity component as a "Complex K component" when its fitted velocity centroid falls within the conventional Complex K velocity range, $-95 \leq v_{\rm LSR} \leq -60$ km s^{-1} (Wakker 2001). The photoionization fit results for all Complex K components are summarized in Table 3.3. We report the posterior median and 1σ uncertainties for velocity $v_{\rm LSR}$, H I column density $\log N_{\rm HI}$, metallicity $\log Z/Z_\odot$, and ionization parameter $\log U$. We additionally derive the hydrogen number density $n_{\rm H}$ from $\log U$ together with the adopted incident radiation (Fox et al. 2005). Because direct distance estimates to individual Complex K components are not available, we evaluate the radiation field over the range $d = 0.2$ to $d = 4$ kpc for each sight line, spanning roughly the ISM scale height to the upper distance limit on Complex K (Lehner et al. 2022). For each component, we adopt the median $n_{\rm H}$ over this distance range as the fiducial value, with the minimum and maximum taken as a systematic uncertainty range as listed in Table 3.3.

Table 3.3: Photoionization model results for Complex K components.

Name	l (deg)	b (deg)	$v_{\rm LSR}$ (km s^{-1})	$\log N_{\rm HI}$ (cm^{-2})	$\log Z/Z_\odot$	$\log U$	$\log n_{\rm H}$ (cm^{-3})
2MASS J1431258+244220	32.42	67.42	-70.1 ± 0.7	18.37 ± 0.03	0.57 ± 0.06	-2.71 ± 0.04	$-1.92^{+0.23}_{-0.07}$
Mrk 877	32.89	41.08	-73.5 ± 2.4	16.06 ± 0.15	0.14 ± 0.13	-2.46 ± 0.08	$-2.03^{+0.35}_{-0.06}$
2MASX J14510879+2709272	39.95	63.43	-77.4 ± 2.0	19.13 ± 0.12	0.73 ± 0.12	-4.76 ± 0.09	$0.15^{+0.23}_{-0.08}$
vZ 1128	42.50	78.68	-61.0 ± 0.6	17.61 ± 0.05	-0.25 ± 0.05	-3.95 ± 0.04	$-0.75^{+0.26}_{-0.06}$
PG 1704+222	43.06	32.36	-69.4 ± 1.5	14.24 ± 0.03	0.36 ± 0.03	-1.49 ± 0.02	$-2.90^{+0.37}_{-0.15}$
2MASS J15442726+2743242	44.13	51.81	-86.9 ± 2.5	15.51 ± 0.29	0.69 ± 0.20	-1.94 ± 0.20	$-2.64^{+0.32}_{-0.07}$
Ton 236	44.43	55.35	-88.7 ± 0.6	15.57 ± 0.07	0.10 ± 0.07	-2.20 ± 0.04	$-2.40^{+0.29}_{-0.07}$

Continued on next page

Table 3.3 – continued

Name	l (deg)	b (deg)	$v_{\rm LSR}$ (km s^{-1})	$\log N_{\rm HI}$ (cm^{-2})	$\log Z/Z_{\odot}$	$\log U$	$\log n_{\rm H}$ (cm^{-3})
QSO J1541+2817	44.86	52.57	-63.4 ± 0.2	18.80 ± 0.04	0.96 ± 0.03	-3.52 ± 0.16	$-1.07^{+0.32}_{-0.06}$
2MASS J15443053+2827567	45.32	51.91	-73.2 ± 0.1	16.63 ± 0.04	0.30 ± 0.03	-2.00 ± 0.06	$-2.58^{+0.32}_{-0.07}$
QSO J1454+3046	48.07	62.94	-83.5 ± 2.2	16.66 ± 0.39	0.58 ± 0.27	-2.46 ± 0.24	$-2.17^{+0.26}_{-0.07}$
QSO J1619+3342	54.59	45.18	-75.7 ± 0.9	17.41 ± 0.09	0.72 ± 0.10	-3.19 ± 0.05	$-1.41^{+0.45}_{-0.05}$
QSO J1445+3428	56.74	64.59	-76.1 ± 5.1	17.19 ± 0.22	0.59 ± 0.21	-4.19 ± 0.24	$-0.47^{+0.29}_{-0.07}$
			-66.1 ± 0.0	18.93 ± 0.01	0.51 ± 0.02	-2.71 ± 0.01	$-1.90^{+0.23}_{-0.08}$
QSO J1553+3548	57.26	50.67	-83.7 ± 1.1	14.42 ± 0.13	0.41 ± 0.08	-1.42 ± 0.09	$-3.22^{+0.41}_{-0.06}$
Gaia DR3 1293015027042062848	57.61	63.67	-93.2 ± 3.4	15.49 ± 0.08	0.49 ± 0.05	-2.08 ± 0.05	$-2.58^{+0.30}_{-0.07}$
QSO J1435+3604	61.52	66.26	-60.5 ± 0.4	17.08 ± 0.10	0.64 ± 0.04	-2.38 ± 0.03	$-2.30^{+0.30}_{-0.06}$
			-63.3 ± 5.4	18.57 ± 0.14	0.04 ± 0.29	-4.13 ± 0.20	$-0.55^{+0.30}_{-0.06}$
QSO J1550+4001	63.96	50.94	-86.4 ± 0.8	17.41 ± 0.26	0.18 ± 0.27	-4.47 ± 0.19	$-0.20^{+0.45}_{-0.05}$
SDSS J145953.97+412851.1	69.94	60.08	-92.7 ± 1.6	15.91 ± 0.34	0.34 ± 0.22	-2.46 ± 0.17	$-2.24^{+0.40}_{-0.05}$
			-64.1 ± 1.4	18.47 ± 0.12	-0.46 ± 0.09	-4.53 ± 0.13	$-0.17^{+0.40}_{-0.05}$

To check consistency with the large-scale structure of Complex K, we compare our fitted component properties to the H I 21 cm emission. Figure 3.3 shows the all-sky map of Galactic HVCs from the HI4PI survey (HI4PI Collaboration et al. 2016; Westmeier 2018). The two panels display the LSR velocity (Fig. 3.3a) and the H I column density (Fig. 3.3b). We overplot each Complex K component as a square marker colored by its fitted value. The fitted velocity centroids agree well with the H I velocity field over the body of the cloud. Components on sight lines outside the main H I extent of Complex K tend toward less negative velocities, suggestive of an ionized envelope extending beyond the cloud body at slightly shifted kinematics. Only a subset of our sight lines intersect H I detectable in 21 cm emission, as discussed in Section 4.2. The fitted H I column densities are likewise consistent with HI4PI where the comparison is possible. Many components have low fitted $N_{\rm HI}$ because their sight lines fall below the HI4PI sensitivity limit, in which case the prior pushes the posterior toward the lower bound of our model grid.

Our Complex K components are substantially ionized, and a comparison with Hα is,

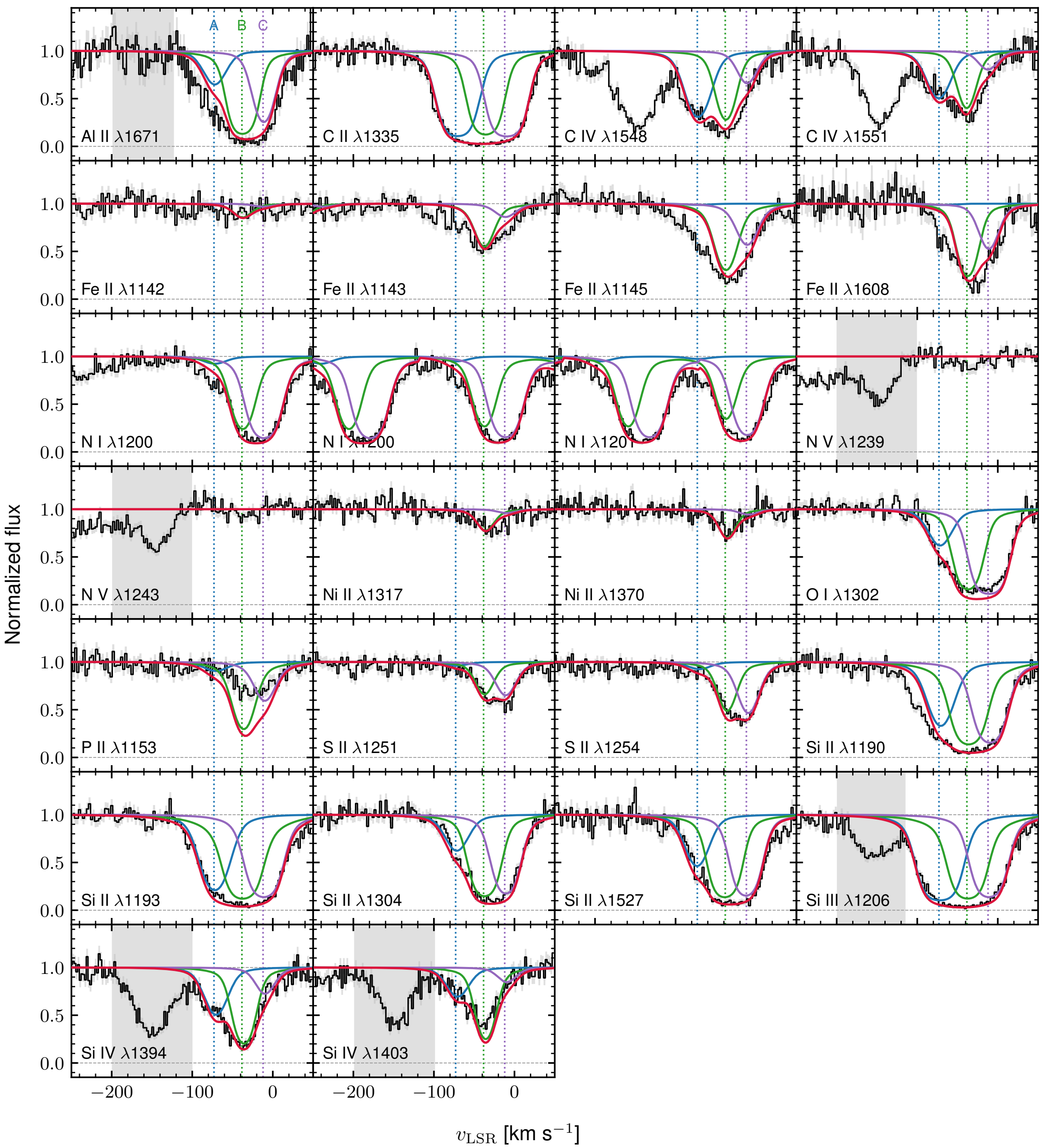

Figure 3.2: Jointly fitted Voigt profiles based on the photoionization model toward the halo star vZ 1128. The red solid line shows the joint profile fit. Stellar absorption features and regions of unreliable continuum are masked (gray shaded) during the fitting process. The resulting fit is consistent across ion species.

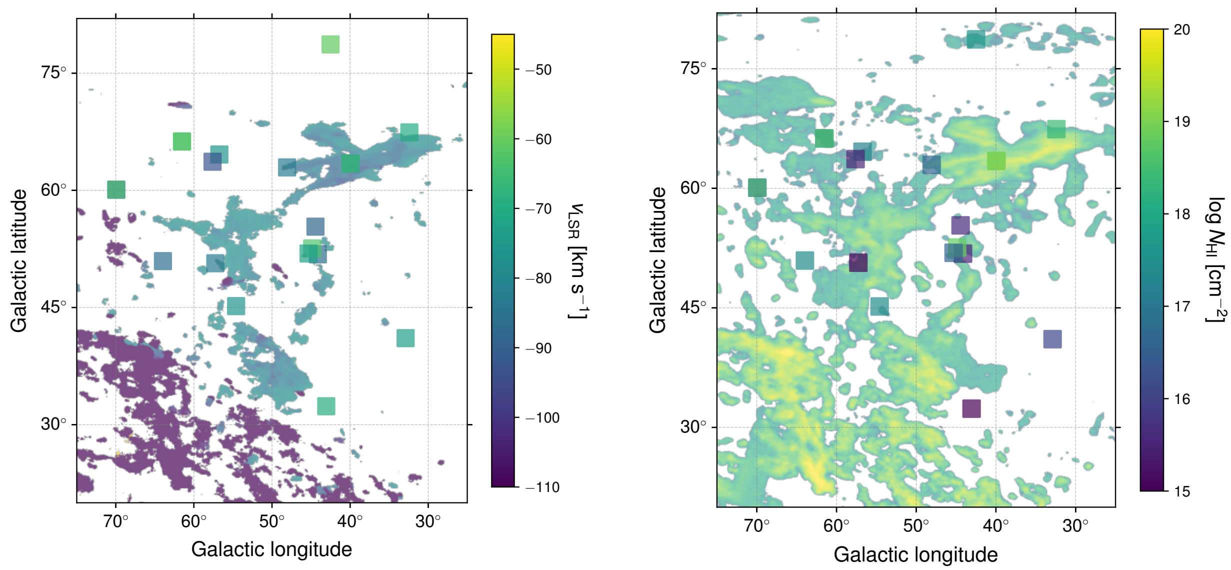

(a) v_{LSR} (b) N_{HI}

Figure 3.3: LSR velocity (left) and H I column density (right) maps of H I 21 cm map from HI4PI (Westmeier 2018), with our Complex K components overplotted as squares.

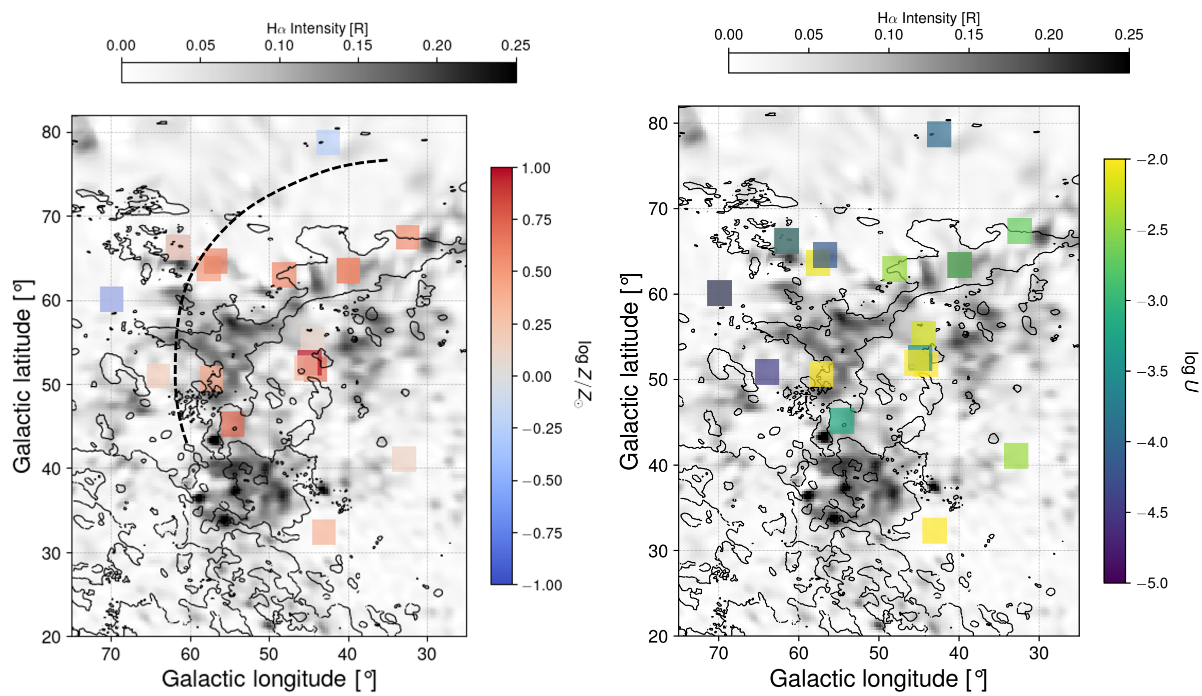

(a) Metallicity $\log(Z/Z_\odot)$ (b) Ionization parameter $\log U$

Figure 3.4: Distribution of Complex K component properties on the Hα map integrated over the Complex K velocity range from WHAM (Haffner et al. 2003). The black contour marks $N_{HI} = 10^{18}$ cm^{-2} from HI4PI. Square markers show our Complex K components, colored by the fitted metallicity (left) and ionization parameter (right).

therefore, informative. The Hα emission from ionized component of Complex K seen in WHAM (Haffner et al. 2003) extends beyond the H I body of the cloud (Haffner et al. 2001), and many of our sight lines lie outside the H I extent as well. We use `whampy`[3] to access the WHAM survey data. In Fig. 3.4, we show the Hα map integrated over Complex K velocity range (grayscale) with H I contour of $N_{\rm HI} = 10^{18}$ cm^{-2} (black solid). The two panels show the fitted metallicity $\log Z/Z_\odot$ (Fig. 3.4a) and ionization parameter $\log U$ (Fig. 3.4b). The metallicity varies across the complex, but the majority of components are super-solar.

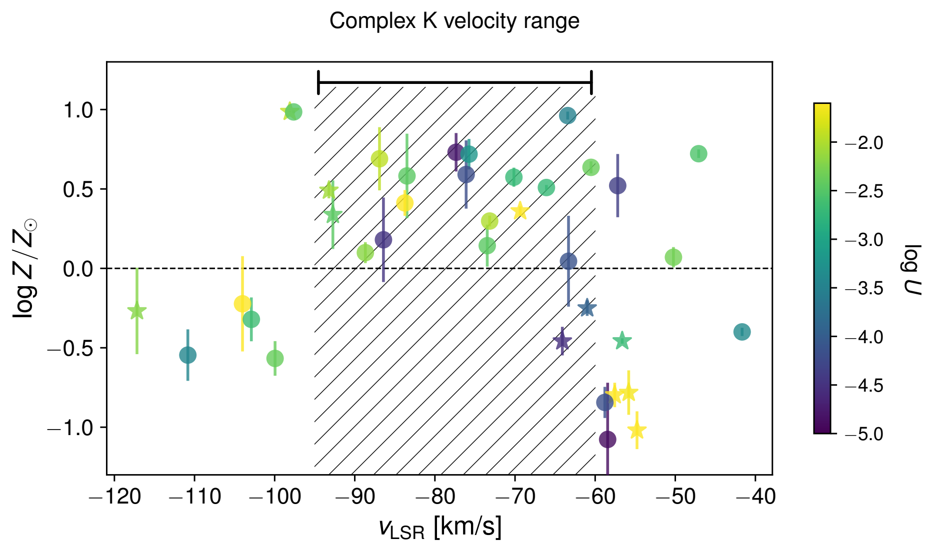

Figure 3.5: Fitted metallicity $\log(Z/Z_\odot)$ and LSR velocity for all components, colored by ionization parameter. The hatched region marks the Complex K velocity range; components within it are the Complex K components. Error bars show 1σ posterior uncertainties, and the horizontal dashed line marks solar metallicity.

Figure 3.5 shows the fitted metallicity as a function of LSR velocity for all Complex K components, colored by ionization parameter $\log U$. The hatched region marks Complex K velocity range. The Complex K components are metal-rich relative to the rest of the sample, with a mean metallicity of $\langle \log Z/Z_\odot \rangle = 0.38$, corresponding to 2.4 $Z_\odot$. Components at more negative velocities ($v_{\rm LSR} < -100$ km s^{-1}) are likely associated with Complex C. These components show metal-poor properties in good agreement with previous mea-

[3]`https://github.com/Deech08/whampy`

surements of Complex C ($\log Z/Z_\odot \lesssim -0.5$; Collins et al. 2007; Fox et al. 2023), supporting the reliability of our modelling procedure. The ionization parameter of Complex K components spans $\log U = -4.5$ to -1.4, with a mean value of -2.95. This range is broader than the metallicity distribution, which is consistently metal-rich, and is consistent with the mean photoionization parameter $\langle \log U \rangle = -3.0^{+0.3}_{-0.4}$ reported for ionized IVCs and HVCs by Shull et al. (2009). We also note that the total electron column density constraint from pulsar dispersion measures is critical for determining both the metallicity and the ionization parameter, as demonstrated in Choi et al. (2024). Without this constraint, the fitting allows substantially higher electron columns, yielding correspondingly lower metallicities. Moreover, our N_e limit is conservative, as the pulsar dispersion measure includes contributions from all ionized gas along the sight line, including the Milky Way ISM, the warm ionized medium (Reynolds 1990), and any diffuse hot coronal gas, not only Complex K. The Complex K components, therefore, account for only a fraction of the total N_e, and the true upper limit on their electron column may be lower than the value applied here.

Figure 3.6 shows the hydrogen number density as a function of Hα intensity, colored by metallicity (top), and hydrogen number density as a function of metallicity, colored by Hα intensity (bottom), for all Complex K components. The systematic uncertainty on $n_{\rm H}$ arising from the unknown cloud distance is shown as error bars spanning $d = 0.2 - 4$ kpc. The metallicity is insensitive to this uncertainty because the distance enters only through the conversion from U to $n_{\rm H}$ and does not affect the fit. The super-solar population (right side of the dashed line in both panels) shows a tentative positive trend between Hα intensity and $n_{\rm H}$ (Spearman $\rho = 0.34$, $p = 0.19$), though it does not reach statistical significance at our sample size. We also find a positive correlation between $n_{\rm H}$ and metallicity (Spearman $\rho = 0.54$, $p = 0.03$), but caution that $\log U$ and $\log Z/Z_\odot$ are partially degenerate in photoionization fits when the H I column density is poorly constrained. For fixed metal ion column densities, lower metallicity solutions require higher total hydrogen columns

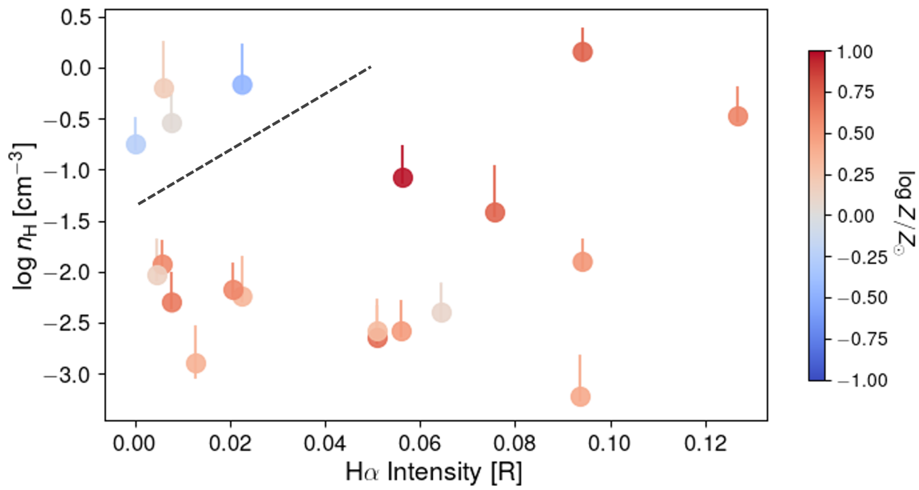

(a) Hα intensity and hydrogen number density

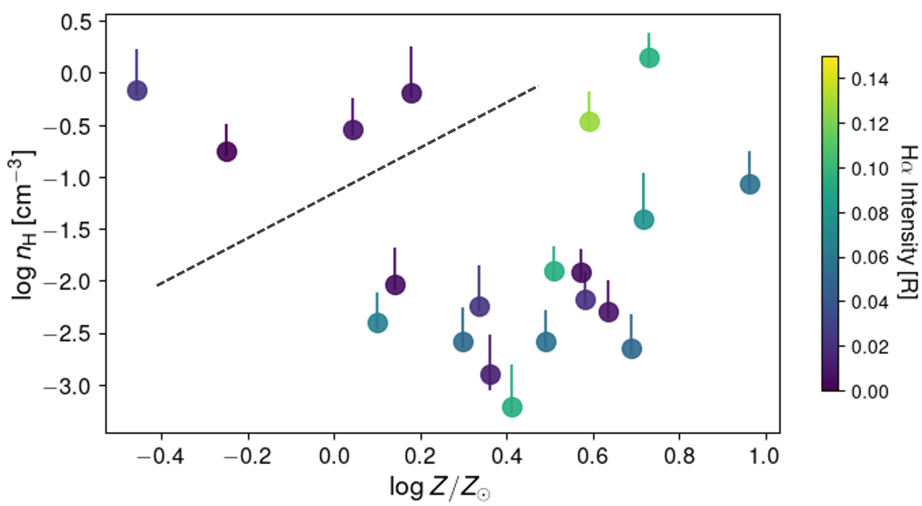

(b) Metallicity and hydrogen number density

Figure 3.6: Hydrogen number density as a function of Hα intensity, colored by metallicity (top), and hydrogen number density as a function of metallicity, colored by Hα intensity (bottom), for all Complex K components. The error bars in both panels reflect the systematic uncertainty on n_H from the unknown cloud distance ($d = 0.2$–4 kpc). The super-solar majority shows a tentative positive trend between Hα intensity and n_H in panel (a). The dashed line separates the super-solar majority from four lower metallicity components that have comparably high densities but notably low Hα intensities.

and correspondingly higher ionization parameters (Choi et al. 2024). Because $n_H \propto 1/U$ at fixed radiation field, this degeneracy can produce an artificial positive n_H-Z correlation. The pulsar-DM constraint mitigates this degeneracy by limiting the total electron column, but does not eliminate it entirely. We therefore do not interpret the $n_{\rm H}$-Z correlation as conclusive evidence for a physical density–metallicity relation within the super-solar population (Note: Our current sample of 20 Complex K components will be expanded to ~ 50 components with additional sight lines for which photoionization modelling is ongoing. The larger sample will provide the statistical power needed to assess whether the trends reported here are significant.)

Four components depart clearly from the super-solar majority (left side of the dashed line in Fig. 3.6). Two have sub-solar metallicities and two have near-solar metallicities that overlap with the lower end of the super-solar population, but all four share notably low Hα intensities despite inferred densities comparable to or exceeding those of the majority. This combination of high density and low Hα distinguishes them as a population, even where their metallicities alone would not. On the sky, all four lie toward the higher-longitude periphery of Complex K, outside the brightest Hα and H I emission (Fig. 3.4a). Their coherent spatial distribution further supports a physically distinct origin rather than random sight line variation. We discuss the interpretation of these components in Section 4.

6 Distance Constraint

6.1 Optical BHB Spectra

We obtain optical spectra of 6 BHB stars in the direction of Complex K at distances of 1–10 kpc to constrain the distance to Complex K via absorption-line bracketing (i.e., detection or non-detection of Ca II and/or Na I absorption). The targets are selected from the *Gaia* photometric BHB catalog (Culpan et al. 2021) and DESI DR1 (DESI Collaboration et al. 2026) Milky Way Survey BHB catalog (Byström et al. 2025). For the *Gaia* BHBs, distance estimates are based on parallax, and for DESI BHBs, their distances are estimated spectrophotometrically with typical error $\lesssim$ 10 %. We observe BHBs using the

ARCES high-resolution spectrograph ($R \sim 31{,}500$) on the Apache Point Observatory ARC 3.5 m telescope, which covers optical wavelengths from 3,200 to 10,000 Å, encompassing the Ca II H&K and Na I D lines. We reduce the data using the `aesop` IRAF pipeline (`https://github.com/bmorris3/aesop`) for basic image calibration, echelle aperture extraction, and wavelength calibration. The stellar continuum is normalized order-by-order using the IRAF `continuum` task with spline functions, verified by visual inspection. We measure radial velocity of BHBs using Ca II triplet at 8498.02, 8542.09, and 8662.14 Å and Hα and Hβ lines, especially when Ca II triplet is too weak.

A summary of the BHB targets and their measured properties is presented in Table 3.4. To estimate expected Ca II and Na I column densities from the HI4PI H I column densities, we use the empirical relations derived from Wakker & Mathis (2000).

$$\log N_{\rm CaII} = 0.22 \, \log N_{\rm HI} + 7.45, \tag{3.3}$$

$$\log N_{\rm NaI} = 0.84 \, \log N_{\rm HI} - 5. \tag{3.4}$$

Table 3.4: BHB targets for Complex K distance bracketing.

Name	Gaia DR3 ID	l	b	d	$v_{\rm LSR,\star}$	$\log N_{\rm HI}$	Ca II		Na I	
		(deg)	(deg)	(kpc)	(km s^{-1})	(cm^{-2})	pred	meas	pred	meas
BHB1	1274344563688693248	49.90	55.13	1.43±0.04	-182.9	18.29	11.47	10.53±2.33	10.37	10.93±0.63
BHB2	1284292734441501824[a]	46.56	66.93	2.09±0.09	-62.3	18.01	11.41	12.93±0.01	10.13	11.66±0.12
BHB3	1457549486075953024	55.24	75.04	2.12±0.10	+15.0	…	…	12.64±0.02	…	10.63±1.24
BHB4	4574762051442201472	49.15	33.21	2.44±0.07	-143.6	18.92	11.61	12.00±0.08	10.90	10.67±1.13
BHB5	1267083835574196864[a]	34.27	65.02	3.27±0.19	-63.0	19.36	11.71	12.82±0.01	11.27	11.38±0.23
BHB6	1287403050976262272	55.26	67.80	9.57±1.78	-42.0	…	…	11.89±0.10	…	…

Note. Distances are from *Gaia* parallax or DESI spectrophotometry (Byström et al. 2025; Culpan et al. 2021). Stellar radial velocities are converted to the LSR frame. N_{HI} is the HI4PI column density integrated over the Complex K velocity range; targets without an H I detection at Complex K velocities are marked with "$\cdots$". "pred" columns give predicted Ca II and Na I column densities from the empirical relations of Wakker & Mathis (2000). "meas" columns give measured column densities (AODM) integrated over -95 to $-60\ \mathrm{km\,s^{-1}}$. All column densities are in units of $\log(\mathrm{cm^{-2}})$.

[a] Stellar velocity falls within the Complex K velocity range (-95 to $-60\ \mathrm{km\,s^{-1}}$); measured column densities are contaminated by stellar absorption.

6.2 *Preliminary Distance Bracket*

A major limitation of our absorption-line bracketing is that two of the six targets have stellar LSR velocities that fall within the Complex K velocity range (-95 to -60 km s^{-1}), the $d = 2.1$ kpc BHB2 ($v_{\mathrm{LSR},\star} = -62.3\ \mathrm{km\,s^{-1}}$) and the $d = 3.3$ kpc BHB5 ($v_{\mathrm{LSR},\star} = -63.0\ \mathrm{km\,s^{-1}}$). For these targets, absorption at Complex K velocities is blended with stellar features, preventing unambiguous identification. The remaining four targets have stellar velocities well separated from the Complex K range.

Among the unblended targets with H I detections at Complex K velocities, the $d = 1.4$ kpc BHB ($v_{\mathrm{LSR},\star} = -182.9$ km s^{-1}) shows marginal Ca II absorption at Complex K velocities ($\log N_{\mathrm{Ca\,II}} \approx 10.5$), well below the predicted value of 11.47 from the Wakker & Mathis (2000) relation, consistent with little or no Complex K gas along this sight line. The $d = 2.4$ kpc BHB ($v_{\mathrm{LSR},\star} = -143.6$ km s^{-1}) shows moderate Ca II absorption ($\log N_{\mathrm{Ca\,II}} \approx 12.0$), comparable to the predicted value of 11.61, suggesting the presence of Complex K gas in front of this star. The two remaining unblended targets ($d = 2.1$ and 9.6 kpc) lack H I detections at Complex K velocities toward their sight lines, limiting their utility for the bracketing.

If confirmed, these results would place the near side of Complex K at a distance of $d \gtrsim 1.4$ kpc, with gas detected in front of the $d = 2.4$ kpc target, consistent with the upper limit of $d < 3.6$ kpc reported by Lehner et al. (2022). We note, however, that Complex K

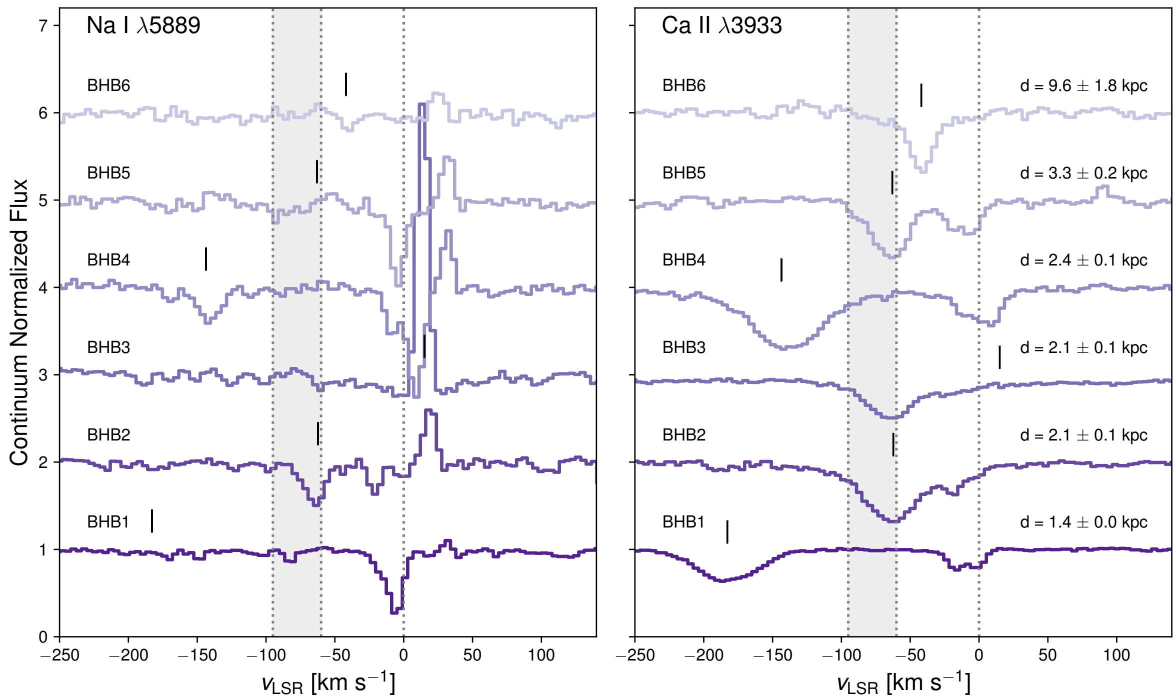

Figure 3.7: ARCES spectra of six BHB stars in the direction of Complex K, showing the spectral regions around Na I D (left) and Ca II K (right). The shaded region marks the Complex K velocity range (-95 to -60 km s^{-1}). Vertical arrows indicate the stellar radial velocity for each target. Targets are ordered by distance from top to bottom.

subtends $\sim 40°$ on the sky, corresponding to a physical extent of ~ 1.4 kpc at $d = 2$ kpc. If the depth along the line of sight is comparable, the complex may span a range of distances rather than residing at a single well-defined distance. Given the large angular extent of Complex K, this distance bracket applies only to the specific sight lines observed and may not be representative of the complex as a whole. A comprehensive picture of the three-dimensional structure of Complex K will require distance brackets across its full spatial extent, using a larger sample of BHB stars whose radial velocities are well separated from the Complex K velocity range.

7 Discussion

7.1 Fountain Origin of Complex K

The super-solar gas-phase metallicity of the majority of Complex K components ($\langle \log Z/Z_\odot \rangle = 0.38$, corresponding to $2.4\ Z_\odot$) strongly supports a Galactic disk origin. Gas accreted from the IGM or stripped from metal-poor satellite galaxies would be expected to have sub-solar metallicities (e.g., Fox et al. 2013; Lehner et al. 2013; Wakker et al. 1999), whereas gas ejected from the star-forming disk by feedback carries the near- or super-solar metallicity of the local ISM (Bregman 1980; Fraternali 2017; Shapiro & Field 1976). The super-solar central tendency we measure is consistent with the near-solar metallicity bracket reported for Complex K and other northern IVCs by Wakker (2001), and sharpens it with a larger sight line sample, joint photoionization modelling, and an independent electron column density constraint from pulsar dispersion measures.

To test whether the kinematics of Complex K are consistent with a fountain flow, we solve for the vertical velocity v_z of each component by placing a particle at the observed (l, b) and an assumed distance d, adopting cylindrical velocity components (v_R, v_ϕ, v_z). We test $v_\phi = 200$–$240\ \mathrm{km\ s^{-1}}$ and present the $v_\phi = 220\ \mathrm{km\ s^{-1}}$, $v_R = 0\ \mathrm{km\ s^{-1}}$ case as fiducial in Fig. 3.8 for assumed distances of $d = 2$ kpc, with $v_R = \pm30\ \mathrm{km\ s^{-1}}$ shown as error bars. These values are consistent with the kinematics of Milky Way IVCs and HVCs (Marasco et al. 2022) and with fountain-particle models (Fraternali & Binney 2008). The qualitative results are insensitive to the assumed v_ϕ. For each Complex K component, we solve for the vertical velocity v_z required to reproduce the observed v_{LSR}. The inferred vertical velocities span $v_z \approx -186$ to $-60\ \mathrm{km\ s^{-1}}$, with all components consistent with infalling gas. These values fall within the range expected from ballistic fountain models (Fraternali & Binney 2006; Shapiro & Field 1976) and more detailed models that incorporate drag and condensation (Fraternali & Binney 2008; Marinacci et al. 2010).

Within the super-solar population, there is a suggestive trend in which the most metal-rich components have the least negative v_z, while components with lower but still super-solar metallicities have more negative v_z (Fig. 3.8). A Spearman test yields $\rho = 0.48$ ($p = 0.06$) at $d = 1$ kpc, $\rho = 0.41$ ($p = 0.12$) at $d = 2$ kpc, and $\rho = 0.40$ ($p = 0.13$) at $d = 3$ kpc. The trend does not reach formal statistical significance ($p < 0.05$) at any assumed distance, but the consistent sign and magnitude of the correlation across all three cases sug-

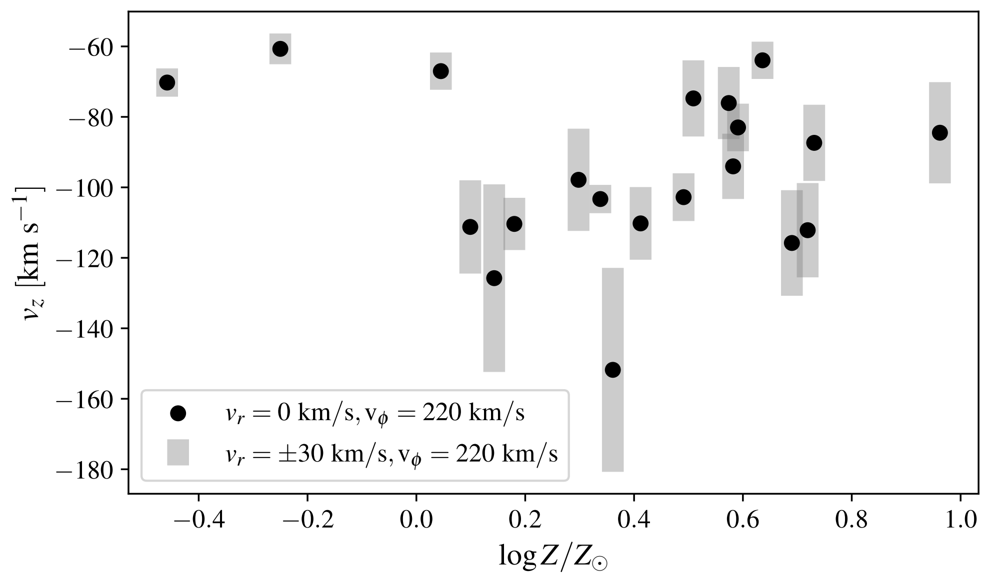

Figure 3.8: Vertical velocity v_z as a function of metallicity for all Complex K components, assuming $v_\phi = 220$ km s^{-1} and distances of 2 kpc. We show $v_r = 0$ km s^{-1} case (points) with error bars that show the range spanned by $v_r = \pm 30$ km s^{-1}. All components have negative v_z, consistent with infalling gas. The super-solar majority shows a tentative trend in which higher metallicity components have less negative v_z.

gest it is not an artifact of the distance assumption. A larger sample will be needed to confirm or rule out this trend. If physical, it can be understood as a mixing sequence in the fountain-driven condensation picture. In the fountain-driven condensation picture, gas ejected from the disk triggers cooling of the surrounding metal-poor corona, progressively gaining mass from the condensed halo gas as it travels through its trajectory (e.g., Fraternali 2017). Since all components have negative v_z (infalling), more negative v_z corresponds to gas that is further along in its descent and has had more time to accumulate metal-poor coronal material, diluting its metallicity. The observed trend, in which the most metal-rich components have the least negative v_z and the lower-metallicity (but still super-solar) components have more negative v_z, is qualitatively consistent with this expectation. While the absolute metallicity values may shift with future depletion corrections, the relative differences between components are more robust.

Verschuur et al. (2024) have recently proposed an alternative interpretation in which

Complex K traces the near-side hemisphere of one or more expanding shells driven by supernovae ($\sim 3 \times 10^5$ yr ago). These two pictures are not strictly mutually exclusive, as galactic fountains are themselves driven by supernova feedback in modern simulations (e.g., Kim & Ostriker 2018; Marasco et al. 2012), but they differ in the predicted spatial coherence and chemical history of the gas. Our data do not definitively distinguish between the two scenarios, and kinematic modelling incorporating both fountain trajectories and shell geometries is deferred to future work.

7.2 Fountain-Driven Halo Gas Condensation

In Section 7.1, we identified a suggestive mixing sequence within the super-solar majority, in which metallicity decreases with increasingly negative v_z. This is consistent with fountain gas progressively gaining metal-poor mass from coronal condensation along its trajectory. Three components, however, depart from this sequence. Despite their low metallicities ($\log Z/Z_\odot = -0.5$ to 0), they have among the least negative v_z in the sample ($v_z \sim -70$ to -60 km s^{-1}). If these components were simply the most extreme end of the same mixing sequence, they should have the most negative v_z, having traveled the longest and accumulated the most halo material. Their slow infall instead suggests a different origin. In the fountain-driven condensation scenario, cold fountain gas and hot coronal gas mix efficiently in a turbulent wake behind the cloud, dramatically reducing the cooling time of the hot gas and triggering condensation (Armillotta et al. 2016; Marinacci et al. 2010). The newly condensed material forms from the corona and is expected to retain its low metallicity and low velocity, as it has not yet been accelerated by the fountain flow. The properties of our three metal-poor components, sub-solar to near-solar metallicity and slow infall, are qualitatively consistent with recently condensed coronal gas at the cloud-halo interface.

Several additional properties of these components support the condensation interpretation. Their inferred hydrogen number densities are comparable to or exceed those of the super-solar majority, despite their lower metallicities, as discussed in Section 5 (Fig. 3.6). This high density is consistent with recently condensed gas. As coronal material cools from $T \sim 10^6$ K to $T \sim 10^4$ K, it compresses to reach pressure equilibrium with the surrounding medium (Fielding et al. 2020; Gronke & Oh 2018 2020). Their Hα intensities are also notably low despite their high densities, suggesting that they are not strongly photoionized by the disk radiation field and may instead trace a recently condensed phase that has not yet been illuminated. Furthermore, all three lie toward the higher-longitude periphery of Complex K, outside the brightest Hα and H I emission (Fig. 3.4a), consistent with condensation occurring preferentially at the cloud-halo interface where mixing between fountain gas and coronal gas is most active (Begelman & Fabian 1990; Slavin et al. 1993).

The fountain-driven condensation (Armillotta et al. 2016; Fraternali 2017; Marinacci et al. 2011) predicts that metal-rich gas ejected from the disk triggers the cooling of the surrounding metal-poor corona through turbulent mixing in the cloud wake. The condensed gas is expected to have intermediate or sub-solar metallicity (inherited from the corona), high density (cooled and compressed relative to the corona), and a kinematic lag relative to the fountain gas (not yet accelerated). All three properties are exhibited by our metal-poor components. While the fountain mechanism in the Milky Way has been established globally through kinematic modelling (Marasco et al. 2012 2022), our results trace the fountain process within Complex K itself, resolving the metallicity evolution along the flow and identifying condensed coronal gas at the cloud boundary.

Under the alternative SN-shell interpretation (Verschuur et al. 2024), the metal-poor components could trace halo gas swept up at the shell front during expansion into the lower halo. The coherent spatial distribution of these components on one side of Complex K is consistent with a directional shell front, although the small sample size prevents a strong statistical claim. The two scenarios also predict different ionization physics. Fountain-driven condensation produces gas that cools radiatively and is photoionized by the ambient radiation field, whereas a shell front would shock-ionize the swept-up gas. Our photoionization modelling cannot distinguish between these cases, as the equilibrium CLOUDY models do not account for non-equilibrium shock ionization. Distinguishing between the two scenarios will require a larger sample and diagnostics sensitive to the ionization mechanism.

7.3 Mass Budget and Infall Timescale

The metal-rich majority of Complex K establishes it as fountain gas returning to the Galactic disk. A natural question is how much mass this return flow carries, on what timescale it reaches the disk, and what implications this has for the chemical evolution of the Milky Way. We estimate the total gas mass of Complex K and its infall rate, and place these in the context of the Galactic baryon cycle.

We estimate the gas mass of Complex K as:

$$M = \mu \, m_p \, d^2 \, \Omega \, \langle N \rangle, \tag{3.5}$$

where $\mu = 1.33$ accounts for helium, m_p is the proton mass, d is the distance to the complex, Ω is the solid angle subtended on the sky, and $\langle N_{\rm HI} \rangle$ is the mean column density over the cloud extent. For the neutral component, we use the HI4PI 21 cm data (HI4PI Collaboration et al. 2016) integrated over Complex K velocity range. With a threshold of $N_{\rm HI} = 10^{18}$ cm^{-2}, $\Omega_{\rm neutral} \approx 564$ deg^2 and $\langle N_{\rm HI} \rangle = 5.7 \times 10^{18}$ cm^{-2}. We obtain $M_{\rm neutral} \approx 9.4 \times 10^4 \, (d/3\,{\rm kpc})^2$ M$_\odot$. This is comparable to the previous estimate of $M_{\rm HI} < 7.5 \times 10^5 \, M_\odot$ based on a distance upper limit of $d < 6.8$ kpc (Wakker 2001); scaling our estimate to the same distance gives $M_{\rm neutral} \approx 4.8 \times 10^5 \, M_\odot$.

The ionized envelope of Complex K extends beyond the H I body of the cloud, as traced by our sight lines. We estimate the ionized gas mass using the ionized hydrogen column density $\langle N_{\rm HII} \rangle = 9.7 \times 10^{18}$ cm^{-2} from our photoionization fits over a larger solid angle of

$\Omega_{\rm ion} \approx 1500\ {\rm deg}^2$. It yields $M_{\rm ion} \approx 4.2 \times 10^5\ (d/3\ {\rm kpc})^2\ {\rm M}_\odot$. The total gas mass is $M_{\rm tot} = M_{\rm neutral} + M_{\rm ion} \approx 5.1 \times 10^5\ (d/3\ {\rm kpc})^2\ {\rm M}_\odot$, with the ionized component dominating the mass budget. We note that the neutral mass derived from the photoionization model $N_{\rm HI}$ values over the ionized gas extent is comparable with the neutral mass derived using H I 21 cm map, having $M_{\rm neutral,model} \approx 8.5 \times 10^4\ (d/3\ {\rm kpc})^2\ {\rm M}_\odot$. The total mass is consistent with the expected fountain gas mass ($\sim 10^5\ M_\odot$) driven by supernovae from a single OB association (~ 100 supernovae) in a Milky Way-like galaxy (Melioli et al. 2008).

The infall timescale for Complex K can be estimated as $t_{\rm infall} = z/|v_z|$, where $|v_z|$ is the mean vertical infall velocity and z is the Galactic height. Adopting $|v_z| \approx 100\ {\rm km\ s}^{-1}$ and $z \approx 2$ kpc, we obtain $t_{\rm infall} \sim 20$ Myr. The full fountain recycling timescale, which includes both the ascending and descending phases, is roughly twice this value ($t_{\rm recycle} \sim 40$ Myr), consistent with the $\sim$ 50–100 Myr fountain cycle timescales found in models (Fraternali 2017). The corresponding mass inflow rate is $\dot{M} \approx M_{\rm total}/t_{\rm infall} \approx 0.02\ M_\odot\ {\rm yr}^{-1}$. For comparison, Fox et al. (2019) estimated the total HVC mass inflow rate to be $\dot{M}_{\rm in} \gtrsim 0.53 \pm 0.23\,(d/12\ {\rm kpc})({\rm Z}/0.2\ {\rm Z}_\odot)^{-1}\ {\rm M}_\odot\ {\rm yr}^{-1}$, noting that contributions from IVCs would increase this estimate. Complex K, as an IVC, represents one such additional contribution to the Milky Way's total gas inflow budget.

Our results can be placed in the broader context of Galactic chemical evolution. Classical models of the Milky Way disk (e.g., Chiappini et al. 1997; Spitoni et al. 2019) predict that the ISM metallicity rises continuously with time as ongoing star formation enriches the gas, with the radial gradient arising from inside-out disk growth. However, Johnson et al. (2025) have recently demonstrated that stellar metallicities in the Milky Way disk are approximately age-independent up to ~ 9 Gyr at fixed Galactocentric radius, favoring an equilibrium scenario in which metal production by star formation is balanced by losses to outflows and star formation itself, and by dilution from metal-poor accretion. Fraternali et al. (2015) demonstrated that fountain-driven condensation of the Galactic corona provides the low-metallicity gas that such models require, using Complex C ($Z \sim 0.1-0.3\ Z_\odot$).

Complex K traces the complementary regime. Gas closer to the disk that retains the super-solar metallicity of the ISM from which it was launched, with condensed coronal material appearing at the cloud boundary. The returned gas is, therefore, not uniformly metal-poor but spans a range of metallicities depending on the accumulated coronal fraction. If the fountain-driven origin established here for Complex K is representative of IVCs generally, as suggested by their near-solar metallicities and infalling kinematics (Marasco et al. 2022; Wakker 2001), the cumulative fountain-driven accretion would enter at higher metallicity than the zero-metallicity infall assumed in most GCE models, which Johnson (2025) showed raises the equilibrium abundance and slightly flattens the radial gradient for accretion metallicities of $[\mathrm{O/H}]_{\mathrm{CGM}} \approx -0.7$; the effect would be stronger for the higher metallicities measured here. Quantifying this effect requires incorporating fountain recycling self-consistently into chemical evolution models, for which resolved measurements of fountain cloud metallicities, masses, and kinematics, such as those presented here, provide direct empirical inputs.

8 Summary

Complex K is a well-resolved intermediate-velocity cloud ($-95 \leq v_{\mathrm{LSR}} \leq -60\ \mathrm{km\ s^{-1}}$) in the northern Galactic halo ($l \approx 30 - 70°$, $b \approx 25 - 70°$), spanning $\sim 40°$ on the sky with near-solar to super-solar metallicity reported in previous studies (Choi et al. 2024; Wakker 2001). Its large angular extent, infalling kinematics, and metal-rich composition make it an ideal target for resolving the internal structure of a Galactic fountain flow. We use HST/COS UV absorption spectroscopy toward 20 background QSOs and 7 halo stars. We identify absorption components from multiple ionized metal species (Si II, Fe II, S II, C IV, among others) and fit Voigt profiles using Hamiltonian Monte Carlo sampling. We then perform joint Bayesian photoionization modelling with CLOUDY, parameterized by N_{HI}, metallicity Z, ionization parameter U, with priors informed by HI4PI 21 cm column densities and an independent electron column density constraint derived from ATNF pulsar dispersion measures. We obtain simultaneous constraints on the metallicity, ionization state, and hydrogen density for 20 Complex K velocity components. Our main findings are:

1. The majority of Complex K components (16/20) have super-solar gas-phase metallicities, with a mean of $\langle \log(Z/Z_\odot) \rangle = 0.38$ $(2.4\,Z_\odot)$. This supports a Galactic disk origin via the fountain mechanism. The absolute metallicity values are subject to systematic uncertainties from the absence of dust depletion corrections and the $Z - U$ degeneracy in photoionization fitting.

2. A kinematic analysis assuming cylindrical velocities (v_R, v_ϕ, v_z) yields vertical velocities of $v_z \approx -186$ to -60 km s^{-1}, with all components consistent with infalling gas. Within the super-solar population, there is a suggestive trend in which higher-metallicity components have less negative v_z (Spearman $\rho = 0.48$, $p = 0.06$ at d = 1 kpc), consistent with progressive dilution by metal-poor coronal gas along the fountain trajectory. The trend persists across assumed distances of $d = 1 - 3$ kpc.

3. Three components depart from the super-solar majority, with sub-solar to near-solar metallicities, slow infall ($v_z \sim -70$ to -60 km s^{-1}), high densities, low Hα intensities, and peripheral spatial locations. These properties are consistent with recently condensed coronal gas at the cloud-halo interface, as predicted by fountain-driven condensation models.

4. Using HI4PI 21 cm data and our photoionization fits, we estimate a total gas mass of $M_{\rm tot} \approx 5.1 \times 10^5\ (d/3\ {\rm kpc})^2\ {\rm M}_\odot$, with the ionized component dominating the mass budget. The infall timescale is $t_{\rm infall} \sim 20$ Myr, corresponding to a mass inflow rate of $\dot{M} \approx 0.01\ M_\odot\ {\rm yr}^{-1}$.

5. Optical spectra of six BHB stars in the direction of Complex K provide a tentative distance bracket of $d \gtrsim 1.4$ kpc. With the current upper limit of $d < 3.6$ kpc (Lehner

et al. 2022), we suggest a tighter distance limit to Complex K. The large angular extent of Complex K ($\sim 40°$) means this bracket may not apply to the complex as a whole.

Chapter 4

An Ionized Extension of the Magellanic Stream

Portions of this chapter were originally published in collaboration with Jessica K. Werk, Kirill Tchernyshyov, Mary E. Putman, Yong Zheng, J. E. G. Peek, Hannah Bish, and David Schiminovich in the December 2025 edition of the Astrophysical Journal Letters (Choi et al. 2025, ApJL, Vol. 995, 24; 2025 © American Astronomical Society, DOI: 10.3847/2041-8213/ae2308), and are reproduced below with the permission of the American Astronomical Society.

Summary

The Magellanic Stream (MS) is a vast gaseous structure in the Milky Way halo, containing most of its mass in ionized form and tracing the interaction between the Large and Small Magellanic Clouds and the Galaxy. Using HST/COS G160M spectra from the Plane Quasar Survey, we detect C IV absorbers likely associated with the MS, extending to the northern side of the Galactic plane, approximately 60° beyond its previously known ionized extent. These absorbers exhibit position and kinematic alignment and show consistent ionization trends with previously studied MS sight lines. The non-detection of low ions such as Al II and Si II, and the detection of C IV (and Si IV in some sight lines), indicates a highly ionized gas phase. The observed Si IV/C IV column density ratios suggest a gas temperature of $T \sim 10^{5.3}$ K and favor collisional ionization over photoionization. We estimate the newly detected extension increases the previous ionized gas mass of the MS, and its coherent kinematics suggest that it was stripped within the past few hundred Myr and has not yet mixed with the Milky Way halo. The existence of highly-ionized MS gas at a location above the Galactic Plane may constrain the orbital direction of the Magellanic Clouds.

1 Introduction

The Magellanic Stream (MS; hereafter the Stream) is a trailing gaseous structure that traces the interaction of the Large and Small Magellanic Clouds (LMC and SMC; hereafter, the "Clouds") with the Milky Way (MW). Its full extent in H I 21 cm emission spans approximately 150 degrees across the southern Galactic sky, with a width of 10 degrees (Mathewson et al. 1974; Nidever et al. 2010; Putman et al. 2003b). The Stream also represents the most massive neutral high-velocity cloud (HVC) complex in the MW halo (Putman et al. 2012), with a H I mass of $M_{\rm HI} \approx 2.7 \times 10^8\ M_\odot$ (Brüns et al. 2005). The Stream represents the single most massive and extended gaseous structure in the MW halo, serves as a testbed for studying the impact of satellite galaxy interactions, and is a crucial probe of coherent gaseous circumgalactic structures throughout the universe.

Observational studies of the neutral Stream, using deep H I surveys and UV absorption spectroscopy, have revealed that the Stream consists of two filaments with distinct morphologies, kinematics (Nidever et al. 2008; Putman et al. 2003b), and metallicities (Fox et al. 2013; Richter et al. 2013). These findings suggest that the Stream contains material stripped from both the Clouds; however, its detailed formation history and nature are not yet fully understood. As the position-velocity structure of the Stream serves as a key observational constraint on the Clouds' orbital history and the nature of its formation, many theoretical models have focused on reproducing it. The Stream was traditionally explained by tidal stripping of material from the Clouds during multiple passages around the MW (e.g., Lin & Lynden-Bell 1977), with later models including the LMC-SMC interactions (i.e., second passage; Diaz & Bekki 2012; Yoshizawa & Noguchi 2003). Precise *Hubble Space Telescope* proper motion measurements of the Clouds posed a different view of their orbital history, suggesting that they may have completed only one orbit or may even be on their first passage around the MW (Kallivayalil et al. 2006 2013). This led to the development of first-passage models, in which the Stream forms primarily through tidal interactions between the Clouds (Besla et al. 2010 2012).

Beyond its neutral gas component, the Stream also hosts a significant reservoir of ionized gas, which introduces additional complexity in understanding its formation and evolution. Fox et al. (2014) estimated the total ionized mass of the Stream to be $\sim 10^9\ M_\odot$, exceeding the neutral mass and extending more widely across the sky. This dominant mass in ionized gas is underestimated in tidal models (Besla et al. 2012; Diaz & Bekki 2012). As an alternative to tidal models, ram-pressure models have been suggested in which the Stream is formed via ram-pressure stripping of gas from the Clouds while they pass through the extended, gaseous MW halo (e.g., Hammer et al. 2015; Mastropietro et al. 2005). Wang et al. (2019) applied a ram-pressure plus direct collision model and reproduced the observed properties including the ionized and H I gas mass. Lucchini et al. (2020) proposed that the Magellanic corona, a warm, extended gas envelope surrounding the Clouds, plays a crucial role in the formation of the Stream, contributing a substantial fraction of its ionized gas. Recent UV detections provide some observational evidence of a $10^{5.5}$ K corona, however it is difficult to distinquish a corona from the ionized component of the Stream (Kim et al. 2024; Krishnarao et al. 2022).

The ionization and kinematic structure of the ionized gas in the Stream are crucial for understanding the physical processes that shapes its evolution. UV absorption observations show that the ionization fraction increases toward the trailing end of the Stream (Kim et al. 2024). The underlying ionization mechanisms remain uncertain (Putman et al. 2003a), with potential sources including shock ionization as the Stream travels through the MW halo (Bland-Hawthorn et al. 2007; Weiner & Williams 1996), a recent Seyfert flare from the Galactic Center (Bland-Hawthorn et al. 2019), and photoionization by stellar radiation from the MW and Clouds (Barger et al. 2017; Bland-Hawthorn & Maloney 1999). In addition to the ionization structure, the velocity structure of the ionized gas provides a useful tracer of the Stream's interaction with the CGM of the MW and LMC, as the more diffuse ionized component is more sensitive to hydrodynamic drag (Lucchini 2024; Zhu et al. 2024) and likely traces conductive or turbulent boundary layers surrounding the Stream (Bustard & Gronke 2022; Fox et al. 2005).

In this Letter, we report the serendipitous discovery of an ionized extension of the Stream reaching above the Galactic plane, about 60 degrees longer than the previously detected ionized gas. This ionized component is traced by C IV absorption in QSO sight lines near the Galactic plane. The QSOs were selected as part of the Plane Quasar Survey (PQS; Werk et al. 2024), which was originally designed to probe gas structures near the MW's disk unrelated to the Stream. From the observations with the *Hubble Space Telescope* (HST)/Cosmic Origin Spectrograph (COS), we detect C IV absorbers with kinematics consistent with those of the Stream up to the Galactic latitude of $b \sim 27°$. We describe the HST/COS observation and data analysis in Section 2. In Section 3, we discuss the association of newly detected C IV absorbers with the Stream, presenting their velocity structure, ionization states, and estimated mass. We discuss their origin and the physical implications of our discovery in Section 4.

Throughout this manuscript, all velocities are reported in the local standard of rest (LSR) frame, denoted as $v_{\rm LSR}$. We adopt the barycentric solar motion relative to the LSR as $(U, V, W) = (11.1, 12.24, 7.25)$ km s^{-1} (Schönrich et al. 2010). The LSR frame is commonly used in studies of HVCs, enabling direct comparison with previous observations and models of the Stream and other halo gas structures.

2 Observation & Data Analysis

2.1 HST/COS G160M Observation

We originally proposed observations of the PQS targets to investigate the extent of a rotating, extended, ionized disk of the Milky Way, with selected QSO sight lines from the PQS at $l \approx 90°$ and $\approx 270°$ at low Galactic latitudes of $|b| < 30°$ (Fig. 4.1a). We observed the QSOs and obtained their FUV spectra with the HST/COS G160M grating with a central wavelength of 1577 Å (Program ID: 16679). Exposure times were optimized to achieve a signal-to-noise ratio (S/N) $\sim$ 11-15 per resolution element across 1400-1550 Å. The COS G160M grating provides a wavelength coverage of 1360-1775 Å, covering absorption lines from various metal ions, including low ions (e.g., Si IIλ1526, Al IIλ1670) and intermediate ions (i.e., Si IV$\lambda\lambda$1393, 1402, C IV$\lambda\lambda$1548, 1550). A characteristic spectral resolution of the G160M grating at lifetime position 6 (LP6) is $R \sim 10,000$.

We applied `coadd_x1d` routine developed by Danforth et al. (2010 2016) to the CALCOS-generated `x1d.fits` files. It combines all the exposures and treats the error arrays properly based on Poisson statistics. We combined the exposures with a weight on S/N and binned the data by three spectral pixels. The resulting science-grade spectra have an FWHM ≈ 18 km s^{-1}.

A useful coordinate system to examine the structure associated with the Stream is the MS coordinate frame defined by Nidever et al. (2008). We show the locations of our targeted sight lines in MS coordinates, $(L_{\rm MS}, B_{\rm MS})$, in Fig. 4.1b. In addition to our COS G160M observations, we searched the Mikulski Archive for Space Telescopes (MAST) for FUV QSO spectra within $-180° < L_{\rm MS} < -150°$ and $|B_{\rm MS}| < 30°$, and obtained an HST/STIS E140M spectrum of H1821+643 (Program ID: 8165). Table 4.1 contains a summary of our QSO samples. The specific observations analyzed in this article can be accessed via [doi: 10.17909/78fe-ne69]https://doi.org/10.17909/78fe-ne69.

Table 4.1: Data Summary

QSO Name	l (deg)	b (deg)	$L_{\rm MS}$ (deg)	$B_{\rm MS}$ (deg)	Instrument	$\log N_{\rm CIV}$ (cm^{-2})	$b_{\rm CIV}$ (km s^{-1})	$v_{\rm LSR,CIV}$ (km s^{-1})
J2206+2757	84.0	-22.2	-123.0	-10.4	COS/G160M	13.78 ± 0.04	45.0 ± 5.7	-345.8 ± 3.9
J2215+2902	86.4	-22.5	-123.1	-8.2	COS/G160M	13.50 ± 0.09	30.0 ± 8.9	-388.8 ± 5.8
J2251+3419	96.5	-22.3	-124.9	1.0	COS/G160M	13.73 ± 0.05	41.1 ± 6.9	-412.7 ± 4.8
J2203+3145	86.0	-18.8	-126.7	-9.3	COS/G160M	13.89 ± 0.03	48.0 ± 4.2	-383.2 ± 2.9

Continued on next page

Table 4.1 – continued

QSO Name	l (deg)	b (deg)	$L_{\rm MS}$ (deg)	$B_{\rm MS}$ (deg)	Instrument	$\log N_{\rm CIV}$ (cm^{-2})	$b_{\rm CIV}$ (km s^{-1})	$v_{\rm LSR,CIV}$ (km s^{-1})
J2141+3151	82.4	-15.7	-129.1	-13.3	COS/G160M	14.16 ± 0.04	53.6 ± 5.8	-343.7 ± 4.1
J2109+3532	80.3	-8.4	-136.1	-16.7	COS/G160M	13.90 ± 0.07	30.0 ± 6.3	-321.8 ± 4.5
J1938+5408	86.4	15.3	-161.3	-13.6	COS/G160M	13.37 ± 0.03	25.3 ± 3.0	-273.9 ± 1.9
J1858+4850	78.8	19.1	-164.9	-21.0	COS/G160M	13.35 ± 0.09	11.3 ± 6.1	-265.4 ± 3.2
J1939+7007	102.0	21.5	-169.0	0.5	COS/G160M	13.02 ± 0.14	10.0 ± 10.3	-247.8 ± 5.1
H1821+643	94.0	27.4	-174.1	-7.4	STIS/E140M	13.31 ± 0.04	6.6 ± 0.9	-216.2 ± 0.6

Properties of the targeted QSO sight lines, including their names, Galactic coordinates (l, b), MS coordinates ($L_{\rm MS}$, $B_{\rm MS}$), and observed instruments. The best Voigt profile fitting parameters to the C IV MS absorbers, C IV column density ($N_{\rm CIV}$), b-parameter, and velocity centroid in the LSR, are also presented.

2.2 *Data Analysis*

We normalize the continuum of all spectra using `lt_continuumfit`, a Python tool in the open-source package `linetools` (Prochaska et al. 2017a). We identify all the absorption components in LSR velocity space within $|v_{\rm LSR}| < 500$ km s^{-1}. The LSR velocity window is chosen to detect absorption components associated with the Stream, of which known LSR velocity of neutral gas spans $|v_{\rm LSR}| \lesssim 450$ km s^{-1}, as well as with the MW ISM and other HVCs. We use the `pyigm IGMGuesses` (Prochaska et al. 2017) to identify components by eye using offsets of velocity centroids. We then jointly fit Voigt profiles to every absorption component in the velocity window using the public package `veeper`[1]. We present the best-fit Voigt profile parameters, ion column density ($N_{\rm ion}$), Doppler-b parameter, and velocity centroid ($v_{\rm LSR}$), for all the sight lines and all the detected metal ions in Table **??** in Appendix 6.

[1]The original version of `veeper`: `https://github.com/jnburchett/veeper`. In this work, we use a custom version (`https://github.com/mattcwilde/veeper`).

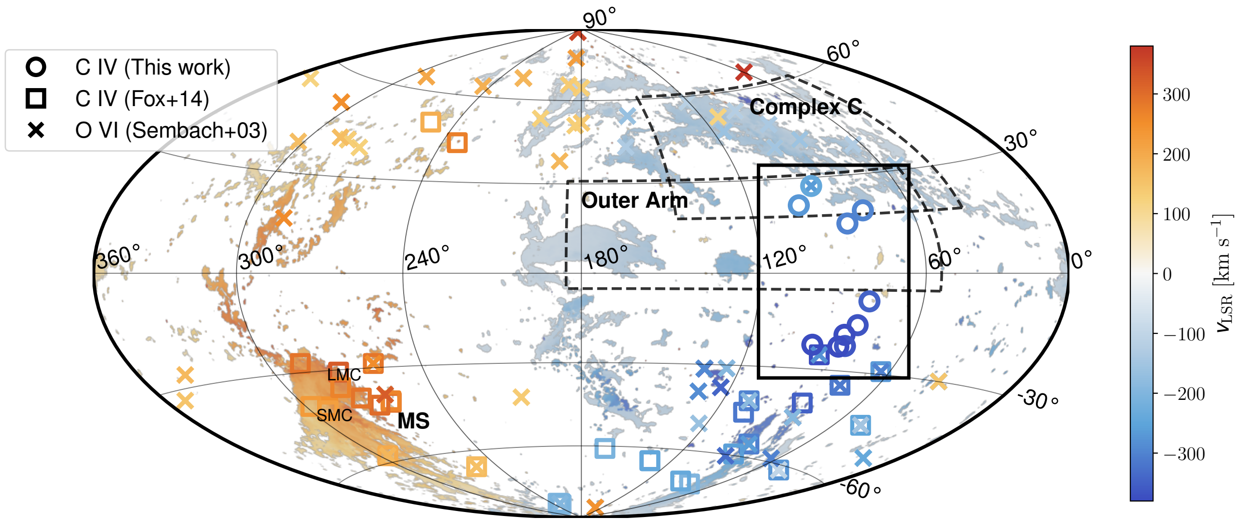

(a) The location of high-ion absorbers near the Stream in Galactic coordinates.

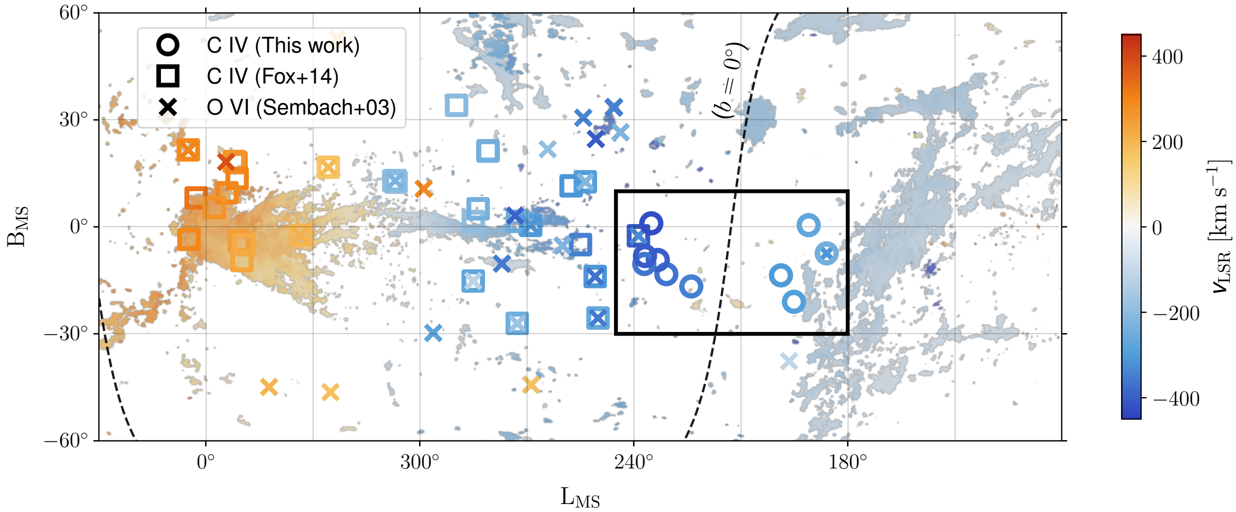

(b) The location of high-ion absorbers near the Stream in MS coordinates.

Figure 4.1: The location of high-ion absorbers near the Stream in (a, top panel) Galactic coordinates and (b, bottom panel) MS coordinates. In this work, we detect C IV absorbers (circles), extending to the Northern sky (Galactic latitude of $b \sim 30°$). We also include C IV (squares; Fox et al. 2014) and O VI (x markers; Sembach et al. 2003) absorbers from previous studies. The LSR velocity of the absorbers is color-coded. The all-sky H I map from the HI4PI survey (Westmeier 2018) is shown with the same velocity color scale.

3 Results

In Fig. 4.2, we present the FUV spectra with best-fit Voigt profiles for Si IIλ1527 (left), Si IVλ1394 (center), and C IVλ1548 (right). The Voigt profiles for all absorption compo-

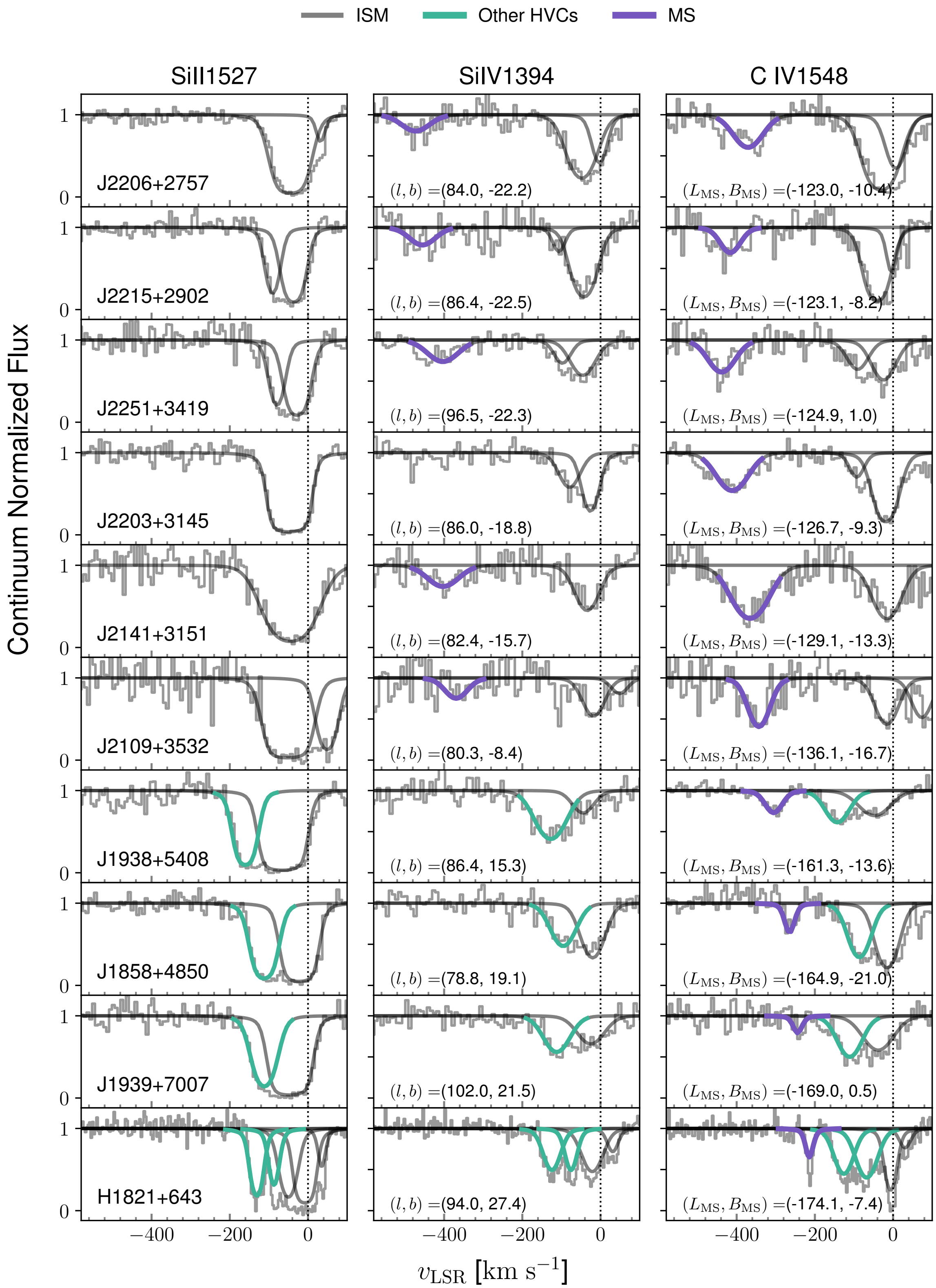

Figure 4.2: UV spectra and fitted Voigt profiles for Si II λ1527 (left), Si IV λ1394 (center), and C IV λ1548 (right) absorptions in the QSO sight lines. The components associated with the MS are shown in purple. These components have distinct velocity offsets from other HVCs, such as Complex C (green), and are not detected in low ions like Si II.

nents within $|v_{\rm LSR}| < 500~\rm km~s^{-1}$ are shown in black, while components associated with the Stream are highlighted in purple. Hereafter, we refer to these components as "MS absorbers". Other high-velocity absorption features associated with known structures are shown in green. We detect C IV MS absorbers in 10 sight lines. No corresponding Si II$\lambda1527$ absorption is detected, nor is absorption from other low-ion species such as Al II$\lambda1670$ (Table 4.2). In 5 sight lines with relatively higher C IV column densities, Si IV is also detected. The detection of only intermediate ions, particularly C IV, implies that the gas in this region is highly ionized.

3.1 C IV Absorbers Associated with the Stream

We briefly summarize the main arguments supporting the association of the detected C IV absorbers with the Stream:

- **Kinematic alignment with Stream predictions.** Velocity centroids align with the velocity gradient of the Stream derived from H I gas at $L_{\rm MS} \gtrsim -150°$ (Nidever et al. 2010), while our MS absorbers extend further to $L_{\rm MS} \sim -180°$ (Fig. 4.3).
- **Consistent ionization trend with known Stream sight lines.** Column density ratios of Si IV/C IV are consistent with those found in sight lines near the traditional end of the Stream, following a similar trend with MS latitude (Fig. 4.4).
- **h Distinct from known Galactic H I structures in the disk and halo.** The absorbers differ from Complex C and the Outer Arm in ionization (only C IV detected), show offset in velocity (more negative $v_{\rm LSR}$), and do not follow the velocity trends of these known Galactic H I structures.

We examine the association between these MS absorbers and the Stream in detail. The LSR velocity of neutral gas in the Stream has been well characterized through H I 21 cm observations (Brüns et al. 2005; Nidever et al. 2010; Putman et al. 2003b), making it a useful reference for identifying absorbers associated with the Stream. The Stream exhibits a

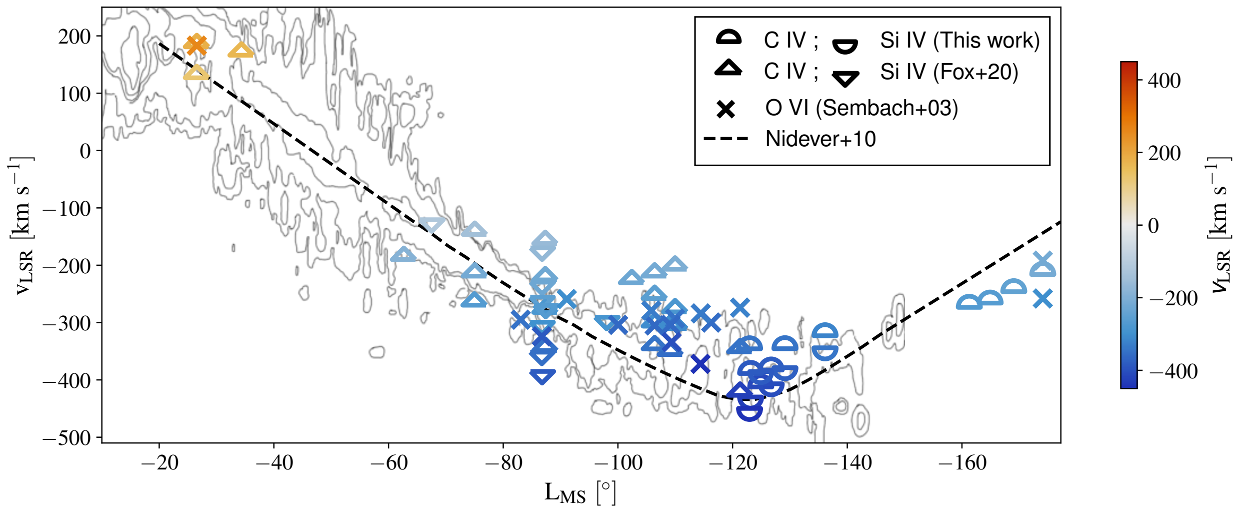

Figure 4.3: Velocity centroid of C IV (half-top circles) and Si IV (half-bottom circles) MS absorbers in the LSR by MS Longitude ($L_{\rm MS}$). The C IV and Si IV from Fox et al. (2020) are also shown in half-top and half-bottom diamonds, respectively, and O VI absorbers from Sembach et al. (2003) are shown as x marks. The velocity gradient suggested by Nidever et al. (2010) is presented with dashed line, and our data follows this trend including velocity inflection at $L_{\rm MS} \sim -120°$. The background H I contours are adopted from Nidever et al. (2010) with permission.

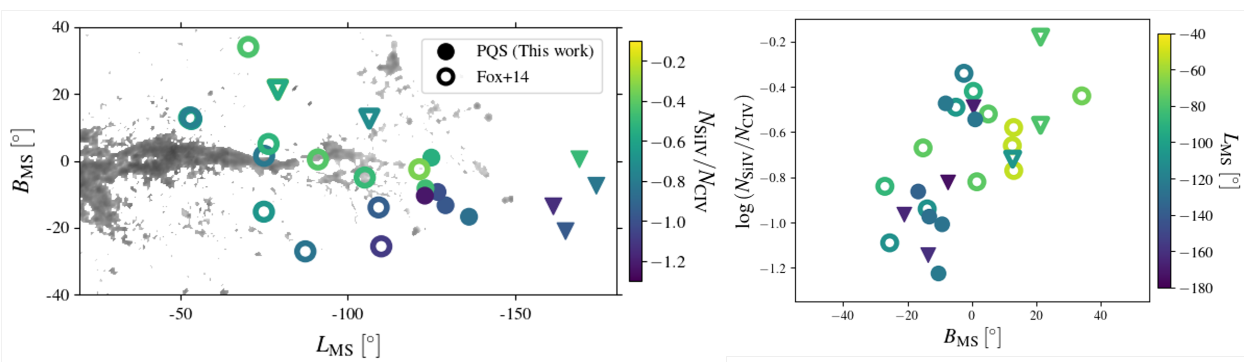

Figure 4.4: The ion column density ratios of Si IV and C IV along the Stream. (Left) QSO sight lines with detected C IV absorption, shown in MS coordinates and color-coded by Si IV/C IV column density ratio. Filled circles represent measurements from this work, and open circles are from Fox et al. (2014). Triangles denote sight lines where only upper limits on Si IV are available. (Right) Si IV/C IV column density ratios along with MS Latitude ($B_{\rm MS}$).

velocity gradient along the MS longitude ($L_{\rm MS}$), with $v_{\rm LSR}$ decreasing nearly linearly and reaching -440 km s^{-1} at the far end of the neutral Stream ($L_{\rm MS} \sim -120°$). This velocity gradient, which provides a critical constraint for formation models of the Stream, has been reproduced in recent simulations (e.g., Besla et al. 2012; Diaz & Bekki 2012; Lucchini et al. 2021 2020). Meanwhile, Nidever et al. (2010) detected H I emission extending to $L_{\rm MS} \sim -150°$ in deep H I 21 cm observations. Their analysis of this extended region revealed a velocity inflection point near $L_{\rm MS} \sim -120°$, where $v_{\rm LSR}$ begins to increase. In Fig. 4.3, we present LSR velocity centroids of our C IV (half-top circles) and Si IV MS absorbers (half-bottom circles) by MS longitude, along with C IV and Si IV absorbers from Fox et al. (2020) (half-top and half-bottom diamonds, respectively) and O VI absorbers from Sembach et al. (2003) (x marks). For O VI absorbers, we only include the absorbers identified as MS-associated in Sembach et al. (2003). The exceptions are absorbers detected in the sight line of H1821+643 ($L_{\rm MS} = -174.1°$, $B_{\rm MS} = -7.4°$), which were newly identified in their work. We also show H I contours and a linear extrapolation of the H I velocity gradient from Nidever et al. (2010) (dashed line). Our C IV MS absorbers closely follow the H I velocity gradient, including the velocity inflection, reinforcing their association with the Stream.

We use ionization structure as an additional test for association with the Stream. In several PQS sight lines, we also detect Si IV (Fig. 4.2), thus we compare the Si IV/C IV column density ratios with those measured in previously studied Stream sight lines. In Fig. 4.4, we present the spatial distribution of Si IV/C IV (left) for both our MS absorbers (filled) and those from Fox et al. (2014) (open). Triangles denote upper limits in cases where Si IV is not detected. The right panel shows the ratio as a function of MS latitude ($B_{\rm MS}$). We find that the Si IV/C IV ratio decreases with decreasing $B_{\rm MS}$, and our new PQS sight lines fall along the same trend as previously studied MS absorbers. While Si IV/C IV is not a straightforward tracer of ionization state, it is noteworthy that the ratio exhibits a dependence on MS latitude. Previous studies have explored ion ratio trends with MS longitude, particularly in low-to-high ion ratios such as C II/C IV and Si II/Si IV. These ratios decrease toward larger negative $L_{\rm MS}$, suggesting that the gas becomes more ionized toward the Stream's trailing end (Fox et al. 2014; Kim et al. 2024). This newly found trend with MS latitude provides additional support that our absorbers are part of the Stream. A detailed exploration of its physical meaning is left to future work with full ionization modeling, but this result may offer a new diagnostic for understanding the origin of the ionized Stream.

Despite kinematic alignment and a consistent ionization trend with the Stream, potential contamination sources must be considered, particularly other Galactic halo HVCs such as the Outer Arm and Complex C (Fig. 4.1). Since several of our sight lines intersect regions associated with these known HVCs, it is necessary to assess whether the MS absorbers are genuinely part of the Stream or potentially associated with other HVCs. In the sight lines above the Galactic plane (J1938+5408, J1858+4850, J1939+7007, and H1821+643), we detect additional absorption components at $v_{\rm LSR} \sim -130$ km s^{-1}, alongside the MS absorbers (green; Fig. 4.2). These components are also seen in lower ionization states, including Al II and Si II, whereas the MS absorbers are only detected in C IV (Table **??**). The LSR velocities and ionization states of these components are consistent with the Outer Arm (Tripp & Song 2012).

Another potential contaminant is the high-velocity ridge of Complex C, a widespread structure with characteristic velocities around $v_{\rm LSR} \sim -180$ km s^{-1} (Tripp et al. 2003; Wakker 2001). Notably, the C IV absorption at $v_{\rm LSR} = -215$ km s^{-1} in the sight line toward H1821+643, identified as an MS absorber here, has previously been reported as a peculiar ionized HVC. Savage et al. (1995) noted that this feature is only detected in C IV, not in any other lower ion species, H I, Mg II, Si II, or S II. Similarly, Tripp et al. (2003) showed the presence of C IV only and suggested that it may trace an extended, highly ionized part of the high-velocity ridge. Lehner & Howk (2010) showed widespread detections of highly ionized HVCs at $v_{\rm LSR} \approx -110$ and -180 km s^{-1} in sight lines near H1821+643, further supporting the existence of a prevalent ionized structure. However, unlike the absorber toward H1821+643, these ionized HVCs generally detected in lower ion species (e.g., Si II, Si III, C II) and tend to have somewhat less negative LSR velocity of -180 to

-150 km s^{-1}.

In contrast, the MS absorbers above the Galactic plane are detected solely in C IV, indicating a higher ionization state. Their LSR velocities span $v_{\text{LSR}} = -215$ to -300 km s^{-1}, far beyond the range associated with the high-velocity ridge. Moreover, they align closely with H I velocity gradient of the Stream (Fig. 4.3). These characteristics support the interpretation that the MS absorbers trace a distinct gaseous structure, likely a highly ionized extension of the Stream, rather than the high-velocity ridge or other Galactic HVCs.

The last potential contamination source is the CGM of M31. Lehner et al. (2020) conducted Project AMIGA, an absorption line survey using QSO sight lines to probe the CGM of M31, and demonstrated that it overlaps with the Stream in both sky position and velocity space. To determine absorber associations, they examined the $L_{\text{MS}} - v_{\text{LSR}}$ plane and adopted the velocity range defined by Nidever et al. (2010) as a reference for identifying Stream-associated absorption. Their findings indicate that absorbers falling within this velocity range are highly likely to be associated with the Stream, and therefore, support the identification of our newly detected C IV absorbers as Stream-associated.

3.2 *Ionization State*

The MS absorbers are primarily detected in C IV, with no detection in low ions such as Si II. It indicates that the gas is highly ionized, consistent with prior studies showing increased ionization toward the trailing end of the Stream based on declining C II/C IV ratios (Kim et al. 2024).

To investigate the ionization mechanism, we consider diagnostic ion ratios such as Si IV/C IV and O VI/C IV, which are commonly used to distinguish between photoionization and collisional ionization scenarios. While our dataset contains only C IV and limited Si IV detections, we incorporate measurements of O VI and Si IV from literature along the Stream, particularly for the tip of the Stream at $L_{\text{MS}} < -105°$, to estimate these ratios where possible (Fox et al. 2014; Sembach et al. 2003).

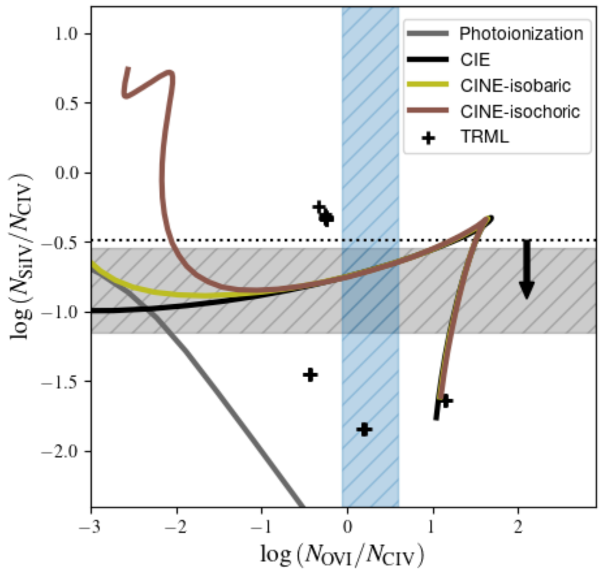

(a) Ion ratios predicted ionization models.

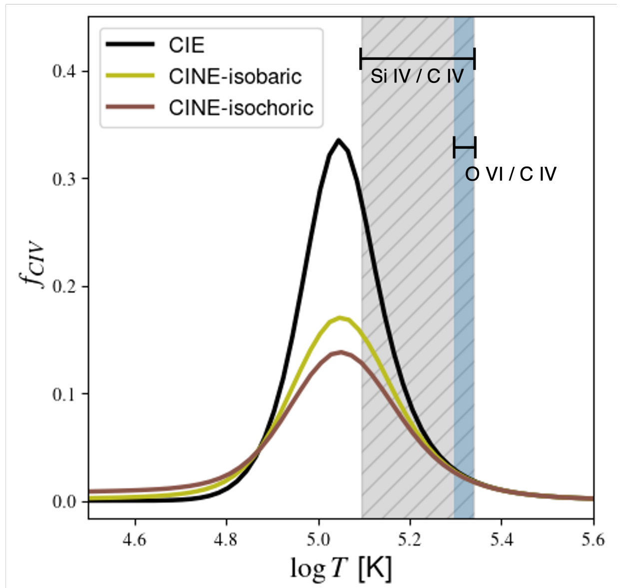

(b) C IV fraction predicted by collisional ionization models.

Figure 4.5: (a) Observed ion column density ratios, $N_{\rm SiIV}/N_{\rm CIV}$ (black-hatched) and $N_{\rm OVI}/N_{\rm CIV}$ (blue-hatched), and comparison with ionization models. We present ion ratio predictions from photoionization (gray), collisional ionization equilibrium (CIE; black), radiative cooling (olive and brown), and turbulent radiative mixing layers models (black pluses). (b) The expected C IV fraction from collisional ionization models (Gnat & Sternberg 2007), collisional ionization equilibrium (black), time-dependent radiative cooling at constant pressure (isobaric; olive) and at constant volume (isochoric; brown). We present sub-solar metallicity ($0.1\ Z_\odot$) for radiative cooling models. The shaded temperature ranges are derived from observed ion column density ratios, $N_{\rm SiIV}/N_{\rm CIV}$ (black) and $N_{\rm OVI}/N_{\rm CIV}$ (blue), respectively.

We performed ionization modeling under both photoionization and collisional ionization scenarios and present the model predictions in Fig. 4.5a. For photoionization, we considered Cloudy models (C17; Ferland et al. 2017) that assume ionization equilibrium and radiation from the Milky Way and the extragalactic background of Haardt & Madau (1996) (Fox et al. 2005). These models fail to reproduce the observed O VI/C IV ratios, which range from $-0.07 \lesssim \log(N_{\rm OVI}/N_{\rm CIV}) \lesssim 0.59$, instead predicting $\log(N_{\rm OVI}/N_{\rm CIV}) < -1$ over a wide range of densities and temperatures (gray; Fig. 4.5a). Although models with extremely low H I column densities of $N_{\rm HI} < 14.5\ {\rm cm}^{-2}$ can yield higher O VI/C IV ratios, they simultaneously predict very low Si IV/C IV values, $\log(N_{\rm SiIV}/N_{\rm CIV}) < -2.5$, which are inconsistent with the observed range of -1.15 to -0.34. This result may suggest that a more extreme radiation source is required to explain the observed ionization state with photoionization, if we assume Si IV, C IV, and O VI are in the same phase of gas. Alternatively, if we instead assume that the kinematically coincident O VI traces a distinct gas phase, then a photoionization model for the observed C IV and Si IV column densities requires low-density gas with hydrogen number density of $n_{\rm H} < 10^{-4}\ {\rm cm^{-3}}$ and a temperature of $T \sim 10^{4.3}$ K. We note that, with a typical C IV column density of $N_{\rm CIV} \sim 10^{13.8}\ {\rm cm^{-2}}$ along the sight lines, this low density implies a very long length scale of the material of > 100 kpc along the sight lines, which is unrealistic, especially given that the Stream in this region is predicted to lie at a distance of order ~ 100 kpc (e.g. Besla et al. 2012).

We also apply the analytic model of turbulent radiative mixing layers (TRMLs) developed by Chen et al. (2023), adopting a fiducial hot gas pressure of $p_{\rm hot}/k_{\rm B} = 10^4\ {\rm K\ cm^{-3}}$. We note that the predicted column density ratios from TRMLs remain nearly constant over a broad range of thermal pressures ($p_{\rm hot}/k_{\rm B} = 10^{3-5}$ K cm^{-3}). We explore a wide parameter space in density contrast between the hot and cold phases ($\chi = 5$–1000) and velocity shear ($v_{\rm shear}$ = 100–400 km s^{-1}). The predicted column density ratios from these models are presented in Fig. 4.5a (black pluses). Some of the TRML models reproduce the observed $N_{\rm OVI}/N_{\rm CIV}$ column density ratios. However, the predicted $N_{\rm SiIV}/N_{\rm CIV}$ ratios are typically lower than the observed values. We note, however, that at the tip of the Stream, where only C IV is detected and Si IV is not, the observed $N_{\rm SiIV}/N_{\rm CIV}$ represents an upper limit. n such cases, the TRML models may plausibly explain the observed ionization conditions.

Finally, we compare the observed ion ratios to predictions from collisional ionization models, including collisional ionization equilibrium (CIE) and non-equilibrium radiative cooling models (Gnat & Sternberg 2007). These models can simultaneously reproduce the observed $N_{\rm SiIV}/N_{\rm CIV}$ and $N_{\rm OVI}/N_{\rm CIV}$ ratios (Fig. 4.5a) with gas at a temperature of $\log T \approx 5.3$ (Fig. 4.5b). If Si IV, C IV, and O VI all arise from a single, collisionally ionized phase, these models offer a self-consistent explanation for the observed ionization state.

3.3 Mass Estimation

The total gas mass in the Stream serves as a critical constraint on the Stream formation and the LMC-SMC and MW dynamics models. It also provides important context for the baryon-to-dark matter (DM) ratio of the Clouds, especially the LMC. The rotation curve of the LMC out to ~ 8.7 kpc suggests a total mass of $\sim 1.7 \times 10^{10}\ M_\odot$ (van der Marel & Kallivayalil 2014), which yields a high baryon fraction of $M_\mathrm{b}/M_\mathrm{DM} \sim 11\%$. If a substantial portion of the Stream's mass was originally stripped from the LMC, this would imply an even higher initial baryon fraction, potentially approaching the cosmic baryon fraction of $\sim 15\%$ (Besla 2015).

The H I mass of the Stream is estimated to be $\sim 2.7 \times 10^8\ M$, assuming a distance of 55 kpc (Brüns et al. 2005). This corresponds to roughly one-third of the total H I gas mass in the Clouds, suggesting that a substantial amount of neutral gas has been stripped to form the Stream. In addition, the Stream likely contains an even greater mass in ionized form, estimated at $\sim 10^9\ M$ (Fox et al. 2014). The ionized gas mass may also be important for examining the properties of the MW halo and Magellanic corona (Lucchini et al. 2024), as some models suggest that a significant fraction of the ionized component may originate in the Magellanic corona and be incorporated into the Stream through interactions with the MW halo (Lucchini et al. 2020), though recent simulations by Zhu et al. (2024) suggest that the CGM of dwarf satellites would be rapidly stripped in MW-like host environments, even for relatively massive dwarfs such as the LMC.

Our discovery of an extended ionized gas adds to the current gas mass estimate. In this section, we estimate the ionized gas mass in this region and discuss its implications for our understanding of the Stream.

An ionization correction using column densities of ions in different ionization states is required to estimate the total ionized gas mass. We derive the total ionized gas mass M_HII, following the approach of Fox et al. (2014):

$$M_{\rm HII} = m_{\rm H} A({\rm H\ II})\,\langle N_{\rm HII}\rangle$$
$$= m_{\rm H} A({\rm H\ II}) \frac{\langle N_{\rm CIV}\rangle}{f_{\rm CIV}[{\rm C/H}]}, \tag{4.1}$$

where $m_{\rm H}$ is the hydrogen mass, A(H II) is the covering area, and $f_{\rm CIV}$ is the C IV fraction relative to the total carbon gas. The angular extent of our newly detected ionized gas, $\approx$ 1800 deg^2, corresponds to a covering area of $A({\rm H\ II}) \approx 1.6 \times 10^{46}$ cm^2 (d/55 kpc)^2. Applying the mean C IV column density of the MS absorbers, $< N_{\rm CIV} >= 5.19 \times 10^{13}$ cm^{-2}, the total ionized gas mass can be expressed as follows.

$$M_{\rm HII} \approx 8.66 \times 10^7\ M_\odot\ \left(\frac{d}{55\ {\rm kpc}}\right)^2 \left(\frac{0.3}{f_{\rm CIV}}\right) \left(\frac{0.1\ Z_\odot}{Z}\right), \tag{4.2}$$

We note that, since only C IV is detected in most sight lines, we cannot observationally constrain $f_{\rm CIV}$. As discussed in Section 3.2, ionization models predict that $f_{\rm CIV}$ varies significantly with ionization conditions and temperature. Our ion ratios indicate a value of $f_{\rm CIV}$ ranging from 0.03 to 0.3 (Fig. 4.5b). The upper limit of 0.3 represents the maximum fraction predicted by both photoionization and collisional ionization models, and therefore provides a conservative lower limit on the total mass. Assuming a metallicity of $Z = 0.1\ Z_\odot$, we estimate corresponding ionized hydrogen column densities of $\log < N_{\rm HII} > = 19.83$ and 18.83 cm^{-2} for $f_{\rm CIV} = 0.03$ and 0.3, respectively. These values are broadly consistent with previous estimates of $\log N_{\rm HII} = 18.93 \pm 0.5$ cm^{-2} in regions where H I is not detected (Fox et al. 2014), and are comparable to predictions from hydrodynamical simulations (Lucchini et al. 2024). Under these assumptions, the total ionized gas mass in the newly discovered extension could range from 6% to 60% of the previously estimated ionized gas mass of the Stream.

4 Discussion

We find that the PQS C IV absorbers discussed in previous sections are most likely associated with the Stream. This discovery reveals that the ionized component of the Stream extends approximately 30° beyond the known H I structure (Nidever et al. 2010). Notably, the absorbers extend to the northern side, crossing the Galactic plane, providing directionality of the Clouds' orbit.

The newly discovered C IV absorbers preserve the Stream's kinematics (Fig. 4.3), indicating that the ionized gas has not yet fully mixed with the MW's hot halo. Assuming a halo temperature of $T \sim 10^6$ K and a radius of ~ 200 kpc, the sound crossing time of the halo is about 1 Gyr. This suggests that the gas may have been stripped from the Clouds relatively recently, within the past $\lesssim 1$ Gyr, before dynamical mixing with the ambient halo could erase its coherent velocity structure.

The detection of C IV implies gas at $T \sim 10^5$ K. Notably, Si IV is not detected at the very trailing end, with $\log{(N_{\rm SiIV}/N_{\rm CIV})} \lesssim -0.8$. For the sight lines where Si IV is detected, Si IV/C IV ratio ranges in $-1.0 \leq \log{(N_{\rm SiIV}/N_{\rm CIV})} \leq -0.54$. This low ratio is inconsistent with predictions from AGN-type photoionization spectra, such as those invoked in the Seyfert flare scenario, which typically produce $\log{(N_{\rm SiIV}/N_{\rm CIV})} \gtrsim -0.2$ (Bland-Hawthorn et al. 2019).

The observed ion ratios are consistent with gas at $\log T \approx 5.3$, supporting a scenario where ionization arises from radiative cooling or turbulent mixing during interaction between the Stream and the clumpy, low-latitude Galactic halo. At this temperature, the radiative cooling time is estimated to be ~ 200 Myr, assuming metallicity of $0.1\ Z_\odot$ (McQuinn & Werk 2018). It suggests that the ionized gas could be produced and remain for hundreds of Myr.

The distance to the Stream remains poorly constrained and almost certainly varies along the length of the Stream. A recent study by Mishra et al. (2025) establishes a firm lower limit of 20 kpc for the distance to the Stream. They further suggest tentative lower limits of 42 kpc and 55 kpc for regions at $L_{\rm MS} \approx -80°$ and $\approx -100°$, respectively. Dynamical models predict that the trailing end of the Stream extends to the farthest distances, reaching $d \gtrsim 120$ kpc (Besla et al. 2012; Diaz & Bekki 2012). This strongly suggests that a considerable mass may be deposited at the most distant regions of the Stream.

5 Summary

We present the discovery of an ionized extension of the Stream that extends to the northern side of the Galactic Plane. This extension was found with PQS HST/COS G160M observations that target QSO sight lines at low Galactic latitudes ($b < 30°$), targetting largely unexplored regions of the MW CGM. This Stream extension reaches approximately 60 degree beyond the previously studied ionized Stream. We detect C IV absorption in the PQS sight lines that fall into an extension in position and LSR velocity of the Stream. This ionized extension is mainly traced by C IV, with Si IV detections in some sight lines. We do not detect any low ions, implying the gas is highly ionized. We suggest these C IV absorbers are associated with the Stream, given that (1) velocity centroids of C IV absorbers align with the velocity gradient of the Stream derived from H I gas, (2) column density ratios Si IV/C IV are consistent with those found in sight lines near the traditional end of the Stream, following a similar trend with Magellanic latitude, and (3) the absorbers present distinct velocity and ionization states from known Galactic HVCs. We explore ionization models, including photoionization, CIE, radiative cooling, and TRMLs, based on the observed ion ratios of Si IV, C IV, and O VI. We find that this ionized extension is in a very low-density photoionized gas ($n_{\rm H} < 10^{-4}$ cm^{-3}) if O VI arises from a distinct gas phase or warm gas phase at $T \approx 10^{5.3}$ K under the assumption that Si IV, C IV, and O VI originate from a single gas phase. We estimate that this ionized extension contributes approximately 6-60% of the previously estimated ionized mass of the Stream, depending on the C IV fraction and distance. Given its position above the Galactic plane, this extension likely traces some of the oldest stripped material in the Stream, and its coherent kinematics suggest it was likely stripped and formed within the past few hundred Myr and has not yet mixed with the hot halo.

6 Appendix: Voigt Profile Fitting

Table 4.2: Best-fit Voigt profile fitting parameters to absorption components.

QSO	$(L_{\rm MS}, B_{\rm MS})$ (deg)	Ion Species	$\log N_{\rm ion}$ ($\rm cm^{-2}$)	b ($\rm km\ s^{-1}$)	$v_{\rm LSR}$ ($\rm km\ s^{-1}$)	Identification
J2206+2757	(-123.0, -10.4)	Al II	12.13 ± 0.52	5.0 ± 20.3	49.2 ± 7.4	
		Si II	13.46 ± 0.12	9.0 ± 6.0	54.1 ± 3.0	
		Si IV	13.39 ± 0.30	20.0 ± 7.8	20.6 ± 6.0	
			13.02 ± 0.11	44.9 ± 15.4	-449.7 ± 10.2	MS
		C IV	13.95 ± 1.5	26.8 ± 27.3	28.7 ± 19.6	
			13.78 ± 0.04	45.0 ± 5.7	-345.8 ± 3.9	MS
J2215+2902	(-123.1, -8.2)	Al II	13.79 ± 0.49	27.9 ± 11.7	-30.7 ± 7.8	
			12.39 ± 3.09	4.1 ± 79.2	-84.3 ± 25.4	
		Si II	14.76 ± 0.15	23.3 ± 4.5	-13.3 ± 3.9	
			14.35 ± 0.12	15.9 ± 4.3	-63.0 ± 4.2	
		Si IV	13.90 ± 0.04	32.7 ± 3.7	-16.9 ± 2.9	
			12.91 ± 0.25	16.9 ± 13.5	-80.8 ± 9.1	
			13.02 ± 0.12	41.1 ± 16.2	-429.8 ± 10.7	MS
		C IV	13.67 ± 0.71	10.8 ± 16.78	20.4 ± 10.3	
			14.44 ± 0.14	30.0 ± 6.4	-13.5 ± 9.1	
			13.50 ± 0.09	30.0 ± 8.9	-388.8 ± 5.8	MS
J2251+3419	(-124.9, 1.0)	Al II	13.43 ± 0.34	34.2 ± 14.7	-14.7 ± 23.0	
			13.54 ± 0.84	17.5 ± 11.3	-59.5 ± 15.2	
		Si II	14.78 ± 0.21	24.9 ± 6.3	-5.8 ± 7.4	
			14.31 ± 0.22	18.1 ± 7.2	-53.7 ± 9.0	
		Si IV	13.36 ± 0.16	37.2 ± 11.2	-21.6 ± 12.3	
			12.99 ± 0.38	24.6 ± 12.2	-73.4 ± 12.2	
		C IV	13.81 ± 0.18	35.0 ± 13.1	-2.0 ± 12.7	
			13.60 ± 0.29	31.7 ± 15.8	-65.1 ± 17.0	
			13.73 ± 0.05	41.1 ± 6.9	-412.7 ± 4.8	MS

Continued on next page

Table 4.2 – continued

QSO	$(L_{\rm MS}, B_{\rm MS})$ (deg)	Ion Species	$\log N_{\rm ion}$ ($\rm cm^{-2}$)	b ($\rm km\,s^{-1}$)	$v_{\rm LSR}$ ($\rm km\,s^{-1}$)	Identification
J2203+3145	(-126.7, -9.3)	Al II	13.93 ± 0.18	38.2 ± 4.4	-32.1 ± 1.7	
		Si II	16.47 ± 1.46	23.8 ± 7.5	-19.6 ± 0.9	
		Si IV	13.58 ± 0.05	22.0 ± 2.7	0.3 ± 2.3	
			13.29 ± 0.09	30.9 ± 8.3	-57.3 ± 6.3	
		C IV	14.29 ± 0.02	30.9 ± 2.1	5.8 ± 1.5	
			13.36 ± 0.11	20.1 ± 7.8	-64.9 ± 5.3	
			13.89 ± 0.03	48.0 ± 4.2	-383.2 ± 2.9	MS
J2141+3151	(-129.1, -13.3)	Al II	13.55 ± 0.05	63.5 ± 7.3	-19.6 ± 5.1	
		Si II	14.84 ± 0.04	63.4 ± 4.1	-22.7 ± 2.8	
		Si IV	13.50 ± 0.04	35.0 ± 4.6	-10.5 ± 3.2	
			13.19 ± 0.09	49.6 ± 13.6	-378.6 ± 9.4	MS
		C IV	14.07 ± 0.05	40.2 ± 5.2	9.7 ± 3.7	
			14.16 ± 0.04	53.6 ± 5.8	-343.7 ± 4.1	MS
J2109+3532	(-136.1, -16.7)	Al II	13.01 ± 0.22	31.9 ± 15.4	73.2 ± 15.6	
			14.44 ± 0.82	40.0 ± 15.2	-31.3 ± 7.1	
		Si II	14.54 ± 0.19	22.8 ± 8.0	70.1 ± 6.7	
			15.43 ± 0.54	38.0 ± 11.3	-29.1 ± 6.2	
		Si IV	12.80 ± 0.43	25.0 ± 28.9	67.6 ± 21.6	
			13.36 ± 0.13	32.1 ± 12.8	1.4 ± 8.8	
			13.04 ± 0.11	35.0 ± 16.7	-346.1 ± 11.4	MS
		C IV	13.75 ± 0.11	28.8 ± 10.9	95.0 ± 7.0	
			13.89 ± 0.08	32.7 ± 9.4	8.9 ± 6.1	
			13.90 ± 0.07	30.0 ± 6.3	-321.8 ± 4.5	MS
J1938+5408	(-161.3, -13.6)	Al II	14.10 ± 0.70	39.0 ± 15.5	-41.7 ± 28.6	
			13.60 ± 0.71	27.2 ± 16.4	-128.2 ± 29.1	OA?
		Si II	15.98 ± 0.66	29.78 ± 6.2	-32.8 ± 2.5	
			14.75 ± 0.15	22.8 ± 3.9	-128.9 ± 2.6	OA?
		Si IV	13.07 ± 0.16	32.8 ± 13.5	-15.1 ± 10.4	
			13.64 ± 0.05	46.0 ± 7.1	-101.8 ± 5.0	OA?
		C IV	13.66 ± 0.04	49.5 ± 6.4	-16.1 ± 4.6	
			13.68 ± 0.04	36.0 ± 3.6	-111.3 ± 2.8	OA?
			13.37 ± 0.03	25.3 ± 3.0	-273.9 ± 1.9	MS
J1858+4850	(-164.9, -21.0)	Al II	13.96 ± 0.12	29.9 ± 2.4	-24.7 ± 1.2	
			13.44 ± 0.03	28.4 ± 1.9	-112.7 ± 1.3	OA?

Continued on next page

Table 4.2 – continued

QSO	$(L_{\rm MS}, B_{\rm MS})$ (deg)	Ion Species	$\log N_{\rm ion}$ ($\rm cm^{-2}$)	b ($\rm km\,s^{-1}$)	$v_{\rm LSR}$ ($\rm km\,s^{-1}$)	Identification
		Si II	15.48 ± 0.61	26.4 ± 6.9	-23.1 ± 2.6	
			14.75 ± 0.11	26.7 ± 4.2	-112.9 ± 2.8	OA?
		Si IV	13.63 ± 0.05	33.0 ± 4.4	-23.3 ± 3.8	
			13.48 ± 0.08	37.0 ± 7.2	-98.5 ± 5.9	OA?
		C IV	14.17 ± 0.05	29.7 ± 4.2	-12.8 ± 3.4	
			14.00 ± 0.07	31.2 ± 5.9	-83.5 ± 4.9	OA?
			13.35 ± 0.09	11.3 ± 6.1	-265.4 ± 3.2	MS
J1939+7007	(-169.0, 0.5)	Al II	14.37 ± 0.51	41.4 ± 11.5	-72.3 ± 16.9	OA?
		Si II	15.81 ± 0.94	28.2 ± 8.6	-49.4 ± 14.1	
			14.50 ± 0.47	29.2 ± 13.8	-119.1 ± 24.6	OA
		Si IV	13.27 ± 0.09	41.7 ± 9.5	-30.6 ± 7.7	
			13.40 ± 0.07	39.4 ± 7.1	-117.7 ± 5.7	OA
		C IV	13.82 ± 0.16	46.6 ± 15.6	-45.4 ± 14.7	
			13.84 ± 0.15	35.6 ± 8.7	-118.3 ± 8.9	OA
			13.02 ± 0.14	10.0 ± 10.3	-247.8 ± 5.1	MS
H1821+643	(-174.1, -7.4)	Al II	16.14 ± 0.22	16.69 ± 0.79	-25.0 ± 1.0	
			14.89 ± 1.53	4.3 ± 2.3	-86.9 ± 1.6	OA?
			13.11 ± 0.04	18.9 ± 1.9	-132.1 ± 1.3	OA
		Si II	13.90 ± 0.13	4.9 ± 0.8	34.9 ± 0.4	
			16.22 ± 0.17	12.6 ± 2.1	-8.6 ± 4.3	
			14.42 ± 0.22	20.0 ± 10.7	-52.6 ± 7.5	
			14.16 ± 0.10	10.0 ± 1.3	-89.2 ± 1.5	OA?
			14.79 ± 0.14	10.8 ± 0.6	-133.3 ± 0.3	OA
		C II	15.40 ± 0.53	8.2 ± 1.3	30.2 ± 1.2	
			18.05 ± 0.25	28.5 ± 1.2	-71.1 ± 1.3	OA?
		S II	15.73 ± 0.03	17.9 ± 0.5	-16.1 ± 0.3	
			14.17 ± 0.07	9.0 ± 2.2	-60.6 ± 1.4	
			14.14 ± 0.05	5.8 ± 1.3	-91.6 ± 0.8	OA?
			14.15 ± 0.08	17.30 ± 3.6	-130.7 ± 2.1	OA
		Si IV	12.85 ± 0.05	14.56 ± 2.1	28.8 ± 1.4	
			13.42 ± 0.03	30.2 ± 2.5	-23.5 ± 1.2	
			13.22 ± 0.04	15.6 ± 1.4	-79.8 ± 0.9	OA?
			13.33 ± 0.02	24.1 ± 1.5	-126.9 ± 1.0	OA
		C IV	13.16 ± 0.07	14.6 ± 3.1	28.5 ± 2.0	
			14.07 ± 0.02	12.7 ± 0.7	-8.6 ± 0.4	

Continued on next page

Table 4.2 – continued

QSO	$(L_{\rm MS}, B_{\rm MS})$ (deg)	Ion Species	$\log N_{\rm ion}$ ($\rm cm^{-2}$)	b ($\rm km\,s^{-1}$)	$v_{\rm LSR}$ ($\rm km\,s^{-1}$)	Identification
			13.91 ± 0.04	29.6 ± 2.7	-70.0 ± 1.8	OA?
			13.82 ± 0.04	26.8 ± 2.2	-128.1 ± 2.1	OA
			13.31 ± 0.04	6.6 ± 0.9	-216.2 ± 0.6	MS
		N V	12.99 ± 0.09	5.5 ± 2.2	19.1 ± 1.4	
			14.20 ± 0.03	10.4 ± 0.6	-8.0 ± 0.4	
			13.13 ± 0.10	25.0 ± 6.9	-104.8 ± 4.8	OA

Voigt profile fit parameters for all detected ion species in the PQS sight lines. The Magellanic Stream coordinates, $(L_{\rm MS}, B_{\rm MS})$, of each PQS sight line are also provided. For each absorption component, we present the ion column density ($N_{\rm ion}$), Doppler b-parameter, and velocity centroid in the LSR. Absorption components with velocity offsets distinguishable from the ISM are labeled by their likely association: MS = Magellanic Stream; OA= Outer Arm; C = Complex C).

Chapter 5

Conclusions and Future Work

1 Conclusion

The Milky Way is the only galaxy where the gas flowing between the disk and its surrounding atmosphere can be resolved spatially, kinematically, and chemically on the scales most directly relevant to star formation. In this dissertation, I have used HST/COS UV absorption spectroscopy combined with Voigt profile fitting and photoionization modeling, supplemented by independent constraints from H I 21 cm emission and pulsar dispersion measures, to characterize the current weather of the Milky Way's inner atmosphere and to forecast its impact on Galactic chemical evolution.

In Chapter 2, I introduced and extended a method that uses pulsar dispersion measures from globular clusters paired with UV-bright halo stars at matched distances to provide a precise ionization correction to the total hydrogen column. Applying this approach to the diffuse ionized gas at the disk-halo interface, I found that the gas spans a wide range of metallicities and does not separate cleanly into a metal-poor inflow and metal-rich outflow population. The detection of a super-solar infalling cloud is consistent with a Galactic fountain origin (motivating Chapter 3), while at least one low-metallicity outflowing cloud poses a challenge for standard fountain and feedback models, indicating that the disk-halo interface hosts clouds of mixed origin actively cycling through the lower halo.

The super-solar infalling cloud detected in Chapter 2 was kinematically associated with the intermediate-velocity cloud Complex K, motivating a deeper investigation of this candidate fountain flow. In Chapter 3, I spatially resolved the metallicity, ionization, and kinematics of Complex K across 28 sight lines, mapping a Galactic fountain flow in unprecedented detail. The majority of the gas is metal-rich ($\langle Z \rangle \sim 2.4\ Z_{\odot}$), with the most metal-rich components showing the slowest infall and progressively lower metallicities at higher infall velocities, capturing fountain-driven mixing with the metal-poor corona in action. These results forecast that fountain accretion returns gas to the disk well above the metallicities assumed in chemical evolution models.

In Chapter 4 (Choi et al. 2025), I searched the underexplored low-latitude sky using HST/COS G160M spectra from the Plane Quasar Survey and reported the discovery of an ionized extension of the Magellanic Stream on the northern side of the Galactic plane, reaching approximately 60° beyond its previously known ionized extent. The newly detected gas is highly ionized, traced primarily by C IV absorption with consistent ionization trends with previously studied Stream sight lines, suggesting collisional ionization at $T \sim 10^{5.3}$ K. The extension increases the previous ionized gas mass estimate of the Stream and, by its position above the Galactic plane, places new constraints on the orbital direction of the Magellanic Clouds and the Stream's recent dynamical history.

Together, these results contribute resolved measurements of the metallicity, ionization, and kinematics of gas flows in the Milky Way's inner halo. The picture that emerges is one in which the disk-halo interface is populated by clouds spanning a continuum of metallicities and ionization states, with fountain recycling, coronal condensation, and satellite stripping operating simultaneously. Future progress will require distance constraints to a larger sample of halo gas structures, which remain the dominant uncertainty in nearly all derived properties, and a closer connection between observations and theories of multiphase halo gas. I outline two future directions along these lines in the next section.

2 Future Work

How much gas the Milky Way's halo contains, how fast it accretes, and what chemical imprint it leaves on the disk all depend on quantities that remain poorly constrained. The total mass of the HVC population, including the Magellanic Stream, is uncertain by more than an order of magnitude because mass scales as d^2 and distances to most halo gas structures are known only as rough brackets or lower limits (e.g., Mishra et al. 2025; Wakker 2001). Inflow rates and accretion timescales inherit the same uncertainties, leaving even basic questions, such as whether the current gas supply can sustain star formation over Gyr timescales, without firm answers. Direct 3D mapping of halo gas would allow these quantities to be pinned down, and would enable comparison of observed cloud kinematics and spatial distributions with fountain and accretion simulations (e.g., Fraternali et al. 2015), connecting the halo gas cycle to the disk's star formation history.

Achieving this mapping requires both a larger sample of distant background sources and the spectroscopic sensitivity to detect weak halo gas absorption at high spectral resolution. Halo stars at $d \gtrsim 20$ kpc can be identified through surveys such as Gaia Gaia Collaboration et al. (2023), DESI Koposov et al. (2024), and H3 (Conroy et al. 2019), but at these distances the targets are too faint for current facilities to obtain the high-resolution, high-S/N spectra needed to detect weak absorption features. In the optical, even 8–10 m telescopes require prohibitively long exposures to detect Ca II and Na I at sufficient spectral resolution toward stars beyond ~ 20 kpc. In the UV, HST/STIS, and even COS face similar sensitivity limits, restricting metal-line absorption studies to the brightest and nearest halo stars.

The next decade of facilities will address these limitations from complementary directions. Rubin Observatory's LSST, now underway, will deliver deep photometry over the full southern sky (Ivezić et al. 2019), potentially identifying blue horizontal branch stars and RR Lyrae variables well beyond $d \sim 50$ kpc and expanding the pool of halo stars available for distance-bracketing experiments. On the ground, the Giant Magellan Telescope and the Extremely Large Telescope, with first light expected in the 2030s, will provide the spectroscopic sensitivity needed to reach these faint targets at distances currently inaccessible with 8–10 m facilities, including stars behind the Magellanic Stream. In the UV, the Habitable Worlds Observatory with ≥ 6 m mirror will extend UV spectroscopic sensitivity well beyond HST at resolutions up to ($R \geq 30,000$), reaching fainter halo stars at larger distances. With these capabilities in view, the following subsections describe two future directions that address specific open questions in the Milky Way's baryon cycle.

2.1 Distance to the Magellanic Stream

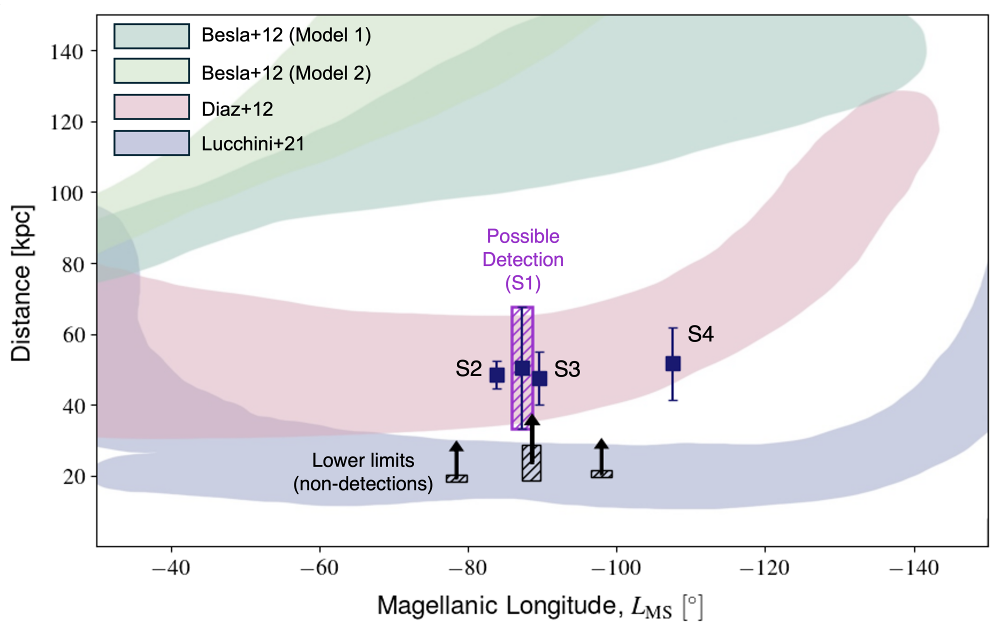

Figure 5.1: Distance predictions for the Magellanic Stream from various dynamical models as a function of Magellanic longitude. The colored regions show predicted distance ranges from different theoretical models: Besla et al. 2012 (Model 1; dark green), Besla et al. 2012 (Model 2; light green), Diaz & Bekki 2012 (pink), and Lucchini et al. 2021 (purple). Squares mark the positions of our sample with distance errors. The currently known lower limits ($\sim$ 20 kpc) are shown with black hatched boxes (Mishra et al. 2025). The large spread in model predictions demonstrates the critical need for empirical distance measurements.

The Magellanic Stream's distance remains the single most important unknown governing its physical interpretation. Because mass scales as d^2, he current total mass estimate of $\sim 2 \times 10^9\ M_\odot$ (Fox et al. 2014), which assumes a fiducial distance of 55 kpc, could be incorrect by more than an order of magnitude: dynamical models predict distances ranging from 20 to over 200 kpc depending on the region along the Stream (Fig. 5.1). This uncertainty propagates directly into the estimated mass inflow rate of $\sim 4-7\ M_\odot\ \mathrm{yr}^{-1}$ (D'Onghia & Fox 2016), leaving the Stream's contribution to future Galactic star formation effectively unconstrained.

The distance question is also tightly coupled to the orbital history of the Magellanic Clouds, one of the most debated problems in Local Group dynamics. The Clouds were traditionally thought to be on a second passage around the Milky Way (Diaz & Bekki 2012; Yoshizawa & Noguchi 2003), but precise proper motion measurements from HST suggest they may instead be on their first infall (Besla et al. 2007; Kallivayalil et al. 2013), a scenario that successfully reproduces several observed features of the Stream (Besla et al. 2012). Resolving this question requires precise constraints on the Stream's three-dimensional position and velocity, which in turn depend on distance measurements along multiple regions of the Stream.

Recent efforts have begun to narrow the distance range. Stellar counterparts to the Stream have been identified, with populations spanning $d \sim 55$–120 kpc (Chandra et al. 2023; Zaritsky et al. 2025 2020), supporting at least partial tidal origin. For the gaseous Stream, Mishra et al. (2025) provided the first strict lower limit of $d \gtrsim 20$ kpc based on non-detections of absorption toward background BHB stars. However, the gas and stars need not trace the same distances: unlike tidally stripped stars, the gaseous component is subject to hydrodynamic forces such as ram pressure and turbulent drag from the Milky Way's hot halo, which can displace gas from any associated stellar debris in both position and velocity.

Building on this progress, we have been awarded Gemini/GMOS time to directly bracket the gaseous Stream's distance across multiple regions, using halo stars with well-determined distances at ~ 50 kpc from DESI and H3 as background sources (planned observation in June 2026). Low-resolution GMOS spectroscopy will efficiently survey these stars using the detection or non-detection of Ca II absorption: detections provide upper distance limits, while non-detections yield lower limits. As LSST identifies BHBs and RR Lyrae at larger distances in the coming years, and GMT/ELT provides the sensitivity to observe them, this approach will extend distance brackets well beyond the current availability, yielding the spatially distributed distance constraints needed to determine the Stream's 3D geometry, total mass, and role in the Milky Way's gas accretion budget.

2.2 Constraining the survival and origin of cool clouds in the Milky Way's nuclear outflow

Galactic winds driven by stellar feedback and black hole activity transport energy, mass, and metals from galaxies into their CGM and beyond (Veilleux et al. 2005). These winds are ubiquitously observed in star-forming and active galaxies across cosmic time and are often found to be multiphase, comprising hot ($T \gtrsim 10^6$ K), warm (10^{4-5} K), and cool ($< 10^4$ K) gas phases (Veilleux et al. 2020; Zhang 2018). The prevalent detection of cool and warm gas in such winds poses a fundamental question: how does this gas exist in the hostile environment of a fast, hot outflow, and what are its origins? Cool clouds may be entrained from the galactic disk and swept into the hot wind, though hydrodynamic instabilities are expected to destroy such clouds on short timescales unless stabilized by radiative cooling at the cloud-wind interface (Gronke & Oh 2018 2020) or by magnetic fields (McCourt et al. 2015). Alternatively, cool gas may condense out of the hot wind itself through radiative cooling as the outflow expands (Thompson et al. 2016) (Fig. 5.2 (a)). Regardless of the formation mechanism, a key unresolved question is how far from the disk cool gas survives within hot winds, whether it is destroyed and mixed into the hot halo, or persists to large distances where it may eventually fall back onto the disk and fuel future star formation (Veilleux et al. 2020).

The Milky Way provides a unique opportunity to study this problem up close. The Fermi bubbles, giant γ-ray emitting bipolar lobes extending up to $b \sim 50°$ (Su et al. 2010), and the even larger eROSITA bubbles, detected in X-rays and reaching $b \sim 75°$ (Predehl et al. 2020), trace the Galaxy's own nuclear outflow. The origin of these bubbles remains debated, with potential mechanisms including SMBH outbursts (e.g., jets or accretion-driven winds) and past nuclear starbursts. While both can plausibly power the bubbles, their different energy injection timescales and coupling mechanisms leave observable imprints on the outflow kinematics, ionization, and thermal state. It is also unclear whether

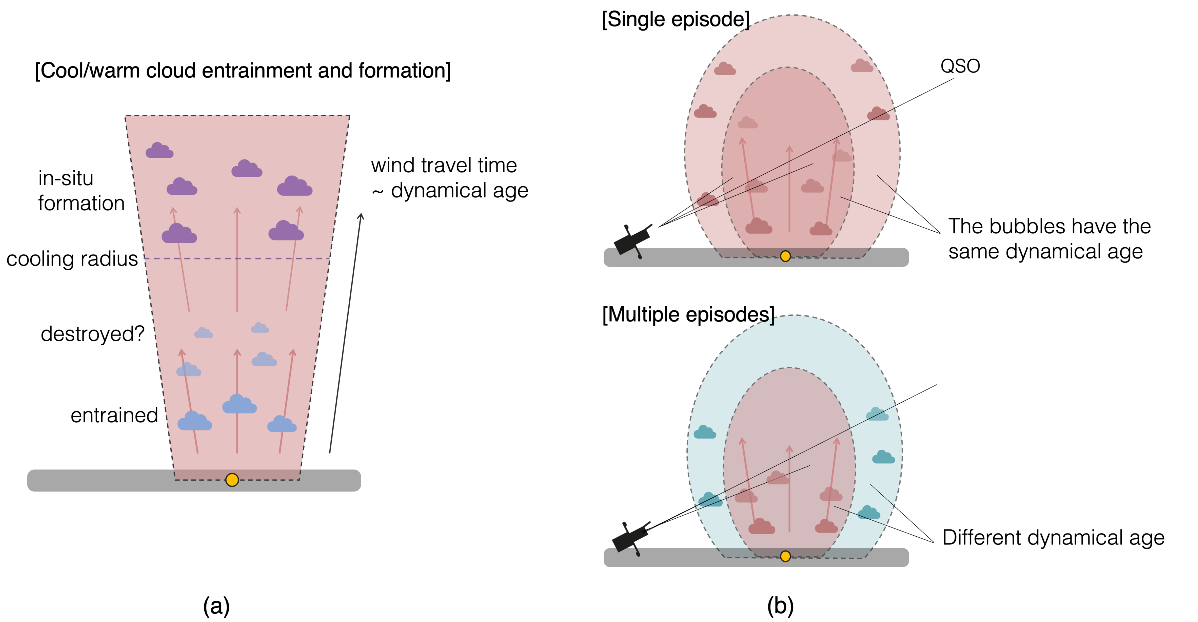

Figure 5.2: Schematic overview of cool gas in the Galactic bubbles. (a) Clouds are either entrained from the disk or condense in situ via radiative cooling in the hot wind; travel times constrain survival and formation scenarios. (b) A single outburst (top) produces clouds of uniform age and kinematics, while two episodes (bottom) yield two kinematically distinct populations.

the Fermi and eROSITA bubbles were produced by the same event or by different episodes (Fig. 5.2b). Single-episode models propose that both structures arise from one outburst, with the Fermi and eROSITA boundaries corresponding to different hydrodynamic features such as a contact discontinuity and forward shock (Yang et al. 2022). Multi-episode models instead suggest two different energy injections, each driving its own shock to produce the two bubbles (Scheffler et al. 2025; Zhang et al. 2025). These scenarios span a range of driving mechanisms and timescales, from AGN jets active for about 0.1 Myr to sustained starbursts over $\sim$ 100 Myr, but all predict different outflow ages and thermodynamic structures, which directly affect the production and survival of cool-warm gas within the outflow. Therefore, the three-dimensional distribution and kinematics of this gas offers an independent constraint to distinguish between the competing models.

Deep H I 21 cm observations have revealed numerous cold HVCs near the Galactic center whose kinematics are consistent with a biconical outflow expanding at $v_{\rm exp} \approx 330$ km s^{-1} (Di Teodoro et al. 2018; Lockman & McClure-Griffiths 2016). UV absorption toward QSOs has extended these detections to higher latitudes, with HVC detection rates of $> 80\%$ inside the Fermi bubbles compared to $\sim$ 20–30% outside (Ashley et al. 2020; Bordoloi et al. 2017; Fox et al. 2015), confirming the physical association of cool clouds with the nuclear outflow.

Two specific questions can be addressed by 3D mapping of the outflow clouds:

Q1. Do the Fermi Bubble HVCs form a single kinematic population? The anomalous velocities and wide metallicity range observed in previous work (Ashley et al. 2022 2020) cannot be fully interpreted without distance information. If all HVCs originate from a single outflow episode, their velocities should vary smoothly with distance, consistent with existing biconical wind models (Bordoloi et al. 2017). If instead the Fermi and eROSITA bubbles trace separate outflow episodes (Scheffler et al. 2025; Zhang et al. 2025), distinct groupings in velocity-distance space would be expected, implying different travel times and outflow ages.

Q2. How far do cool-warm HVCs extend, and what are their survival timescales? The detection rate of absorption as a function of background star distance directly measures how far cool gas persists in the outflow. Combined with measured velocities, distances yield cloud travel times that can be compared with theoretical survival timescales (Gronke & Oh 2018). Clouds detected at distances implying travel times exceeding the cloud-crushing time would favor stabilization or in-situ condensation, while a drop in detection rate beyond a certain distance would constrain where clouds are destroyed and mixed into the hot halo.

Bibliography

Afruni, A., Pezzulli, G., & Fraternali, F. 2022, MNRAS, 509, 4849, doi: 10.1093/mnras/stab3237

Anderson, S. B. 1993, PhD thesis, California Institute of Technology

Andrews, B. H., Weinberg, D. H., Schönrich, R., & Johnson, J. A. 2017, ApJ, 835, 224, doi: 10.3847/1538-4357/835/2/224

Anglés-Alcázar, D., Faucher-Giguère, C.-A., Kereš, D., et al. 2017, MNRAS, 470, 4698, doi: 10.1093/mnras/stx1517

Armillotta, L., Fraternali, F., & Marinacci, F. 2016, MNRAS, 462, 4157, doi: 10.1093/mnras/stw1930

Ashley, T., Fox, A. J., Cashman, F. H., et al. 2022, Nature Astronomy, 6, 968, doi: 10.1038/s41550-022-01720-0

Ashley, T., Fox, A. J., Jenkins, E. B., et al. 2020, ApJ, 898, 128, doi: 10.3847/1538-4357/ab9ff8

Bailer-Jones, C. A. L., Rybizki, J., Fouesneau, M., Demleitner, M., & Andrae, R. 2021, VizieR Online Data Catalog, I/352

Barger, K. A., Madsen, G. J., Fox, A. J., et al. 2017, ApJ, 851, 110, doi: 10.3847/1538-4357/aa992a

Baumgardt, H., & Vasiliev, E. 2021, MNRAS, 505, 5957, doi: 10.1093/mnras/stab1474

Begelman, M. C., & Fabian, A. C. 1990, MNRAS, 244, 26P

Behroozi, P. S., Conroy, C., & Wechsler, R. H. 2010, ApJ, 717, 379, doi: 10.1088/0004-637X/717/1/379

Bergeron, J. 1986, A&A, 155, L8

Besla, G. 2015, arXiv e-prints, arXiv:1511.03346, doi: 10.48550/arXiv.1511.03346

Besla, G., Kallivayalil, N., Hernquist, L., et al. 2007, ApJ, 668, 949, doi: 10.1086/521385

—. 2010, ApJ, 721, L97, doi: 10.1088/2041-8205/721/2/L97

—. 2012, MNRAS, 421, 2109, doi: 10.1111/j.1365-2966.2012.20466.x

Bigiel, F., Leroy, A., Walter, F., et al. 2008, AJ, 136, 2846, doi: 10.1088/0004-6256/136/6/2846

Bingham, E., Chen, J. P., Jankowiak, M., et al. 2019, J. Mach. Learn. Res., 20, 28:1. http://jmlr.org/papers/v20/18-403.html

Birnboim, Y., & Dekel, A. 2003, MNRAS, 345, 349, doi: 10.1046/j.1365-8711.2003.06955.x

Bish, H. V., Werk, J. K., Prochaska, J. X., et al. 2019, ApJ, 882, 76, doi: 10.3847/1538-4357/ab3414

Bland-Hawthorn, J., & Maloney, P. R. 1999, ApJ, 510, L33, doi: 10.1086/311797

Bland-Hawthorn, J., Sutherland, R., Agertz, O., & Moore, B. 2007, ApJ, 670, L109, doi: 10.1086/524657

Bland-Hawthorn, J., Maloney, P. R., Sutherland, R., et al. 2019, ApJ, 886, 45, doi: 10.3847/1538-4357/ab44c8

Bordoloi, R., Prochaska, J. X., Tumlinson, J., et al. 2018, ApJ, 864, 132, doi: 10.3847/1538-4357/aad8ac

Bordoloi, R., Fox, A. J., Lockman, F. J., et al. 2017, ApJ, 834, 191, doi: 10.3847/1538-4357/834/2/191

Borkowski, K. J., Balbus, S. A., & Fristrom, C. C. 1990, ApJ, 355, 501, doi: 10.1086/168784

Bowen, D. V., Jenkins, E. B., Tripp, T. M., et al. 2008, ApJS, 176, 59, doi: 10.1086/524773

Bregman, J. N. 1980, ApJ, 236, 577, doi: 10.1086/157776

Bromm, V., & Yoshida, N. 2011, ARA&A, 49, 373, doi: 10.1146/annurev-astro-081710-102608

Brüns, C., Kerp, J., Staveley-Smith, L., et al. 2005, A&A, 432, 45, doi: 10.1051/0004-6361:20040321

Bryan, G. L., & Norman, M. L. 1998, ApJ, 495, 80, doi: 10.1086/305262

Bustard, C., & Gronke, M. 2022, ApJ, 933, 120, doi: 10.3847/1538-4357/ac752b

Byström, A., Koposov, S. E., Lilleengen, S., et al. 2025, MNRAS, 542, 560, doi: 10.1093/mnras/staf1219

Cashman, F. H., Fox, A. J., Wakker, B. P., et al. 2023, ApJ, 944, 65, doi: 10.3847/1538-4357/acaaa5

Chandra, V., Naidu, R. P., Conroy, C., et al. 2023, ApJ, 956, 110, doi: 10.3847/1538-4357/acf7bf

Chayer, P., Dixon, W. V., Fullerton, A. W., Ooghe-Tabanou, B., & Reid, I. N. 2015, MNRAS, 452, 2292, doi: 10.1093/mnras/stv1435

Chen, H.-W., Lanzetta, K. M., & Webb, J. K. 2001, ApJ, 556, 158, doi: 10.1086/321537

Chen, Z., Fielding, D. B., & Bryan, G. L. 2023, ApJ, 950, 91, doi: 10.3847/1538-4357/acc73f

Chiappini, C., Matteucci, F., & Gratton, R. 1997, ApJ, 477, 765, doi: 10.1086/303726

Chiappini, C., Matteucci, F., & Romano, D. 2001, ApJ, 554, 1044, doi: 10.1086/321427

Chisholm, J., Tremonti, C. A., Leitherer, C., & Chen, Y. 2017, MNRAS, 469, 4831, doi: 10.1093/mnras/stx1164

Choi, B.-E., Werk, J. K., Tchernyshyov, K., et al. 2024, ApJ, 976, 222, doi: 10.3847/1538-4357/ad84f8

—. 2025, ApJ, 995, L24, doi: 10.3847/2041-8213/ae2308

Chomiuk, L., & Povich, M. S. 2011, AJ, 142, 197, doi: 10.1088/0004-6256/142/6/197

Collins, J. A., Shull, J. M., & Giroux, M. L. 2004, ApJ, 605, 216, doi: 10.1086/382269

—. 2007, ApJ, 657, 271, doi: 10.1086/510770

Conroy, C., Bonaca, A., Cargile, P., et al. 2019, ApJ, 883, 107, doi: 10.3847/1538-4357/ab38b8

Cordes, J. M., & Lazio, T. J. W. 2002, arXiv e-prints, astro, doi: 10.48550/arXiv.astro-ph/0207156

Culpan, R., Pelisoli, I., & Geier, S. 2021, A&A, 654, A107, doi: 10.1051/0004-6361/202040074

Dai, S., Johnston, S., Kerr, M., et al. 2020, ApJ, 888, L18, doi: 10.3847/2041-8213/ab621a

D'Amico, N., Possenti, A., Fici, L., et al. 2002, ApJ, 570, L89, doi: 10.1086/341030

D'Amico, N., Possenti, A., Manchester, R. N., et al. 2001, ApJ, 561, L89, doi: 10.1086/324562

Danforth, C. W., Keeney, B. A., Stocke, J. T., Shull, J. M., & Yao, Y. 2010, ApJ, 720, 976, doi: 10.1088/0004-637X/720/1/976

Danforth, C. W., Keeney, B. A., Tilton, E. M., et al. 2016, ApJ, 817, 111, doi: 10.3847/0004-637X/817/2/111

Davé, R., Finlator, K., & Oppenheimer, B. D. 2012, MNRAS, 421, 98, doi: 10.1111/j.1365-2966.2011.20148.x

de Avillez, M. A., Asgekar, A., Breitschwerdt, D., & Spitoni, E. 2012, MNRAS, 423, L107, doi: 10.1111/j.1745-3933.2012.01267.x

de Boer, K. S., & Savage, B. D. 1984, A&A, 136, L7

De Cia, A., Jenkins, E. B., Fox, A. J., et al. 2021, Nature, 597, 206, doi: 10.1038/s41586-021-03780-0

Dekel, A., & Birnboim, Y. 2006, MNRAS, 368, 2, doi: 10.1111/j.1365-2966.2006.10145.x

Dekel, A., Birnboim, Y., Engel, G., et al. 2009, Nature, 457, 451, doi: 10.1038/nature07648

DESI Collaboration, Abdul Karim, M., Adame, A. G., et al. 2026, AJ, 171, 285, doi: 10.3847/1538-3881/ae4c43

Di Teodoro, E. M., McClure-Griffiths, N. M., Lockman, F. J., & Armillotta, L. 2020, Nature, 584, 364, doi: 10.1038/s41586-020-2595-z

Di Teodoro, E. M., McClure-Griffiths, N. M., Lockman, F. J., et al. 2018, ApJ, 855, 33, doi: 10.3847/1538-4357/aaad6a

Diaz, J. D., & Bekki, K. 2012, ApJ, 750, 36, doi: 10.1088/0004-637X/750/1/36

Dixon, W. V., Chayer, P., Reid, I. N., & Miller Bertolami, M. M. 2019, AJ, 157, 147, doi: 10.3847/1538-3881/ab0b40

D'Onghia, E., & Fox, A. J. 2016, ARA&A, 54, 363, doi: 10.1146/annurev-astro-081915-023251

Dopita, M. A., & Sutherland, R. S. 1996, ApJS, 102, 161, doi: 10.1086/192255

Edgar, R. J., & Chevalier, R. A. 1986, ApJ, 310, L27, doi: 10.1086/184775

Fang, T., Mckee, C. F., Canizares, C. R., & Wolfire, M. 2006, ApJ, 644, 174, doi: 10.1086/500310

Faucher-Giguère, C.-A., & Oh, S. P. 2023, ARA&A, 61, 131, doi: 10.1146/annurev-astro-052920-125203

Ferland, G. J., Chatzikos, M., Guzmán, F., et al. 2017, Rev. Mexicana Astron. Astrofis., 53, 385, doi: 10.48550/arXiv.1705.10877

Field, G. B. 1965, ApJ, 142, 531, doi: 10.1086/148317

Fielding, D. B., Ostriker, E. C., Bryan, G. L., & Jermyn, A. S. 2020, ApJ, 894, L24, doi: 10.3847/2041-8213/ab8d2c

Fox, A. J., Cashman, F. H., Kriss, G. A., et al. 2023, ApJ, 946, L48, doi: 10.3847/2041-8213/acc640

Fox, A. J., Frazer, E. M., Bland-Hawthorn, J., et al. 2020, ApJ, 897, 23, doi: 10.3847/1538-4357/ab92a3

Fox, A. J., Richter, P., Ashley, T., et al. 2019, ApJ, 884, 53, doi: 10.3847/1538-4357/ab40ad

Fox, A. J., Richter, P., Wakker, B. P., et al. 2013, ApJ, 772, 110, doi: 10.1088/0004-637X/772/2/110

Fox, A. J., Savage, B. D., Sembach, K. R., et al. 2003, ApJ, 582, 793, doi: 10.1086/344692

Fox, A. J., Savage, B. D., Wakker, B. P., et al. 2004, ApJ, 602, 738, doi: 10.1086/381024

Fox, A. J., Wakker, B. P., Savage, B. D., et al. 2005, ApJ, 630, 332, doi: 10.1086/431915

Fox, A. J., Wakker, B. P., Barger, K. A., et al. 2014, ApJ, 787, 147, doi: 10.1088/0004-637X/787/2/147

Fox, A. J., Bordoloi, R., Savage, B. D., et al. 2015, ApJ, 799, L7, doi: 10.1088/2041-8205/799/1/L7

Fraternali, F. 2017, in Astrophysics and Space Science Library, Vol. 430, Gas Accretion onto Galaxies, ed. A. Fox & R. Davé, 323, doi: 10.1007/978-3-319-52512-9_14

Fraternali, F., & Binney, J. J. 2006, MNRAS, 366, 449, doi: 10.1111/j.1365-2966.2005.09816.x

—. 2008, MNRAS, 386, 935, doi: 10.1111/j.1365-2966.2008.13071.x

Fraternali, F., Marasco, A., Armillotta, L., & Marinacci, F. 2015, MNRAS, 447, L70, doi: 10.1093/mnrasl/slu182

Fraternali, F., van Moorsel, G., Sancisi, R., & Oosterloo, T. 2002, AJ, 123, 3124, doi: 10.1086/340358

Freire, P. C. C., Wolszczan, A., van den Berg, M., & Hessels, J. W. T. 2008, ApJ, 679, 1433, doi: 10.1086/587832

Fumagalli, M., O'Meara, J. M., & Prochaska, J. X. 2016, MNRAS, 455, 4100, doi: 10.1093/mnras/stv2616

Fumagalli, M., Prochaska, J. X., Kasen, D., et al. 2011, MNRAS, 418, 1796, doi: 10.1111/j.1365-2966.2011.19599.x

Gaensler, B. M., Madsen, G. J., Chatterjee, S., & Mao, S. A. 2008, PASA, 25, 184, doi: 10.1071/AS08004

Gaia Collaboration, Vallenari, A., Brown, A. G. A., et al. 2023, A&A, 674, A1, doi: 10.1051/0004-6361/202243940

Garza, S. L., Werk, J. K., Berg, T. A. M., et al. 2025, ApJ, 978, L12, doi: 10.3847/2041-8213/ad9c69

Ghavamian, P., Aloisi, A., Lennon, D., et al. 2009, Preliminary Characterization of the Post-Launch Line Spread Function of COS, COS Instrument Science Report 2009-01(v1), 23 pages

Gnat, O., & Sternberg, A. 2007, ApJS, 168, 213, doi: 10.1086/509786

Gronke, M., & Oh, S. P. 2018, MNRAS, 480, L111, doi: 10.1093/mnrasl/sly131

—. 2020, MNRAS, 492, 1970, doi: 10.1093/mnras/stz3332

Haardt, F., & Madau, P. 1996, ApJ, 461, 20, doi: 10.1086/177035

—. 2012, ApJ, 746, 125, doi: 10.1088/0004-637X/746/2/125

Hafen, Z., Faucher-Giguère, C.-A., Anglés-Alcázar, D., et al. 2019, MNRAS, 488, 1248, doi: 10.1093/mnras/stz1773

—. 2020, MNRAS, 494, 3581, doi: 10.1093/mnras/staa902

Hafen, Z., Stern, J., Bullock, J., et al. 2022, MNRAS, 514, 5056, doi: 10.1093/mnras/stac1603

Haffner, L. M., Reynolds, R. J., & Tufte, S. L. 2001, ApJ, 556, L33, doi: 10.1086/322867

Haffner, L. M., Reynolds, R. J., Tufte, S. L., et al. 2003, ApJS, 149, 405, doi: 10.1086/378850

Hammer, F., Yang, Y. B., Flores, H., Puech, M., & Fouquet, S. 2015, ApJ, 813, 110, doi: 10.1088/0004-637X/813/2/110

Heckman, T., Borthakur, S., Wild, V., Schiminovich, D., & Bordoloi, R. 2017, ApJ, 846, 151, doi: 10.3847/1538-4357/aa80dc

Heckman, T. M., & Thompson, T. A. 2017, arXiv e-prints, arXiv:1701.09062, doi: 10.48550/arXiv.1701.09062

Heitsch, F., & Putman, M. E. 2009, ApJ, 698, 1485, doi: 10.1088/0004-637X/698/2/1485

Hessels, J. W. T., Ransom, S. M., Stairs, I. H., Kaspi, V. M., & Freire, P. C. C. 2007, ApJ, 670, 363, doi: 10.1086/521780

HI4PI Collaboration, Ben Bekhti, N., Flöer, L., et al. 2016, A&A, 594, A116, doi: 10.1051/0004-6361/201629178

Hoffman, M., Sountsov, P., Dillon, J. V., et al. 2019, NeuTra-lizing Bad Geometry in Hamiltonian Monte Carlo Using Neural Transport. https://arxiv.org/abs/1903.03704

Hoffman, M. D., & Gelman, A. 2011, The No-U-Turn Sampler: Adaptively Setting Path Lengths in Hamiltonian Monte Carlo. https://arxiv.org/abs/1111.4246

Howk, J. C., Rueff, K. M., Lehner, N., et al. 2018, ApJ, 856, 166, doi: 10.3847/1538-4357/aab1fa

Howk, J. C., Sembach, K. R., & Savage, B. D. 2006, ApJ, 637, 333, doi: 10.1086/497352

Ivezić, Ž., Kahn, S. M., Tyson, J. A., et al. 2019, ApJ, 873, 111, doi: 10.3847/1538-4357/ab042c

Jenkins, E. B. 2013, ApJ, 764, 25, doi: 10.1088/0004-637X/764/1/25

Johnson, J. W. 2025, arXiv e-prints, arXiv:2510.05223, doi: 10.48550/arXiv.2510.05223

Johnson, J. W., Weinberg, D. H., Blanc, G. A., et al. 2025, ApJ, 988, 8, doi: 10.3847/1538-4357/addbe5

Joung, M. R., Putman, M. E., Bryan, G. L., Fernández, X., & Peek, J. E. G. 2012, ApJ, 759, 137, doi: 10.1088/0004-637X/759/2/137

Kalberla, P. M. W., Burton, W. B., Hartmann, D., et al. 2005, A&A, 440, 775, doi: 10.1051/0004-6361:20041864

Kallivayalil, N., van der Marel, R. P., Alcock, C., et al. 2006, ApJ, 638, 772, doi: 10.1086/498972

Kallivayalil, N., van der Marel, R. P., Besla, G., Anderson, J., & Alcock, C. 2013, ApJ, 764, 161, doi: 10.1088/0004-637X/764/2/161

Kereš, D., Katz, N., Fardal, M., Davé, R., & Weinberg, D. H. 2009, MNRAS, 395, 160, doi: 10.1111/j.1365-2966.2009.14541.x

Kereš, D., Katz, N., Weinberg, D. H., & Davé, R. 2005, MNRAS, 363, 2, doi: 10.1111/j.1365-2966.2005.09451.x

Kim, C.-G., & Ostriker, E. C. 2018, ApJ, 853, 173, doi: 10.3847/1538-4357/aaa5ff

Kim, D. A., Zheng, Y., & Putman, M. E. 2024, ApJ, 966, 134, doi: 10.3847/1538-4357/ad2def

Klein, R. I., McKee, C. F., & Colella, P. 1994, ApJ, 420, 213, doi: 10.1086/173554

Koposov, S. E., Allende Prieto, C., Cooper, A. P., et al. 2024, MNRAS, 533, 1012, doi: 10.1093/mnras/stae1842

Krishnarao, D., Fox, A. J., D'Onghia, E., et al. 2022, Nature, 609, 915, doi: 10.1038/s41586-022-05090-5

Larson, R. B. 1972, Nature, 236, 21, doi: 10.1038/236021a0

Lehner, N., & Howk, J. C. 2010, ApJ, 709, L138, doi: 10.1088/2041-8205/709/2/L138

—. 2011, Science, 334, 955, doi: 10.1126/science.1209069

Lehner, N., Howk, J. C., Marasco, A., & Fraternali, F. 2022, MNRAS, 513, 3228, doi: 10.1093/mnras/stac987

Lehner, N., Howk, J. C., Thom, C., et al. 2012, MNRAS, 424, 2896, doi: 10.1111/j.1365-2966.2012.21428.x

Lehner, N., Wotta, C. B., Howk, J. C., et al. 2018, ApJ, 866, 33, doi: 10.3847/1538-4357/aadd03

Lehner, N., Howk, J. C., Tripp, T. M., et al. 2013, ApJ, 770, 138, doi: 10.1088/0004-637X/770/2/138

Lehner, N., Berek, S. C., Howk, J. C., et al. 2020, ApJ, 900, 9, doi: 10.3847/1538-4357/aba49c

Leroy, A. K., Walter, F., Brinks, E., et al. 2008, AJ, 136, 2782, doi: 10.1088/0004-6256/136/6/2782

Licquia, T. C., & Newman, J. A. 2015, ApJ, 806, 96, doi: 10.1088/0004-637X/806/1/96

Lilly, S. J., Carollo, C. M., Pipino, A., Renzini, A., & Peng, Y. 2013, ApJ, 772, 119, doi: 10.1088/0004-637X/772/2/119

Lin, D. N. C., & Lynden-Bell, D. 1977, MNRAS, 181, 59, doi: 10.1093/mnras/181.2.59

Lockman, F. J., & McClure-Griffiths, N. M. 2016, ApJ, 826, 215, doi: 10.3847/0004-637X/826/2/215

Lucchini, S. 2024, Ap&SS, 369, 114, doi: 10.1007/s10509-024-04377-5

Lucchini, S., D'Onghia, E., & Fox, A. J. 2021, ApJ, 921, L36, doi: 10.3847/2041-8213/ac3338

—. 2024, ApJ, 967, 16, doi: 10.3847/1538-4357/ad3c3b

Lucchini, S., D'Onghia, E., Fox, A. J., et al. 2020, Nature, 585, 203, doi: 10.1038/s41586-020-2663-4

Lucchini, S., Han, J. J., Hernquist, L., Conroy, C., & Fox, A. J. 2025, ApJ, 990, 118, doi: 10.3847/1538-4357/adf3b3

Maiolino, R., & Mannucci, F. 2019, A&A Rev., 27, 3, doi: 10.1007/s00159-018-0112-2

Maller, A. H., & Bullock, J. S. 2004, MNRAS, 355, 694, doi: 10.1111/j.1365-2966.2004.08349.x

Manchester, R. N., Hobbs, G. B., Teoh, A., & Hobbs, M. 2005, AJ, 129, 1993, doi: 10.1086/428488

Mannucci, F., Cresci, G., Maiolino, R., Marconi, A., & Gnerucci, A. 2010, MNRAS, 408, 2115, doi: 10.1111/j.1365-2966.2010.17291.x

Marasco, A., Fraternali, F., & Binney, J. J. 2012, MNRAS, 419, 1107, doi: 10.1111/j.1365-2966.2011.19771.x

Marasco, A., Fraternali, F., Lehner, N., & Howk, J. C. 2022, MNRAS, 515, 4176, doi: 10.1093/mnras/stac1172

Marinacci, F., Binney, J., Fraternali, F., et al. 2010, MNRAS, 404, 1464, doi: 10.1111/j.1365-2966.2010.16352.x

Marinacci, F., Fraternali, F., Nipoti, C., et al. 2011, MNRAS, 415, 1534, doi: 10.1111/j.1365-2966.2011.18810.x

Martin, C. L., Shapley, A. E., Coil, A. L., et al. 2012, ApJ, 760, 127, doi: 10.1088/0004-637X/760/2/127

Mastropietro, C., Moore, B., Mayer, L., Wadsley, J., & Stadel, J. 2005, MNRAS, 363, 509, doi: 10.1111/j.1365-2966.2005.09435.x

Mathewson, D. S., Cleary, M. N., & Murray, J. D. 1974, ApJ, 190, 291, doi: 10.1086/152875

Matteucci, F. 2021, A&A Rev., 29, 5, doi: 10.1007/s00159-021-00133-8

McCourt, M., Oh, S. P., O'Leary, R., & Madigan, A.-M. 2018, MNRAS, 473, 5407, doi: 10.1093/mnras/stx2687

McCourt, M., O'Leary, R. M., Madigan, A.-M., & Quataert, E. 2015, MNRAS, 449, 2, doi: 10.1093/mnras/stv355

McGaugh, S. S., Schombert, J. M., de Blok, W. J. G., & Zagursky, M. J. 2010, ApJ, 708, L14, doi: 10.1088/2041-8205/708/1/L14

McQuinn, M., & Werk, J. K. 2018, ApJ, 852, 33, doi: 10.3847/1538-4357/aa9d3f

Melioli, C., Brighenti, F., D'Ercole, A., & de Gouveia Dal Pino, E. M. 2008, MNRAS, 388, 573, doi: 10.1111/j.1365-2966.2008.13446.x

Melso, N., Bryan, G. L., & Li, M. 2019, ApJ, 872, 47, doi: 10.3847/1538-4357/aafaf5

Miller, M. J., & Bregman, J. N. 2015, ApJ, 800, 14, doi: 10.1088/0004-637X/800/1/14

Mishra, S., Fox, A. J., Smoker, J. V., Lucchini, S., & D'Onghia, E. 2025, arXiv e-prints, arXiv:2503.14368. https://arxiv.org/abs/2503.14368

Mishra, S., Fox, A. J., Krishnarao, D., et al. 2024, ApJ, 976, L28, doi: 10.3847/2041-8213/ad8b9d

Mo, H. J., & Miralda-Escude, J. 1996, ApJ, 469, 589, doi: 10.1086/177808

Moehler, S., Landsman, W. B., Lanz, T., & Miller Bertolami, M. M. 2019, A&A, 627, A34, doi: 10.1051/0004-6361/201935694

Mooney, C. J., Rolleston, W. R. J., Keenan, F. P., et al. 2002, MNRAS, 337, 851, doi: 10.1046/j.1365-8711.2002.05912.x

Mou, G., Sun, D., Fang, T., et al. 2023, Nature Communications, 14, 781, doi: 10.1038/s41467-023-36478-0

Münch, G., & Zirin, H. 1961, ApJ, 133, 11, doi: 10.1086/146999

Muratov, A. L., Kereš, D., Faucher-Giguère, C.-A., et al. 2015, MNRAS, 454, 2691, doi: 10.1093/mnras/stv2126

Murphy, E. M., Lockman, F. J., & Savage, B. D. 1995, ApJ, 447, 642, doi: 10.1086/175906

Nidever, D. L., Majewski, S. R., & Butler Burton, W. 2008, ApJ, 679, 432, doi: 10.1086/587042

Nidever, D. L., Majewski, S. R., Butler Burton, W., & Nigra, L. 2010, ApJ, 723, 1618, doi: 10.1088/0004-637X/723/2/1618

O'Malley, E. M., Gilligan, C., & Chaboyer, B. 2017, ApJ, 838, 162, doi: 10.3847/1538-4357/aa6574

Oosterloo, T., Fraternali, F., & Sancisi, R. 2007, AJ, 134, 1019, doi: 10.1086/520332

Oppenheimer, B. D., & Schaye, J. 2013, MNRAS, 434, 1043, doi: 10.1093/mnras/stt1043

Pagel, B. E. J. 1997, Nucleosynthesis and Chemical Evolution of Galaxies

Pagel, B. E. J., & Patchett, B. E. 1975, MNRAS, 172, 13, doi: 10.1093/mnras/172.1.13

Pallanca, C., Ransom, S. M., Ferraro, F. R., et al. 2014, ApJ, 795, 29, doi: 10.1088/0004-637X/795/1/29

Pan, Z., Qian, L., Ma, X., et al. 2021, ApJ, 915, L28, doi: 10.3847/2041-8213/ac0bbd

Peek, J. E. G., Heiles, C., Douglas, K. A., et al. 2011, ApJS, 194, 20, doi: 10.1088/0067-0049/194/2/20

Peeples, M., Tumlinson, J., Fox, A., et al. 2017a, The Hubble Spectroscopic Legacy Archive, Instrument Science Report COS 2017-4, 8 pages

—. 2017b, The Hubble Spectroscopic Legacy Archive, Instrument Science Report COS 2017-4, 8 pages

Peeples, M. S., Werk, J. K., Tumlinson, J., et al. 2014, ApJ, 786, 54, doi: 10.1088/0004-637X/786/1/54

Péroux, C., & Howk, J. C. 2020, ARA&A, 58, 363, doi: 10.1146/annurev-astro-021820-120014

Phan, D., Pradhan, N., & Jankowiak, M. 2019, arXiv preprint arXiv:1912.11554

Pointon, S. K., Kacprzak, G. G., Nielsen, N. M., et al. 2019, ApJ, 883, 78, doi: 10.3847/1538-4357/ab3b0e

Ponti, G., Zheng, X., Locatelli, N., et al. 2023, A&A, 674, A195, doi: 10.1051/0004-6361/202243992

Predehl, P., Sunyaev, R. A., Becker, W., et al. 2020, Nature, 588, 227, doi: 10.1038/s41586-020-2979-0

Prochaska, J. X., Tejos, N., Crighton, N., et al. 2016, Linetools/Linetools: Second Major Release, v0.2, Zenodo, Zenodo, doi: 10.5281/zenodo.168270

Prochaska, J. X., Werk, J. K., Worseck, G., et al. 2017a, ApJ, 837, 169, doi: 10.3847/1538-4357/aa6007

Prochaska, J. X., Tejos, N., Crighton, N., et al. 2017b, Linetools/Linetools: Third Minor Release, v0.3, Zenodo, Zenodo, doi: 10.5281/zenodo.1036773

Prochaska, J. X., Tejos, N., cwotta, et al. 2017, pyigm/pyigm: Initial release for publications, v1.0, Zenodo, doi: 10.5281/zenodo.1045480

Putman, M. E., Bland-Hawthorn, J., Veilleux, S., et al. 2003a, ApJ, 597, 948, doi: 10.1086/378555

Putman, M. E., Peek, J. E. G., & Joung, M. R. 2012, ARA&A, 50, 491, doi: 10.1146/annurev-astro-081811-125612

Putman, M. E., Staveley-Smith, L., Freeman, K. C., Gibson, B. K., & Barnes, D. G. 2003b, ApJ, 586, 170, doi: 10.1086/344477

Putman, M. E., de Heij, V., Staveley-Smith, L., et al. 2002, AJ, 123, 873, doi: 10.1086/338088

Rees, M. J., & Ostriker, J. P. 1977, MNRAS, 179, 541, doi: 10.1093/mnras/179.4.541

Reynolds, R. J. 1990, ApJ, 349, L17, doi: 10.1086/185640

Richter, P. 2017, in Astrophysics and Space Science Library, Vol. 430, Gas Accretion onto Galaxies, ed. A. Fox & R. Davé, 15, doi: 10.1007/978-3-319-52512-9_2

Richter, P., Fox, A. J., Wakker, B. P., et al. 2013, ApJ, 772, 111, doi: 10.1088/0004-637X/772/2/111

Ritchey, A. M., Jenkins, E. B., Shull, J. M., et al. 2023, ApJ, 952, 57, doi: 10.3847/1538-4357/acda25

Rubin, K. H. R., Prochaska, J. X., Koo, D. C., & Phillips, A. C. 2012, ApJ, 747, L26, doi: 10.1088/2041-8205/747/2/L26

Saintonge, A., Lutz, D., Genzel, R., et al. 2013, ApJ, 778, 2, doi: 10.1088/0004-637X/778/1/2

Salem, M., Bryan, G. L., & Corlies, L. 2016, MNRAS, 456, 582, doi: 10.1093/mnras/stv2641

Sánchez Almeida, J., Elmegreen, B. G., Muñoz-Tuñón, C., & Elmegreen, D. M. 2014, A&A Rev., 22, 71, doi: 10.1007/s00159-014-0071-1

Savage, B. D., & Sembach, K. R. 1991, ApJ, 379, 245, doi: 10.1086/170498

Savage, B. D., Sembach, K. R., & Lu, L. 1995, ApJ, 449, 145, doi: 10.1086/176040

Savage, B. D., & Wakker, B. P. 2009, ApJ, 702, 1472, doi: 10.1088/0004-637X/702/2/1472

Scheffler, T., Schulreich, M. M., Schurer, D. P. P. R., & Breitschwerdt, D. 2025, A&A, 695, A34, doi: 10.1051/0004-6361/202451965

Schmidt, M. 1963, ApJ, 137, 758, doi: 10.1086/147553

Schönrich, R., Binney, J., & Dehnen, W. 2010, MNRAS, 403, 1829, doi: 10.1111/j.1365-2966.2010.16253.x

Sembach, K. R., Howk, J. C., Savage, B. D., & Shull, J. M. 2001, AJ, 121, 992, doi: 10.1086/318777

Sembach, K. R., Wakker, B. P., Savage, B. D., et al. 2003, ApJS, 146, 165, doi: 10.1086/346231

Shapiro, P. R., & Field, G. B. 1976, ApJ, 205, 762, doi: 10.1086/154332

Shull, J. M., Jones, J. R., Danforth, C. W., & Collins, J. A. 2009, ApJ, 699, 754, doi: 10.1088/0004-637X/699/1/754

Slavin, J. D., Shull, J. M., & Begelman, M. C. 1993, ApJ, 407, 83, doi: 10.1086/172494

Spitoni, E., Silva Aguirre, V., Matteucci, F., Calura, F., & Grisoni, V. 2019, A&A, 623, A60, doi: 10.1051/0004-6361/201834188

Spitzer, Jr., L. 1956, ApJ, 124, 20, doi: 10.1086/146200

Steidel, C. C., Erb, D. K., Shapley, A. E., et al. 2010, ApJ, 717, 289, doi: 10.1088/0004-637X/717/1/289

Stern, J., Faucher-Giguère, C.-A., Hennawi, J. F., et al. 2018, ApJ, 865, 91, doi: 10.3847/1538-4357/aac884

Stern, J., Fielding, D., Faucher-Giguère, C.-A., & Quataert, E. 2020, MNRAS, 492, 6042, doi: 10.1093/mnras/staa198

Stern, J., Hennawi, J. F., Prochaska, J. X., & Werk, J. K. 2016, ApJ, 830, 87, doi: 10.3847/0004-637X/830/2/87

Su, M., Slatyer, T. R., & Finkbeiner, D. P. 2010, ApJ, 724, 1044, doi: 10.1088/0004-637X/724/2/1044

Sutherland, R. S., & Dopita, M. A. 1993, ApJS, 88, 253, doi: 10.1086/191823

Tan, B., & Oh, S. P. 2021, MNRAS, 508, L37, doi: 10.1093/mnrasl/slab100

Tan, B., Oh, S. P., & Gronke, M. 2023, MNRAS, 520, 2571, doi: 10.1093/mnras/stad236

Thom, C., Peek, J. E. G., Putman, M. E., et al. 2008, ApJ, 684, 364, doi: 10.1086/589960

Thompson, T. A., Quataert, E., Zhang, D., & Weinberg, D. H. 2016, MNRAS, 455, 1830, doi: 10.1093/mnras/stv2428

Tosi, M. 1988, A&A, 197, 47

Tremonti, C. A., Heckman, T. M., Kauffmann, G., et al. 2004, ApJ, 613, 898, doi: 10.1086/423264

Tripp, T. M., & Song, L. 2012, ApJ, 746, 173, doi: 10.1088/0004-637X/746/2/173

Tripp, T. M., Wakker, B. P., Jenkins, E. B., et al. 2003, AJ, 125, 3122, doi: 10.1086/374995

Tumlinson, J., Peeples, M. S., & Werk, J. K. 2017, ARA&A, 55, 389, doi: 10.1146/annurev-astro-091916-055240

Tumlinson, J., Thom, C., Werk, J. K., et al. 2011, Science, 334, 948, doi: 10.1126/science.1209840

—. 2013, ApJ, 777, 59, doi: 10.1088/0004-637X/777/1/59

van de Voort, F., Schaye, J., Booth, C. M., Haas, M. R., & Dalla Vecchia, C. 2011, MNRAS, 414, 2458, doi: 10.1111/j.1365-2966.2011.18565.x

van der Marel, R. P., & Kallivayalil, N. 2014, ApJ, 781, 121, doi: 10.1088/0004-637X/781/2/121

van Woerden, H., Wakker, B. P., Schwarz, U. J., & de Boer, K. S. 2004, 312, doi: 10.1007/1-4020-2579-3

Veilleux, S., Cecil, G., & Bland-Hawthorn, J. 2005, ARA&A, 43, 769, doi: 10.1146/annurev.astro.43.072103.150610

Veilleux, S., Maiolino, R., Bolatto, A. D., & Aalto, S. 2020, A&A Rev., 28, 2, doi: 10.1007/s00159-019-0121-9

Verschuur, G. L., Schmelz, J. T., Escorza, A., & Jorissen, A. 2024, ApJ, 963, 87, doi: 10.3847/1538-4357/ad1bd4

Wakker, B. P. 2001, ApJS, 136, 463, doi: 10.1086/321783

Wakker, B. P., & Mathis, J. S. 2000, ApJ, 544, L107, doi: 10.1086/317316

Wakker, B. P., & van Woerden, H. 1997, ARA&A, 35, 217, doi: 10.1146/annurev.astro.35.1.217

Wakker, B. P., Howk, J. C., Savage, B. D., et al. 1999, Nature, 402, 388, doi: 10.1038/46498

Wang, J., Hammer, F., Yang, Y., et al. 2019, MNRAS, 486, 5907, doi: 10.1093/mnras/stz1274

Wang, L., Peng, B., Stappers, B. W., et al. 2020, ApJ, 892, 43, doi: 10.3847/1538-4357/ab76cc

Wang, Q. D., & McCray, R. 1993, ApJ, 409, L37, doi: 10.1086/186854

Weiner, B. J., & Williams, T. B. 1996, AJ, 111, 1156, doi: 10.1086/117860

Werk, J., Tchernyshyov, K., Bish, H., et al. 2024, ApJS, 273, 21, doi: 10.3847/1538-4365/ad58df

Werk, J. K., Prochaska, J. X., Thom, C., et al. 2013, ApJS, 204, 17, doi: 10.1088/0067-0049/204/2/17

Werk, J. K., Prochaska, J. X., Tumlinson, J., et al. 2014, ApJ, 792, 8, doi: 10.1088/0004-637X/792/1/8

Werk, J. K., Rubin, K. H. R., Bish, H. V., et al. 2019, ApJ, 887, 89, doi: 10.3847/1538-4357/ab54cf

Westmeier, T. 2018, MNRAS, 474, 289, doi: 10.1093/mnras/stx2757

White, S. D. M., & Frenk, C. S. 1991, ApJ, 379, 52, doi: 10.1086/170483

White, S. D. M., & Rees, M. J. 1978, MNRAS, 183, 341, doi: 10.1093/mnras/183.3.341

Wilde, M. C., Tchernyshyov, K., Werk, J. K., et al. 2023, ApJ, 948, 114, doi: 10.3847/1538-4357/acc85b

Winkel, B., Kerp, J., Flöer, L., et al. 2016, A&A, 585, A41, doi: 10.1051/0004-6361/201527007

Wotta, C. B., Lehner, N., Howk, J. C., et al. 2019, ApJ, 872, 81, doi: 10.3847/1538-4357/aafb74

Xue, X.-X., Rix, H.-W., Yanny, B., et al. 2011, ApJ, 738, 79, doi: 10.1088/0004-637X/738/1/79

Yang, H.-Y. K., Ruszkowski, M., & Zweibel, E. G. 2022, Nature Astronomy, 6, 584, doi: 10.1038/s41550-022-01618-x

Yoshizawa, A. M., & Noguchi, M. 2003, MNRAS, 339, 1135, doi: 10.1046/j.1365-8711.2003.06263.x

Zaritsky, D., Chandra, V., Conroy, C., et al. 2025, The Open Journal of Astrophysics, 8, 16, doi: 10.33232/001c.129885

Zaritsky, D., Conroy, C., Naidu, R. P., et al. 2020, ApJ, 905, L3, doi: 10.3847/2041-8213/abcb83

Zech, W. F., Lehner, N., Howk, J. C., Dixon, W. V. D., & Brown, T. M. 2008, ApJ, 679, 460, doi: 10.1086/587135

Zhang, D. 2018, Galaxies, 6, 114, doi: 10.3390/galaxies6040114

Zhang, L., Ridolfi, A., Blumer, H., et al. 2022, ApJ, 934, L21, doi: 10.3847/2041-8213/ac81c3

Zhang, R., Guo, F., Xie, S., et al. 2025, arXiv e-prints, arXiv:2507.13665, doi: 10.48550/arXiv.2507.13665

Zheng, Y., Peek, J. E. G., Putman, M. E., & Werk, J. K. 2019, ApJ, 871, 35, doi: 10.3847/1538-4357/aaf6eb

Zhu, J., Tonnesen, S., Bryan, G. L., & Putman, M. E. 2024, ApJ, 974, 142, doi: 10.3847/1538-4357/ad6c3f